I.O.S.

GREAT METEOR EAST
(DISTAL MADERIA ABYSSAL PLAIN):
GEOLOGICAL STUDIES OF ITS SUITABILITY FOR DISPOSAL OF HEAT-EMITTING RADIOACTIVE WASTES

BY
R.C. SEARLE, P.J. SCHULTHEISS
P.P.E. WEAVER, M. NOEL, R.B. KIDD,
C.L. JACOBS AND Q.J. HUGGETT

REPORT NO. 193
1985

OCEAN DISPOSAL OF HIGH LEVEL RADIOACTIVE WASTE
A RESEARCH REPORT PREPARED FOR THE DEPARTMENT
OF THE ENVIRONMENT

NATURAL ENVIRONMENT RESEARCH COUNCIL
INSTITUTE OF
OCEANOGRAPHIC
SCIENCES

INSTITUTE OF OCEANOGRAPHIC SCIENCES

Wormley, Godalming,
Surrey, GU8 5UB.
(0428 - 79 - 4141)
(Director: Dr. A.S. Laughton FRS)

Bidston Observatory,
Birkenhead,
Merseyside, L43 7RA.
(051 - 653 - 8633)
(Assistant Director: Dr. D.E. Cartwright FRS)

Crossway,
Taunton,
Somerset, TA1 2DW.
(0823 - 86211)
(Assistant Director: M.J. Tucker)

When citing this document in a bibliography the reference should be given as follows:-

SEARLE, R.C., SCHULTHEISS, P.J., WEAVER, P.P.E., NOEL, M., KIDD, R.B., JACOBS, C.L. & HUGGETT, Q.J. 1985
Great Meteor East (distal Madeira Abyssal Plain): geological studies of its suitability for disposal of heat-emitting radioactive wastes.
Institute of Oceanographic Sciences, Report, No. 193, 162pp.

INSTITUTE OF OCEANOGRAPHIC SCIENCES

WORMLEY

Great Meteor East (distal Madeira Abyssal Plain): geological studies of its suitability for disposal of heat-emitting radioactive wastes

by

R.C. Searle, P.J. Schultheiss,
P.P.E. Weaver, M. Noel, R.B. Kidd,
C.L. Jacobs and Q.J. Huggett

I.O.S. Report No. 193

1985

DEPARTMENT OF THE ENVIRONMENT
RADIOACTIVE WASTE MANAGEMENT
RESEARCH PROGRAMME 1979/84

DoE Report No.:	RW/84/32
Contract Title:	Selection and evaluation of sites for the disposal of radioactive waste.
DoE Reference:	DGR 481/179
Report Title:	Great Meteor East (Distal Madeira Abyssal Plain): geological studies of its suitability for disposal of heat-emitting radioactive wastes
Authors:	SEARLE, R.C., SCHULTHEISS, P.J., WEAVER, P.P.E., NOEL, M.J., KIDD, R.B., JACOBS, C.L. and HUGGETT, Q.J.
Date of submission to DoE:	7 September 1984

ABSTRACT
This report summarises geological and geophysical studies carried out by the Institute of Oceanographic Sciences up to December 1983 in an area of the Madeira Abyssal Plain in order to assess its suitability for the disposal of heat-emitting radioactive waste. The results of work carried out in the same area by the Rijks Geologische Dienst of the Netherlands are also reviewed in the report. Other oceanographic studies in the area in the fields of geochemistry, biology and oceanography are briefly touched upon.

Keywords:
91 - Disposal (general)
92 - Geologic disposal
93 - Disposal on deep ocean bed
94 - Disposal under deep ocean bed
110 - Geology
225 - Ocean sites
299 - DoE sponsored research

This work has been commissioned by the Department of the Environment as part of its radioactive waste management research programme. The results will be used in the formulation of Government policy but, at this stage, they do not necessarily represent Government policy.

CONTENTS Page

CONTENTS continued

1. INTRODUCTION

1.1 Scope of the report

This report summarises the geological and geophysical studies carried out by the Institute of Oceanographic Sciences (IOS) between 1980 and 1983, inclusive, to assess the suitability of an area of the Madeira Abyssal Plain for heat-emitting radioactive waste disposal. All the work carried out during that period is reported here; however, some of the data and samples collected during that period have not yet been fully analysed, so the results of these analyses will be reported in a future work, together with the results of data collected since 1983. On the other hand, we occasionally include here brief mention of some results obtained since the end of 1983, where relevant.

A large body of work has also been carried out in the area by the Netherlands Rijks Geologische Dienst (RGD: State Geological Service), and we review that work and combine their results with ours wherever possible. Much of the IOS and Dutch work was co-ordinated through the 'Seabed Working Group' (SWG) of the Organisation for Economic Co-operation and Development's Nuclear Energy Agency.

In addition to the purely geological and geophysical work, there have been studies by IOS and others in the fields of geochemistry, biology, and physical oceanography. Although we have made no attempt to review that work rigorously, we have included brief discussions of some of the salient features that seem most relevant to the geological and geophysical studies.

The area of the Madeira Abyssal Plain chosen for detailed study lies some 200 to 500 km NE of Great Meteor Seamount (Fig. 2.1); it has consequently been designated "Great Meteor East" (GME). (Another study area that received some early attention from the SWG lies west of the seamount, and was called "Great Meteor West"). The boundaries of GME have not been precisely delineated. Most of the IOS work reported here was carried out between 30.5°N and 32.5°N, 23°W and 26°W, while the RGD has extended its coverage from 30°N to 33°N between the same longitudes. Some work has also been carried out outside the boundaries of GME, and is reported where appropriate.

1.2 History of the investigations

In March 1980, the SWG's Site Assessment Task Group decided to include distal abyssal plains in the group of 'generic' or 'type' areas to be considered for potential disposal sites (Anderson, 1980, pp. 112-113). The early work in the area was mainly contributed by the Dutch RGD, with an 11-day survey using

HNLMS Tydeman in November-December 1980, and a 15-day study with MS Tyro in April 1982 (Kuijpers, 1982; Duin & Kuijpers, 1983). These cruises laid down a regular grid of tracks and obtained some 7000-8000 km of watergun seismic reflection and 3.5 kHz profiler records (Fig. 1.1), as well as 45 evenly-spaced piston cores (Fig. 1.2). During this time IOS work was divided between GME and the King's Trough Flank area north of the Azores (Kidd et al., 1983a).

IOS work at GME has concentrated on developing and applying techniques that were largely not available to the Dutch, so as to complement rather than duplicate their effort. Thus our only cruise to undertake extensive underway geophysical observations was Farnella Cruise 3/81, which was dedicated to GLORIA long-range sidescan sonar observations, and concommitantly recorded airgun seismic reflection profiles (Fig. 1.1). During the course of the other three cruises (Discovery 118, 126 and 134) we carried out a seismicity survey and developed and used techniques for high-resolution seismic profiling (2.0 and 3.5 kHz sources), piston coring, near-bottom camera and seismic profiling surveys, dredging of sediment surfaces, heat flow and geotechnical measurements, and seismology using seabed artificial sound sources (Table 1.1; Fig. 1.2). The major objectives of the work were: (1) to produce a detailed stratigraphy of the sediments in order to assess the sedimentation history and especially any evidence for erosion; (2) to understand the processes of sediment transport within and around the area in order to predict its future evolution; (3) to assess natural and potential induced porewater advection; (4) to assess the distribution of erratic boulders on the sediment surface; (5) to assess the natural seismicity of the area; (6) to investigate the geotechnical properties of the sediments. One other important objective was to determine the degree of lateral homogeneity in the area. This requires a combination of seismic profiling and coring, and since our Dutch colleagues had far and away the best data sets in these areas, we have largely left such studies to them. However, we have kept in close touch with their work through the SWG and personal contacts and we have also analysed our own, smaller collections of data with the same objectives. We report on both our own and the Dutch findings later in this report.

Early in 1983 the Dutch reported observations of 'fault-like features' within the sediments at GME (Duin & Kuijpers, 1983). This observation caused considerable interest and debate, for the nature and origin of the features were not immediately apparent. As a consequence, some time was devoted by us to studying those features during *Discovery* Cruise 134, and a more detailed study of them was carried out during *Discovery* Cruise 144 (January-February 1984) as this report was being prepared.

Table 1.1 presents all the IOS stations in GME classified by measurement type and cruise; Table 1.2 gives the IOS stations in numerical order. Figure 1.1 shows all the tracks (IOS and RGD) in the area on which geophysical profiles were taken; and Figure 1.2 shows the positions of all stations (IOS and RGD).

TABLE 1.1 - IOS Stations and geophysical measurements in or near GME (by station type)

CRUISE	DATES	GLORIA (km^2)	2.2/3.5 kHz PROFILING (km)	AIRGUN SEISMIC PROFILING (km)	PISTON CORE	KASTEN CORE	GRAVITY CORE	SURVEY CAMERA	NEAR-BOTTOM PROFILER	EPIBENTHIC SLEDGE	HEAT FLOW	EARTHQUAKE SEISMOLOGY	ARTIFICIAL SOURCE SEISMOLOGY	PENETRATORS
Discovery 118	Feb-Mar 1981	-	Between Stations	500	-	D10321 D10325	D10320 D10323	D10319	D10329	D10328	D10318	D10304 D10317 D10322 D10327	D10303	-
Farnella 3/81	Nov 1981	20,000	-	1000	-	-	-	-	-	-	-	-	-	-
Discovery/ Shackleton 126	Mar-Apr 1982	-	Between Stations	-	-	D10406 S126/2 S126/4	-	S126/6	D10407 D10408	-	D10405 S126/3 S126/5	-	-	
Discovery 134	Mar 1983	-	✓	-	D10688 D10695 D10698 D10699	D10684 D10690	D10688 D10695 D10697 D10698 D10699	D10678 D10689 D10693	D10676 D10683 D10685 D10691 D10696	D10677	-	-	-	D10686 D10687

TABLE 1.2 - IOS Geology and Geophysics Stations in or near GME (numerical order)

STATION NUMBER	LATITUDE	LONGITUDE	DEPTH (m)	STATION TYPE
D10303	32°35.0'N	22°30.0'W*	5262	Artificial source seismology
D10304	32°59.6'N	24°54.1'W	5388	Earthquake seismology
D10317	31°04.1'N	25°49.2'W	4961	Earthquake seismology
D10318	31°15.0'N	25°43.0'W*	5433	Heat flow
D10319	31°15.0'N	25°43.0'W*	5433	Survey camera
D10320	31°05.2'N	25°50.0'W	5005	Gravity core
D10321	31°04.8'N	25°49.3'W	4978	Kasten core
D10322	30°20.3'N	24°06.8'W	5405	Earthquake seismology
D10323	30°21.7'N	24°06.8'W	5406	Gravity core
D10325	30°22.9'N	24°05.8'W	5407	Kasten core
D10327	32°36.3'N	21°56.7'W	5238	Earthquake seismology
D10328	30°25.0'N	24°05.0'W*	5412	Epibenthic sledge
D10329	30°21.0'N	24°06.0'W*	5402	Near-bottom profiler
D10405	33°30.0'N	22°59.0'W*	5410	Heat flow
D10406	32°34.7'N	22°27.3'W	5268	Kasten core
D10407	30°51.0'N	22°52.0'W*	5225	Near-bottom profiler
D10676	31°24.2'N	24°34.0'W*	5428	Near-bottom profiler
D10677	31°23.4'N	24°29.0'W*	5429	Epibenthic sledge
D10678	31°23.8'N	24°34.6'W*	5422	Survey camera
D10683	31°21.5'N	24°44.0'W*	5432	Near-bottom profiler
D10684	31°21.9'N	24°45.3'W	5434	Kasten core
D10685	31°18.0'N	24°44.0'W*	5434	Near-bottom profiler
D10686	31°25.5'N	24°44.5'W	5433	Penetrator
D10687	31°23.5'N	24°02.7'W	5428	Penetrator
D10688	32°03.0'N	24°12.1'W	5428	Piston and gravity core
D10689	32°39.5'N	24°19.5'W*	4871-5422	Survey camera
D10690	32°40.8'N	24°22.3'W	5421	Kasten core
D10691	32°00.5'N	24°12.0'W*	5429	Near-bottom profiler
D10693	31°39.9'N	24°48.3'W*	5433	Survey camera
D10695	31°23.7'N	24°46.3'W	5433	Piston and gravity core
D10696	31°17.5'N	24°43.0'W*	5434	Near-bottom profiler
D10697	31°36.3'N	24°53.1'W	5433	Gravity core
D10698	31°38.2'N	24°49.8'W	5433	Piston and gravity core
D10699	30°43.8'N	24°29.0'W	5431	Piston and gravity core
S126/2	31°33.2'N	24°50.5'W	5446	Kasten core
S126/3	31°31.0'N	24°28.0'W*	5447	Heat flow
S126/4	31°31.7'N	24°25.3'W	5446	Kasten core
S126/5	31°30.0'N	24°28.5'W*	5444	Heat flow
S126/6	31°09.9'N	23°48.5'W*	5418	Survey camera
S126/7	30°37.7'N	22°17.2'W	5095	Gravity core
S126/8	30°36.8'N	22°24.4'W	5116	Gravity core
S126/11	30°51.1'N	22°51.9'W	5223	Gravity core
S126/12	30°52.5'N	22°51.1'W	5241	Gravity core
S126/15	30°22.0'N	23°35.0'W	5330	Kasten core

* Mean position

FIGURE CAPTIONS

Figure 1.1 Ship's tracks on which underway geophysical data were collected in GME. (SRP = Seismic Reflection Profiling with air- or water-gun.) Lettered sections are locations of profiles shown in Figures 3.8-3.10. (Profile KL extends slightly beyond southern boundary of figure in direction indicated by arrow.) Stipple indicates area not covered by GLORIA sonographs.

Figure 1.2 Positions of stations in GME.

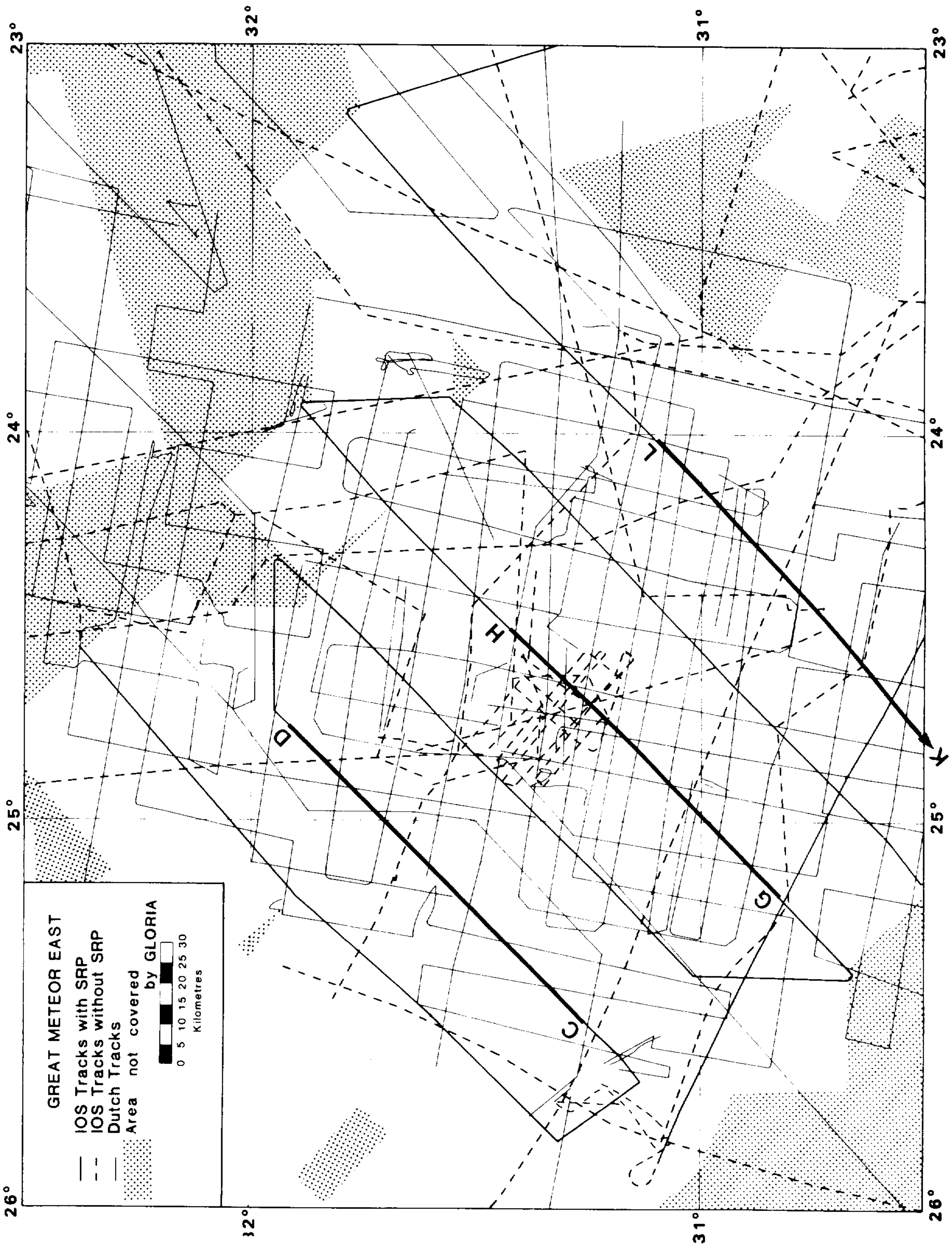

Figure 1.1 Ship's tracks on which underway geophysical data were collected in GME. (SRP = Seismic Reflection Profiling with air- or water-gun). Lettered sections are locations of profiles shown in Figures 3.8 to 3.10. (Profile KL extends slightly beyond southern boundary of figure in direction indicated by arrow.) Stipple indicates area not covered by GLORIA sonographs.

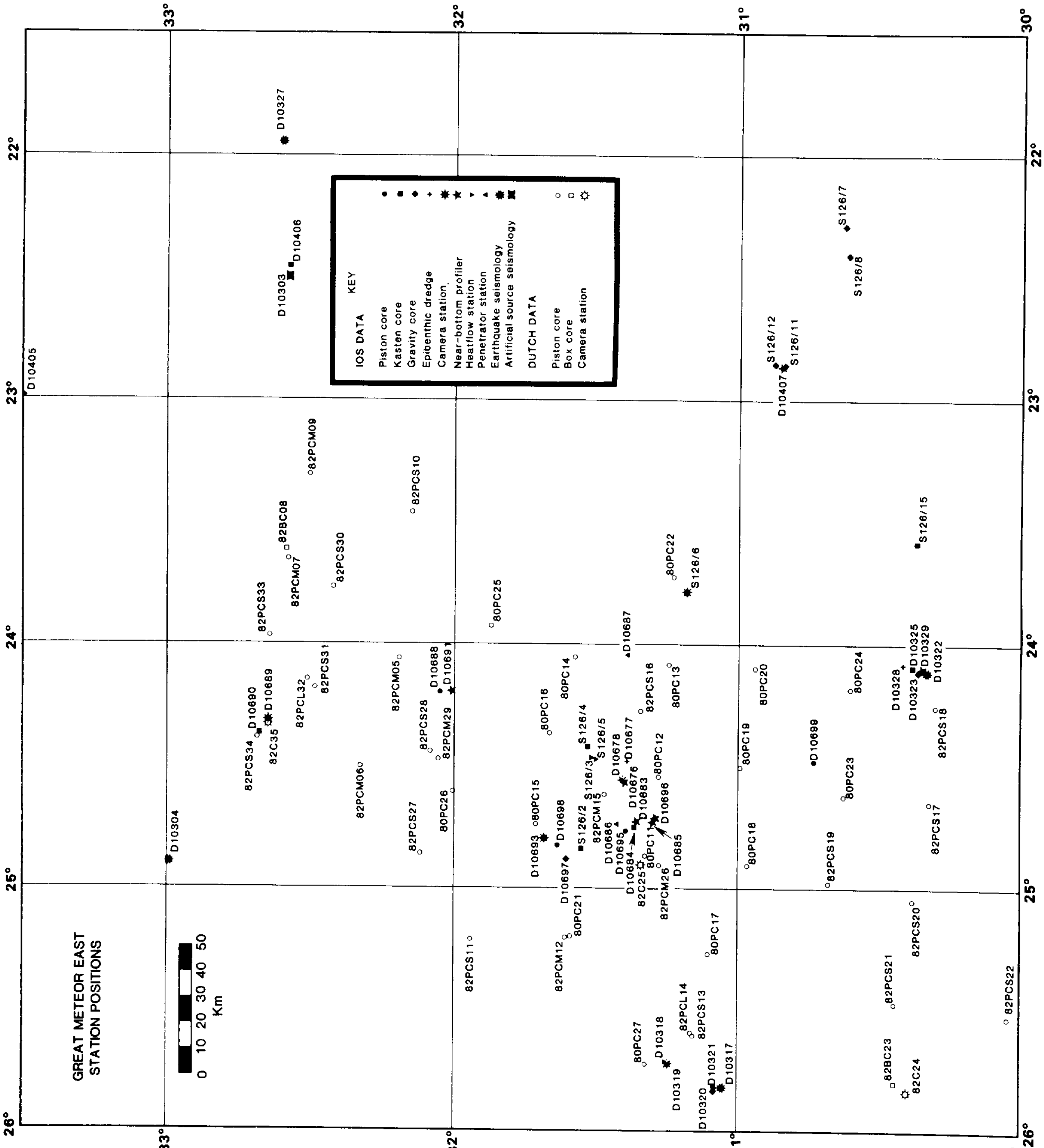

Figure 1.2 Positions of stations in GME.

2. REGIONAL SETTING

2.1 Physiography

Great Meteor East is situated on the Madeira Abyssal Plain in the centre of the Canary Basin (Fig. 2.1). Immediately to the west of GME the abyssal plain abuts against the lower flank of the Mid-Atlantic Ridge, which is characterised by numerous abyssal hills elongated in a NE-SW direction. The western boundary of the abyssal plain trends NNE-SSW along the base of the Ridge flank. Fracture zone valleys cut through the abyssal hills at right angles to this general trend, and in the valleys fingers of the abyssal plain stretch westward into the Ridge flank.

Between 150 and 250 km west of GME is a line of major seamounts extending from Great Meteor Seamount in the south (30°N, 28.5°W) through Hyeres Seamount to the Irving/Cruiser Seamount complex near 32°N, 28°W (Ulrich, 1969; Verhoef & Collette, 1983; Verhoef, 1983). All reach to within less than 300m of the sea surface; moreover, Great Meteor has an extensive flat top (i.e. it is a 'Guyot' or 'Tablemount') which was almost certainly produced by wave erosion at or near sea-level in the relatively recent past.

The Mid-Atlantic Ridge axis, running 600-800 km NW of GME, is the western boundary of the Canary Basin and is also the boundary between the North American and African tectonic plates. The basin's northern boundary is the Azores-Gibraltar Rise, part of a fracture zone separating the Eurasian and African tectonic plates (Laughton & Whitmarsh, 1974). This feature passes within 500 km to the north of GME. The northern margin of the Madeira Abyssal Plain is near 34°N, about 200-250 km NNE of GME.

To the north-east the Canary Basin is bounded by the Madeira-Tore Rise, a broad feature rising above 3000m and culminating in Madeira and Porto Santo islands. Its closest point is about 250-300 km east of GME. To the east it is the platform of the Canary Islands, and to the south the Cape Verde Rise, 1000 km away, that bound the basin.

The central and deepest part of the Canary Basin is occupied by the Madeira Abyssal Plain, a narrow strip of flat seafloor about 200 km wide. Its eastern edge includes the lowermost parts of the Madeira-Tore Rise, the Canaries insular rise and the Saharan (NW African) continental rise. Often this boundary is gradational, especially around its southern and northern edges, although immediately to the east of GME it is marked by a sharp change of slope from the very gentle gradient of the rise (about 1:300 to 1:1000) to the virtually flat (<1:2000) abyssal plain.

2.2 Oceanic basement

Great Meteor East and its environs appear to be underlain by normal oceanic igneous crust. Ewing & Ewing (1959) and Le Pichon et al. (1965) reported a seismic refraction line (their station D-5) which lies in the NE corner of GME and gave normal crustal thickness and normal velocities (Schreiber & Fox, 1973) for oceanic layer 3 and the mantle (Table 2.1). A second station (D-6) 200 km ENE of GME on the southern end of the Madeira-Tore Rise also gave a normal layer 3, but no mantle refractions were observed (Ewing & Ewing, op. cit.). Their station A-180-7, on the flank of the Mid-Atlantic Ridge 200 km N of GME, gave normal crustal thickness and layer 2 and mantle velocities. The layer 3 velocity was abnormally low at 6.2 km s^{-1}, but in the absence of further evidence there is no reason to believe that the crust is abnormal there. Station V-10-9, 250 km W of GME, also gave a completely normal oceanic structure (Ewing & Ewing, 1959; Le Pichon et al., 1965), as did three other stations in the Canary Basin within 1000 km of GME (Ewing & Ewing, 1959 (D-13); Udintsev et al., 1976, 1977).

The Madeira-Tore Rise is probably an aseismic oceanic ridge produced by excess volcanism at the spreading centre when it was formed in the lower Cretaceous (Tucholke & Ludwig, 1982).

The Deep Sea Drilling Project (DSDP) drilled to basement at Sites 136 (160 km N of Madeira) and 137 and 138 (500 km SSW of GME), and bottomed in normal oceanic basalt in each case (Hayes, Pimm et al., 1972). No other sites have been drilled within 800 km of GME. However, mention should be made of the results of DSDP site 141 on the lower continental rise on the southern margin of the Canary Basin (19°N, 24°W). This site investigated a 'piercement structure' that had previously been interpreted as a salt or possibly mud diapir. No trace of salt was seen, and the hole bottomed in highly-altered basalt (Hayes, Pimm, et al., 1972). It is possible, though perhaps not probable, that the structure is therefore an igneous intrusion.

Seismic reflection profiles across the Canary Basin show that the basement topography is quite normal (Collette et al., 1984; section 3.2). The basement displays the typical ridge-and-trough fabric of ocean crust, the fabric being aligned roughly NNE-SSW, parallel to the axis of crustal spreading. This fabric is cut by deep, linear fracture zone valleys that run WNW-ESE and are spaced about 100 km apart (Collette et al., 1984).

To the west of GME is a regional depth anomaly, centred on the Great Meteor Seamount complex, where the observed depth of the basement is up to 2000 m shallower than expected (Verhoef, 1984). GME lies on the eastern flank of this anomaly, where it has a value of a few hundred metres only (everywhere less than 500 m).

Most of the Madeira Abyssal Plain lies within the Cretaceous Magnetic Quiet Zone, so the crust cannot be precisely dated by magnetic anomalies. However, a compilation of magnetic anomalies by Collette _et al_. (1984) suggests that anomaly 34 (84 My bp) just passes through the NW corner of GME near 32°N, 26°W. The next anomaly to be recognised is M2 (116 My) near 30°N, 21°W (Perry _et al_., 1981). Linear interpolation gives an age of 106 My for the SE corner of GME at 30.5°N, 23°W, since the crustal age increases in an east-southeasterly direction. The study area is therefore late-mid Cretaceous in age, spanning the Santonian to Hauterivian stages. This would mean that the crust was accreted at a typical 'slow' spreading rate of about 15 mm y^{-1}. This is consistent with the observed rugged basement topography, which is also typical of slowly spread ocean crust. (The absolute ages given above are based on a Mesozoic magnetic time scale (Miles & Masson, pers. comm., 1984) that combines the magnetic stratigraphy of Harland _et al_. (1982, Chapter 4) with the revised stratigraphic timescale of Kennedy & Odin (1982)).

2.3 Volcano-tectonic setting

As mentioned above, the Canary Basin is bounded to the north and west by active tectonic plate boundaries. Seismic and volcanic activity is very localised along the boundaries, which are no more than a few tens of kilometres wide, and it is considered very unlikely that GME will be affected by processes at those boundaries.

However, there is evidence of seismic and volcanic activity, albeit at a lower level, within the Canary Basin. Lilwall (1982) has studied intraplate seismicity in the Atlantic, and for convenience divided the ocean into a number of regions. The Canary Basin lies in his region C for which the expected number of events per square kilometre per year with body wave magnitude $m_b > 4.5$ is $(13.5 \pm^{8.5}_{5.7}) \times 10^{8}$, where the ± values are 90% confidence limits. This is within the range found for the North Atlantic (excluding plate boundaries) as a whole. This would predict, for example, the occurrence of about twelve such events in a 30 km-square disposal site during a 100,000 year period. The frequency falls off by a factor of ten for each unit increase in magnitude.

Lilwall (1982) also estimated return periods for peak accelerations based on the observed seismicity for the whole North Atlantic excluding plate boundaries.

For accelerations of 0.1, 0.25 and 0.5 g he found return periods of the order of 10^4, 3 x 10^4, and 10^5 years, respectively, assuming uniformly distributed seismicity. If the seismicity is localised along faults, the return periods would be shorter than this for sites on the faults (minimum return period is 2000 years for 0.1 g peak acceleration with faults 200 km apart) and longer for sites between the faults. 0.1 to 0.15 g has been estimated as the lower limit of acceleration required to cause slope failure on land (Seed & Idriss, 1971); the corresponding value for marine sediments is unknown, although one empirical study on pelagic marls and oozes in the Mediterranean suggests that a similar value may be appropriate (Kastens, 1984).

The evidence for intraplate volcanic activity is the existence of recently active volcanic islands such as Madeira, the Canaries and Cape Verde islands, and of the Great Meteor-Cruiser seamount chain which probably post-dates crustal formation. The best studied of the islands are the Canaries. These are clearly of oceanic character (Bosshard & MacFarlane, 1970; Banda et al., 1981; Schmincke, 1979, 1982). The same seems to be true of the Azores (Ridley et al., 1974; Searle, 1976, 1980) and there is no reason to doubt that it also holds for the Madeira and Cape Verde islands. In all of these islands the vast majority of the volcanic activity has been quite recent. Schmincke (1982) concludes that the Canaries formed "chiefly during the last 20 My", although there may have been some Oligocene or even Eocene activity in the eastern island of Fuerteventura. The volcanic rocks of Porto Santo (near Madeira) are 12-13 My old, and those of Madeira itself 0.7 to 3.05 My. Santa Maria in the Azores is 3.2 to 8.1 My, and the rest of the Azores is younger than that (Abdel-Monem et al., 1968, 1975; Ridley et al., 1974; Watkins, 1973; Schmincke, 1982). (However, the Azores probably are associated with the Africa-Eurasia plate boundary (Krause & Watkins, 1970; McKenzie, 1972; Searle, 1980), so are not strictly speaking intraplate volcanoes). Schmincke (1982) summarises these observations: "Age data presently available for island volcanism in the Eastern North Atlantic suggest episodes of high activity betweeen 18 and 10 My and 5 My to the present . . ."

Great Meteor Seamount also appears to have formed relatively recently on pre-existing oceanic crust that was generated at anomaly 34 time. Two basalts from the seamount are dated (Wendt et al., 1976) at 11 and 16 My (Miocene), and foraminiferal sediment from the summit is also Miocene (Pratt, 1963; Von Rad, 1974). The seamount is therefore at least of Miocene age. On the other hand studies of the gravity field over the seamount, which reflect the response of the underlying lithosphere to the superimposed load, suggest that the lithosphere was at least 20 My old when the seamount formed, i.e. its maximum age now is 64 My (Watts et al., 1975; Collette et al., 1984). Finally, Verhoef (1983) has shown that a buried volcaniclastic apron around the seamount cannot be much older than Miocene. It is therefore concluded that the seamount formed no earlier than 64 My b.p., and most probably in the Miocene.

Finally, although this will be very tentative, we can try to estimate an approximate probability of formation of new volcanoes. The total area in the Canary Basin covered by volcanic seamounts is about 6×10^4 km^2 (this includes the Great Meteor-Cruiser complex, the Plato and Atlantis Seamount complexes to its NW, and two unnamed seamounts to the north of Cruiser). If we also include Madeira, Porto Santo and the Canary Islands, together with their volcanic pedestals, the area comes to 11×10^4 km^2. This volcanism is not uniformly distributed throughout the basin but tends to occur in units of 10^4 km^2 (Great Meteor Seamount, for example, is about that size). We could therefore say that about eleven such volcanic units have been formed in the Canary Basin. The total area of the basin is some 4×10^6 km^2, so the probability of occurrence of a volcanic unit at any point within the basin at some time during its history is roughly $11/(4 \times 10^6)$ i.e. 2.8×10^{-6} km^{-2}. A minimum estimate of the probability of formation of a volcano per unit area per year is given by dividing this figure by the average age of the basin. That age is about 75×10^6 years and the corresponding minimum probability is 3.7×10^{-14} km^{-2} y^{-1}. A maximum probability is given by noting that virtually all of this activity has been confined to the last 20 My and is still going on. We therefore divide 2.8×10^{-6} by 20×10^6 to obtain a very approximate probability of occurrence during the last 20 My of 1.4×10^{-13} km^{-2} y^{-1}. Taking the example of a 30 km square disposal site, the probability of a new volcano forming within the site would be 1.3×10^{-5} over a 100,000 year period.

2.4 Sedimentary setting

The present-day carbonate compensation depth (CCD), below which calcium carbonate is too soluble to accumulate in sediments, is generally considered to be at about 4900-5300 m in the North Atlantic (Berger & Von Rad, 1972; Van Andel, 1975; Tucholke & Vogt, 1979), although our results suggest that at GME it is slightly below 5400 m (see Chapter 4). As a result, most abyssal hills and the flanks of the Mid-Atlantic Ridge are covered to a greater or lesser extent by a drape of pelagic carbonate, mostly foraminiferal and nannoplankton ooze. Very young crust and steep slopes are usually bare or thinly covered.

Generally these sediments are stable, but slumping probably occurs on steep slopes and from terraces directly above them, producing locally derived debris flow deposits at the feet of such slopes and pelagic turbidites which pond in the basins. Within the ridge flank and abyssal hills provinces such sediment flows probably do not travel more than about 10 km from their source. However, sediment slides travel more extensively from areas of large topographic relief; for example, the RGD has detected recent debris flows up to 70 km SW of Hyeres Seamount, near 31°N, 30°W (Kuipers, 1982; RGD, unpublished data).

Crust younger than about 20 My (about 300 km ESE of the Mid-Atlantic Ridge axis or 500 km WNW of Great Meteor Seamount; Perry et al., 1981) has probably never been below the CCD, so the total sediment column would be expected to contain only carbonates. Farther east, on older crust, it is likely that pelagic clays occur in some deeper parts of the column. Seafloor now below the CCD (about 4900-5500 m) is unlikely to be accumulating significant pelagic carbonates at present. These expectations are confirmed by results from Deep Sea Drilling Project (DSDP) sites 136, 137 and 138 (Berger & Von Rad, 1972; see Fig. 2.1 for site locations).

Significant quantities of mid-Tertiary siliceous sediments occur in DSDP holes 138 and eastwards (Holes 140 and 139), probably as a consequence of increased productivity adjacent to NW Africa; such sediments are rare at sites 137 and 136, although some siliceous sediments occur in the upper Cretaceous at site 137 because it was then under the equatorial high productivity zone (Berger & Von Rad, op. cit.).

The continental and insular slopes and upper rises off NW Africa consist mainly of Neogene sequences of pelagic carbonate overlying clay, siliceous, and terrigenous sediments (DSDP sites 136 and 139), all deposited on massive Jurassic carbonate platforms and Cretaceous deltaic deposits (Von Rad & Wissman, 1982). The lower rise began to receive terrigenous sediments, probably mainly emplaced by turbidity currents resulting from slope failures on the continental slope, in the early Miocene (sites 136 and 138; Berger & Von Rad, 1972; Von Rad & Wissman, 1982). Since then the rise has probably been prograding outwards, and its foot now lies near the eastern edge of GME.

The Neogene sequences of the continental slope and rise off the Spanish Sahara have been examined primarily using airgun and 3.5 kHz high-resolution seismic profiling. Embley (1976) described a major Late Quaternary submarine sediment slide (the 'Sahara' slide) that originated on the upper continental slope near the Canary Islands and the resultant 'tongues' of debris flows that reach downslope to the continental rise (Fig. 2.1). To the north Embley (1976) and later Jacobi (in preparation) mapped turbidity current channel systems that again originate on the upper continental slopes off the mainland and also on the insular slopes of major islands such as Madeira. Jacobi & Hayes (1982) have mapped similar sediment transport features on the rise south of the Canaries, and Kidd & Searle (1984) have traced these features to the foot of the Mid-Atlantic Ridge flank near 24°N, 26°W using the long-range sidescan sonar GLORIA.

GLORIA surveys of the Saharan slide show that its debris flow 'lobes' extend right to the edge of the abyssal plain (Simm & Kidd, 1984). One of these reaches 24°W at 30°50'N, right at the eastern edge of GME. GLORIA also shows sediment lineations (which probably indicate the presence of ribbons of sediment with a sand or coarse silt content) reaching 24°W at 31°10'N (see Section 3.2 and Figs. 3.3 and 3.4).

TABLE 2.1 - Seismic Refraction Stations near GME

STATION	LATITUDE N	LONGITUDE W	DEPTH (m)	LAYER 2		LAYER 3		Mantle V_p	$h_2 + h_3$ km	Approximate distance from GME (km)	Reference
				V_p kms^{-1}	h_2 km	V_p kms^{-1}	h_3 km				
D-5	31°55'	23°02'	5170			6.5		8.0	4.6	0	1
D-6	32°49'-32°51'	18°58'-18°55'	3450			6.6(R)				200	1
A-180-7	35°35'-35°00'	26°00'-26°05'	4020	4.5	2.3	6.2(R)	2.9	8.0(R)	5.3	200	1
D-13	32°50'-32°50'	34°46'-34°04'	3660	5.0	3.1	7.2(R)			$\geq$3.1	800	1
-	31°45'	34°38'	3750	4.4(S)		6.6(S)	1.8-2.0			800	2
-	21°21.5'	30°08.5'		3.8(S)	2.3	6.6(S)	$\geq$3.0		$\geq$5.3	1000	3
V-10-9	31°51'-31°51°	30°54'-31°23'	4300	5.1	1.5	6.9	4.6	8.5(R)	6.1	250	4

h = thickness of layer
V_p = compressional wave velocity
R = reversed
S = split
1 = Ewing & Ewing, 1959
2 = Udintsev *et al.*, 1976
3 = Udintsev *et al.*, 1977
4 = LePichon *et al.*, 1965

FIGURE CAPTION

Figure 2.1 Regional setting of GME. Outline bathymetry, simplified from Searle et al. (1982), in kilometres. Sediment mass-movement features compiled and simplified from Embley (1975, 1976); Jacobi & Hayes (1982); Kidd & Searle (1984); and Jacobi (unpublished chart). Fracture zones from Searle et al. (1982) and Collette et al. (1984).

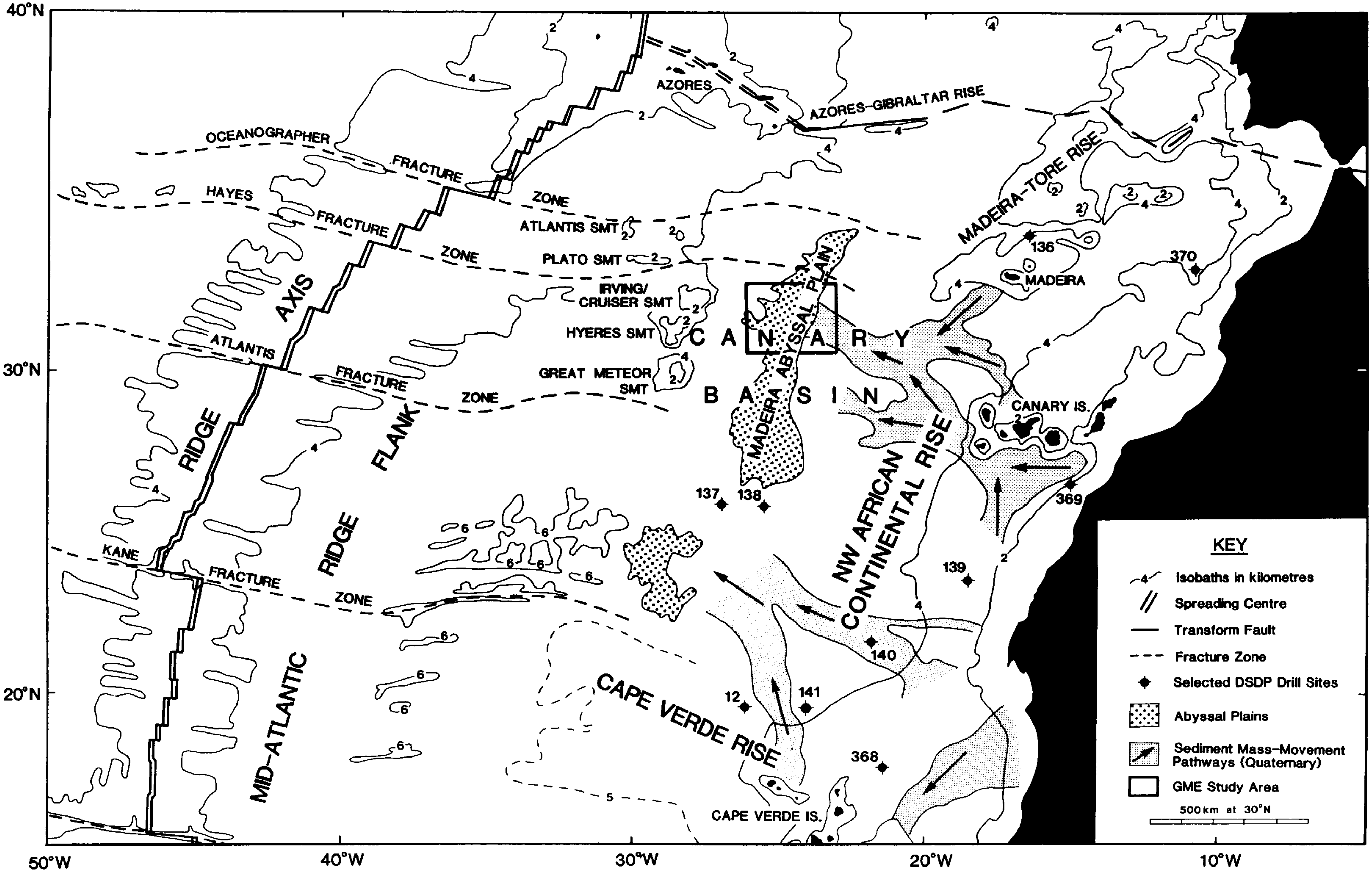

Figure 2.1 Regional setting of GME. Outline bathymetry, simplified from Searle et al. (1982), in kilometres. Sediment mass-movement features compiled and simplified from Embley (1975, 1976); Jacobi & Hayes (1982); Kidd & Searle (1984); and Jacobi (unpublished chart). Fracture zones from Searle *et al.* (1982) and Collette *et al.* (1984).

3. GEOPHYSICAL SURVEYS

A number of underway geophysical measurements have been made in GME. The long-range sidescan sonar GLORIA (Somers *et al.*, 1978) was used during the *Farnella* cruise, and provided nearly complete coverage (20,000 km^2) of the study area. Records were replayed at two different levels with and without automatic gain control (AGC). The non-AGC records were generally preferred, since they distort the signal amplitudes less. The high-level records reveal details recorded as very low-intensity signals, while the low-level replays reveal details within the high-intensity regions that otherwise saturate the photographic images. GLORIA resolution varies from 50 m down-range to 1 km along-track at maximum range of 30 km. The sonographs provide a detailed and accurate map of seabed structure, allowing both the production of improved bathymetric and outcrop maps, and also the examination of sediment facies distribution.

Single-channel seismic reflection profiling using airgun sound sources was run by IOS on *Farnella* 3/81 and *Discovery* 118, producing some 1600 km of record; the RGD has completed some 6750 km of single-channel seismics using a water-gun source, which has a broader-band signal and is richer in high frequencies than the airgun. Both airgun and watergun profiles reveal details of the subsurface sediment structure down to acoustic basement, but the watergun records have somewhat higher resolution. The IOS profiles employed either 0.33 litre (20 cubic inch), 1.31 litre or 2.62 litre airguns. The 1.31 litre source, which was used for the majority of the work, was deployed with a "wave-shape kit" which cuts down on the bubble reverberation and improves the resolution, at the expense of some penetration, and this combination gave us our best records. IOS data were replayed in two frequency bands: a high-frequency band (generally in the range 50-160 Hz) and a low-frequency band (generaly in the range 15-100 Hz). The high-frequency records obtained with the smaller airguns have a vertical resolution of about 20-40 milliseconds two-way acoustic travel time (equivalent to about 30 m) but may fail to show basement. The low-frequency records have much poorer resolution, but reveal the basement clearly. Details of the RGD equipment and techniques are given in Duin & Kuijpers (1983).

Both IOS and RGD have also carried out high-resolution profiling using 2.2 or 3.5 kHz sound sources. These systems have vertical resolutions on the order of a metre or two, but only penetrate the uppermost few tens of metres (in GME, typically 30-80 m). The RGD has recorded over 8000 km of 3.5 kHz profiles, mostly on a regular grid. IOS coverage is much less, in general being confined to passage tracks between and over stations (Fig. 1.1).

High-resolution profilers deployed near the sea-surface have poor horizontal resolution, generally having conical beams with half-angles of the order of 45°. They therefore have a 'footprint' on the seafloor that is many kilometres across, and can record echoes from features well off to the side of the ship's track. Low-frequency air- or water-gun systems are even worse, since their beams are essentially disc-shaped and have no directivity in the thwartships plane. In fact, for flat-lying reflectors profilers perform somewhat better than the simple beam-width argument suggests, because reflections well off-axis tend to interfere and cancel out. However, in order to improve the resolution, particularly for the more general case of non-flat reflectors, IOS has developed a high-resolution near-bottom profiler. This employs a broad-band (5 kHz-10kHz) acoustic source and has a relatively narrow beam (about 20° half-angle) and, because it is towed only a few tens of metres above the bottom, a much smaller footprint (<50 m). Its vertical resolution is about 20 cm. It has been deployed on all IOS cruises except *Farnella*, but was used most extensively on *Discovery* 134.

Magnetic field was measured on most IOS cruises using a proton precession magnetometer and was reduced to the appropriate International Geomagnetic Reference Field (IAGA, 1981; Peddie, 1982). Gravity was measured on the *Farnella* cruise since the instrument was already on board for other cruises, but has not been analysed for this report. Finally, all IOS cruises recorded 10 kHz echosounder data.

3.1 Magnetic Field

Contoured magnetic anomalies from IOS cruises are shown in Figure 3.1. On the flank of the Mid-Atlantic Ridge north and west of 31.5°N, 25.5°W we recognise high-amplitude anomalies (around 500 nT peak to trough) that are lineated NE-SW, roughly parallel to the present Mid-Atlantic Ridge and normal to the WNW-ESE Cretaceous spreading direction indicated by fracture zone trends (see below). These anomalies are interpreted as the Vine-Matthews-Morley seafloor spreading anomalies produced at the time of crustal generation. The negative anomaly at 32.3°N, 25.5°W is identified as anomaly 34 (Santonian/Campanian boundary, 84 My b.p.; see Section 2.2) by comparison with the anomaly identifications of Collette *et al.* (1984). Although this anomaly appears to be continuous with the one centred near 31.6°N, 26.2°W, the two are actually separated by a fracture zone, and a more likely identification of anomaly 34 south of the fracture zone is at 32.2°N, 26.3°W.

As stated in Section 2.2, GME itself lies within the Cretaceous Magnetic Quiet Zone. It is clear from Figure 3.1 that anomaly amplitudes are generally low and not significantly lineated over most of the area. Peak-to-trough amplitudes are mostly less than 200 nT. The only exceptions to this occur in the region of two fracture zones (located on the basis of the basement topography - see Section 3.3), which are characterised by lines of magnetic highs. This is especially apparent in the case of the southern fracture zone, where the anomalies may have amplitudes of over 400 nT peak-to-trough. Such positive magnetic anomalies are to some extent characteristic of fracture zones in the magnetic quiet zone, although their origin is not well understood (Collette _et al_., 1984).

3.2 Seabed Morphology

Figure 3.2 is a bathymetric chart of GME, based on all soundings available to us (see figure caption for data sources). Contouring between lines of soundings has been guided by form deduced from GLORIA images (see Fig. 3.3).

In the eastern part of Figure 3.2 we see the foot of the North West African continental rise. The regional slope is between 1 in 300 and 1 in 1000 down to the 5420 m contour. Below this depth the slope decreases abruptly to less than 1 in 2000, and west of 24°W the abyssal plain is flat to within about 10 m, at an average depth of 5440 m (see also Kuijpers, 1982).

Locally the abyssal plain is interrupted by abyssal hills a few hundred metres high and a few tens of kilometres across. They become more frequent and continuous to the west, north, and south. Those to the south represent the outcropping above the abyssal plain of the south wall of the southern of the two fracture zones that cross GME; to the west the increased frequency of hills reflects the beginning of the lower flank of the Mid-Atlantic Ridge. Narrow fingers of the abyssal plain extend westwards into the ridge flank along the lines of the fracture zones (e.g. at 31.3°N, 25.8°W and at 32.1°N, 25.3°W). The abyssal hills are generally elongated in a NE-SW to NNE-SSW direction, reflecting their origin by block-faulting at the Mid-Atlantic Ridge axis. This tectonic grain is clearly seen in the GLORIA imagery (Figs. 3.3, 3.4).

A combination of GLORIA and seismic reflection profiling (see sections 3.3 and 3.4) can be used to identify outcrops of basaltic basement (Fig. 3.5). It turns out that such outcrops are rare, most of the hills being covered by a drape of pelagic sediment. However, a few of them, especially those adjacent to the fracture zones, have spines of basalt outcropping along their crests.

GLORIA not only shows the major topography, but also responds to very small structures and texture at the scale of the acoustic wavelength. This has proved particularly valuable for studying variations in sediment facies on the seabed (Kidd et al., 1985). In particular, the rough surfaces of debris flows can be recognised as areas of relatively strong acoustic backscattering, and lineations in the backscattering pattern observed over an otherwise smooth seafloor indicate directions of sediment bed-transport (Kidd & Searle, 1984). The mechanism of the latter effect is not yet understood, however: the lineations may reflect variations in sediment grain size, porosity, sand-content, rippling, biological mounding, or even very small-scale channelling.

Nevertheless, the effects are very clear. Sonograph C in Figure 3.4 is from the lowermost continental rise, and includes the most distal parts of the Saharan sediment slide (Simm & Kidd, 1984). A small abyssal hill (with a spine of basaltic outcrop) is located at the centre of the sonograph, and clear lineaments can be seen in the sediment surface to either side of it. They fan out to the west of the hill, suggesting the fanning out of the bottom transported sediment load after passing the obstacle presented by the hill. Coring here reveals that the surficial sediments are fine-grained turbidites, but a massive sand unit occurs less than a metre below the seafloor (Kuijpers, 1982). The presence of this sand bed indicates rapid and possibly erosive bed-transport (Kidd et al., 1985).

Near the southwestern edge of sonograph C can be seen a small patch of moderately reflective seafloor surrounded by a darker region. Other sonographs in the region show this feature better and clearly reveal it as a distal lobe of the Saharan debris flow system (Kidd & Simm, 1984); Fig. 3.3). It can be traced for hundreds of kilometres up the continental rise to the east, but does not extend to the west of 24°04'W.

A few weak NW-SE sediment lineations occur between sonographs B and C (Fig. 3.3), reflecting the residual effect of vigorous bed-load transport here. However, no such lineations can be seen within the area of sonograph B. There are some much broader variations in acoustic backscattering intensity over the abyssal plain here, but these are orientated NNE-SSW and probably indicate subtle variations in sediment properties reflecting the underlying morphological grain of the basement. By the time one is as far west as sonograph A, virtually all variations in backscattering intensity have ceased, and the surface of the abyssal plain appears acoustically completely uniform.

3.3 Sediment thickness and basement morphology

The widely-spaced Farnella seismic reflection profiles do not by themselves allow an adequate contouring of sediment thickness in the area. We have therefore combined our data with the sediment thickness and depth-to-basement measurements of the RGD shown in enclosures 3 and 2 of Duin & Kuijpers (1983). In those figures, sediment thickness (h) had been inferred from one-way acoustic travel time (t) using the expression

$$h = V_0\{\exp(\bar{a}t) - 1\}/\bar{a} \qquad (3.1)$$

(Houtz & Ewing, 1963), and taking the average velocity gradient within the sediments ($\bar{a}$) to be given by the empirical relationships of Hamilton (1979, 1980) for calcareous sediments:

$$\bar{a} = 1.902 - 1.71t + 0.97t^2. \qquad (3.2)$$

V_0 was taken to be 1527.4 m s^{-1} (Duin & Kuijpers, 1983). We have used the same expressions to convert our travel times to depths, although we recognise that they may not be entirely appropriate for this area. Figures 3.5 and 3.6 show the results of contouring the combined data sets of total sediment thickness and depth to basement. Areas of basement outcrop were extrapolated from the seismic lines on the basis of the GLORIA sonographs, and in general contouring between lines was constrained to follow trends shown by GLORIA and the seabed topography.

Sediment thickness (Fig. 3.5) within GME varies from zero to over 2000 m. The greatest thicknesses occur in narrow basement valleys in the centre of the area and in the fracture zones. Sediment thicknesses in excess of 250 m characterise the majority of the area, including almost all of the area beneath the abyssal plain. Sediment thickness on the abyssal hills is generally less than 250 m. The total sediment thickness therefore closely follows the shape of the basement (compare Figs. 3.5 and 3.6).

The basement topography has a pronounced NNE-SSW grain which reflects its tectonic origin as discussed above. The total relief between these lineated valleys and ridges is about 1000 m. The present abyssal hills are clearly the culminations of the shallower basement ridges. Two prominent valleys cut across the main part of the area from WNW to ESE, and represent the traces of two inactive fracture zones. A third one can be seen near 32.5°N, between 23° and 24°W. The basement reaches depths of over 7000 m within these valleys, and is generally shallowest just above their rims. The main basin of GME thus lies between the two main fracture zones at 31°N and 32°N, and is bounded to the east by the continental rise at 24°W and to the west by the Mid-Atlantic Ridge Flank near 25°W.

3.4 Seismic Reflection Profiles

In this section we describe the seismic reflection profiles in some detail, and as far as possible infer the sub-surface sediment structure from them. The seismic character of the sediment column varies within and across the area, and we illustrate this by considering in detail three separate sections. These are all SW-NE sections, each approximately 50 miles long and all obtained during the Farnella cruise (Figs. 3.8 to 3.10). Throughout this discussion, for convenience we use the travel-time-to-depth conversion presented above to infer actual depths and thicknesses of units. However, we recognise that these conversions are not based on velocity determinations in this area and may be somewhat in error.

The relative attitudes of various lithologic units recognised in seismic sections may suggest the type of depositional environment. Usually, pelagic sediment accumulates by being draped fairly uniformly over the underlying topography, although it will fail to accumulate on steep slopes or may slump off them to form local debris flow deposits or turbidites in nearby basins. On the other hand, turbidites tend to pond in basins, forming initially horizontal beds that onlap the underlying topography to form a depositional unconformity; subsequently, the beds tend to be deformed as a result of differential compaction so that the deeper turbidite strata will tend to become more conformable with the underlying topography. Finally, while pelagic deposits tend to be uniform and therefore appear relatively featureless and transparent on seismic records, turbidites by virtue of rapid variations in grain-size and carbonate content tend to be characterised by strong acoustic laminations. However, departures from these simple identification relations are frequent, and direct interpretation of lithologies from seismic profiles must be regarded as highly speculative.

On the other hand, we can to some extent infer the likely lithologies at depth by considering the regional geology, particularly the depth of the seafloor in relation to the CCD. Pelagic sediment deposited above the CCD should contain a high proportion of calcium carbonate, while that deposited below it will have most of the carbonate dissolved and will consist mostly of clay minerals and very fine-grained quartz, etc. The variation with time of the North Atlantic CCD, as deduced first by Van Andel (1975) and then by Tucholke & Vogt (1979), is shown in Figure 3.7, together with a predicted age-depth curve for 92 My-old seafloor, assuming that the basement sank by thermal contraction in the usual way (Sclater

& Francheteau, 1970; Parsons & Sclater, 1977). The figure illustrates a particularly simple hypothetical sedimentation history; other possible models are discussed below.

We use these considerations in the following sections to interpret the reflection profiles, but we emphasise that there is no independent control by sampling below a depth of 22 m. Positions along profile are denoted as a/bZ, where a is the Julian day number and b is the time in hours and minutes; Z indicates Greenwich Mean Time.

Profile CD (Example section 314/0730-314/1400 Z; Figure 3.8)

Oceanic basement can be clearly recognised on both the low-frequency and high-frequency records over most of this profile. In the section illustrated it ranges from depths of 7.93 s (about 6100 m) below sea level at 1100 Z to 7.10 s (5340 m) at 0925 Z. The basement reflector is typical of that normally associated with the top of the basaltic crust.

Basement is immediately overlain by a seismic unit that grades from moderately transparent (0745-0820 Z; 0840-1020 Z; 1140-1330 Z) to strongly layered (0820-0840 Z; 1020-1140 Z), with the latter character being more common in the deeper areas. In general, this lowermost unit is draped over the basement, though locally it onlaps it or abuts sharply against it at steep basement slopes (e.g. 1020-1030 Z; 1120 Z; 1130 Z). Duin & Kuijpers (1983) recognise a "lower stratified unit C" which contains closely-spaced, strong reflectors, and which probably corresponds to the layered unit described here, but they do not mention variations in its degree of stratification. They also refer to a "basal transparent sediment unit D" underlying unit C, but that is absent or at best very poorly developed on profile CD (it may be present, and about 100 ms thick, at 0745-0810 Z). It is just possible that the transparent unit between 1140 and 1330 Z is unit D, and is onlapped by C near 1140-1145 Z; but the stratigraphic relationship is not entirely clear there, and we think it is more likely to be a facies change.

The basement along this profile is approximately Turonian in age (~92 My old), so any parts of it shallower than 5600-6000 m were probably above the CCD at and shortly after their formation; however, the deeper parts of the basement must have been near or below the CCD then (Fig. 3.7). All of the basement should have dropped below the CCD by about 80 My b.p., although it would have been briefly above it again during the Maastrichtian (65-70 My b.p.). We therefore expect most of the basal unit here to consist of pelagic clay, although some of the shallower parts may be predominantly carbonate. Very speculatively, the acoustic laminations in the deeper areas could result from variations in grain size or carbonate content in local (pelagic) turbidites, slumps or debris flows, from volcaniclastic deposits, or fluid lava flows. Similar interpretations have been suggested for this unit by Duin & Kuijpers (1983), and for similar units in Nares Abyssal Plain (NAP) by Tucholke et al. (1983).

This lowermost unit (C) reaches a maximum thickness of 260 to 300 ms or about 300 m (0810 Z; 1045-1100 Z; 1215 Z; 1310 Z). In the deeper parts, especially where it is laminated, it is capped by a strong, prominent, regional reflector, which is Reflector 4 of Duin & Kuijpers (1983). If most of the sediment below Reflector 4 is clay then the reflector could be quite young, though the average sedimentation rate must have been greater than 300 m in 92 My, i.e. 3×10^{-6} my^{-1}, which is rather high for pure pelagic clay. However, if a substantial portion of these deep sediments are more rapidly deposited carbonates then the reflector could be considerably older. If the unit were entirely carbonate deposited at 20×10^{-6} my^{-1}, Reflector 4 could be as old as 80 My. An intriguing possibility is that the reflector arises from Maastrichtian carbonates laid down during the brief depression of the CCD at that time (Fig. 3.7). Reflector A* in the northwest Atlantic had that origin (Tucholke & Mountain, 1979) and appears very similar to our Reflector 4.

Overlying Reflector 4 is a unit that is weakly stratified at its base, but grades upwards into an acoustically strongly laminated unit whose top is at the seafloor. The upper (stratified) and lower (non-stratified) parts of this unit correspond to units A and B, respectively, of Duin & Kuijpers (1983), but we see no obvious boundary between the two. We therefore refer to the whole unit as AB. In the deeper parts of the basins it appears to be conformable with Reflector 4 and the underlying Unit C (e.g. 0800-0830 Z; 1045-1110 Z), but near the margins of the basin, and especially where Reflector 4 is weak or absent, it clearly onlaps unit C (1150-1210 Z). The unconformity between units AB and C, coupled with the generally sub-horizontal attitude of the internal reflectors in unit AB, strongly suggest that AB consists mainly of ponded turbidites interlayered with pelagic sediments. The lack of strong acoustic laminations in its lower part may be the result of increasing attenuation of the seismic signal with depth, as suggested by Tucholke et al. (1983) for a similar acoustic unit in the Nares Abyssal Plain.

Within unit AB the near-surface reflectors are horizontal, but deeper ones are progressively inclined so that near the base of this unit the reflectors are tending to be conformable with the top of Unit C. However, as stated above, they are definitely unconformable on C near the basin margins (1210-1330 Z). We attribute this progressive bending of the reflectors to differential compaction.

We recognise a prominent, almost continuous reflector at depths of 100 to 150 ms (80-120 m) beneath the seafloor. This corresponds to Duin & Kuijper's reflector 2. It is deepest at the centres of the basins and shoals towards their edges, where it appears to lap on to the underlying pelagic units (0845 Z; 1015 Z).

Duin & Kuijpers (1983) interpret reflector 2 as the base of the uppermost turbidites (their unit A) and recognise a transparent unit (B) below it. However, although the resolution of our records is poorer than theirs, we see similar closely-spaced reflectors both above and below reflector 2. Six distinct parallel lines of energy peaks, conformable with reflector 2, can be seen in an interval of 110 ms beneath it near 1100 Z, and not all of these can be source or internal reflection multiples. (On this profile the basic air-gun source signal is a strong, equally spaced triplet covering a total of 40 ms two-way time.) Also, there is no obvious unconformity between units A and B, whereas there is between B and C. We therefore believe that the turbidites extend to at least 250 ms (210 m) beneath the seafloor in this region, and probably, as argued above, right down to Reflector 4.

The lowermost of the strong reflectors in unit AB, at 200-290 ms beneath the seafloor, may correspond to Duin & Kuijper's Reflector 3. It is at about the right depth, but we do not recognise a distinct reflector here apart from those belonging to the overlying section. This lowermost strong reflector appears to be generally conformable with the weaker reflectors in the underlying transparent unit (B), but we do recognise minor unconformities in places (e.g. 0740 Z).

Unit AB has a maximum thickness of 450 ms (410 m) along profile CD. If we assume that throughout the unit the sedimentation rate was similar to the 46 x 10^{-6} to 105 x 10^{-6} m y^{-1} measured over the last 190,000 years in cores (section 4.5), then it represents a depositional period of between 3.9 and 8.9 My. Weaver & Kuijpers (1983) have shown that individual GME turbidites correlate with interglacial changes of sea level, suggesting that major turbidite sedimentation began here at the onset of glaciation (about 2.4 My b.p. according to Kidd et al, 1983b). If this is correct, our identification of unit AB as turbidites would imply a sedimentation rate of up to 170 m y^{-1} for it on this profile. This is higher than currently observed, but it is possible that thicker turbidites were deposited in the early history of the abyssal plain, since the area of ponding would then have been smaller.

Above reflector 2 we see considerable along-profile variations in reflector strength and continuity. We show later in this report that for 3.5 kHz records acoustic reflectors generally correlate with the silty bases of turbidites. The airgun wavelength is much longer than the average turbidite spacing, but variations in physical properties of turbidites may still affect reflections indirectly. If so, then the variations referred to in the profiles may indicate variations in the silt content or grain size, possibly reflecting control of turbidite deposition by very small scale (~1 m) variations in the relief of the seafloor. Another possibility is that individual reflections are formed by interference between rays reflected from very closely-spaced features, and that variations in the reflections are due to small-scale variations in the bed spacing. Finally, some of the areas of more broken reflectors may result directly from small-scale relief such as channels. However, we see no evidence of faulting or fault-like features within the sediments on this profile.

Profile GH (Example section 315/0700 Z-315/1300 Z, Fig. 3.9)

This profile is about 50 km SE of CD, and the basement here has a mean age of approximately 95 My. Oceanic basement is clearly recorded over most of the profile, although in the deeper parts it is difficult to interpret without the help of the low-frequency recordings. It is shallowest (6.68 s or 5040 m below sea level) at the top of the scarp overlooking the southern fracture zone (0735 Z), drops to 8.03 s (6230 m) within the fracture zone (0820 Z), and reaches its greatest depth around 1120 Z. This latter is one of the deepest occurrences of basement in the area, except for the fracture zone valleys. In profile the steep basement scarp at 1110 Z looks very like a fracture zone, but if so it was shortlived, since it does not extend more than about 40 km in an E-W direction (Fig. 3.5, 31.2°N, 24.4-24.8°W).

Reflector 4 is recognised on this profile at a maximum depth of 600 ms (580 m) below the seabed; this is somewhat deeper than on profile CD. The reflector shoals towards the margins of the basement depressions (0900 Z, 1045 Z), and possibly occurs as high as 280 ms (240 m) at 0920-0930 Z.

The seismic units between the basement and reflector 4 are rather different from those in section CD. Another reflector occurs intermittently about 150 ms (150-160 m) below reflector 4. It is roughly equal in strength to reflector 4, and typically contains 4-5 energy peaks spanning about 110 ms. We take the sediments between this and Reflector 4 in most places to be the (pelagic?)

unit C, and find that it is generally acoustically laminated, and is draped over moderate underlying topography (0850-0930 Z; 1230-1300 Z) or abuts against steep basement slopes (0740 Z; 1110 Z). Below this is a generally transparent unit, probably Duin & Kuijper's Unit D, which has occasional reflectors within it (e.g. at 8.28 s at 1130 Z), and so far as we can see is conformable with C.

Over the deeper parts of the basement most of the sediments below reflector 4 appear to be ponded rather than draped, and may here contain substantial proportions of turbidites or other bed-transported sediment, possibly locally derived (e.g. 1110-1130 Z).

Above reflector 4 the sediment column is very similar to that in section CD. Reflector 3 occurs at depths of 190-280 ms, and 2 occurs at 120-190 ms; both ranges are almost identical to those in section CD, although the total thickness of AB is in fact slightly greater here (Table 3.1).

One further difference between sections CD and GH is that in the latter we begin to recognise vertical discontinuities in the sediment column that have been interpreted as possible faults (Duin & Kuijpers, 1983; Duin et al., 1984). Examples are seen at 1207 Z and 1220 Z. Here there are near-vertically aligned discontinuities in the reflectors lying between Reflector 2 and Reflector 4. Reflector 2 is slightly kinked but we cannot resolve any offset in it, and the reflectors above it are unaffected. However, there are small offsets of about 10-20 ms in the deeper reflections, sometimes accompanied by zones of focussed or defocussed acoustic energy, down to about reflector 4, below which it is impossible to resolve the structure adequately. Because of the inherent resolution limitations of the reflection profiling method this is only indicative of steep slopes, and not necessarily of physical discontinuities, in the actual reflectors. We attribute these fault-like features to the effects of differential compaction (see section 3.5).

Profile KL (Example section 316/1000-316/1800 Z; Figure 3.10)

This is the easternmost of the Farnella profiles, over crust with a mean basement age of 98 My. On this section basement depths are similar to those of section GH, reaching a maximum of 1400 ms below the abyssal plain (7100 m below sea level) in the southern fracture zone valley (1410 Z). Again the greatest depths are best seen on the low-frequency record.

Reflectors 2, 3 and 4 are all somewhat shallower than on section GH, lying in the ranges 90-160 ms, 120-200 ms and 150-440 ms, respectively. The sediments above Reflector 4 (unit AB) are generally unconformable with those below it (unit C), as can be seen for example at 1030-1040 Z, 1200-1230 Z and 1340-1350 Z. At the edges of the basin the unconformity is time-transgressive and reaches the surface of the abyssal plain, for example, as the pelagic-sediment/turbidite contact at the foot of the abyssal hill at 1015 Z.

To the southwest of the point at 1410 Z, Reflector 4 has much the same appearance as on the more westerly profiles. However, to the northeast of this point the reflector becomes increasingly broken up into a band of small diffractions, and to the northeast of 1700 Z it becomes quite indistinct. Further to the northeast it recovers some, but not all, of its former clarity. The major disturbed band extends from 31°00'N, 24°05'W to 31°20'N, 23°44'W on this profile, and from 31°20'N, 24°10'W to 31°28'N, 24°02'W on the next profile west (IJ, not illustrated). This corresponds roughly to the position of the toe of the Saharan Sediment Slide (Section 3.2). It is unlikely that the changes in reflector 4 are direct effects of that slide (e.g. by increased acoustic scattering near the sediment surface), since the reflectors above 4 are unaffected and the slide does not extend to profile IJ. However, these changes in the reflector may indicate some earlier disturbance in the same region.

Several other reflectors can be discerned below Reflector 4, of which the main ones are indicated in Figure 3.9b. Some of these mark unconformities. These deeper reflectors are less continuous than the overlying ones, and do not obviously correlate with each other along the profile. Most of them are actually bands of closely-spaced reflections, and the units between them vary from acoustically well-laminated to almost 'transparent'. The transparent unit just above basement at 1300-1330 Z may be unit D, but elsewhere the identification of the deeper units is very uncertain. The laminated sediments just above the basal unit here appear to onlap it, and may therefore represent deep, basin-fill turbidites, though this interpretation is very tentative.

Above reflector 4 the sedimentary units are similar to their counterparts further west. The main difference is that they are somewhat thinner. Unit A and unit B are both thinner than on sections GH or CD (Table 3.1). These uppermost units also contain more fault-like features than on profile GH. The appearance of these features is similar to those on that profile except that in several cases they can be seen to extend some distance above Reflector 2. This may be due, at least in part, to the fact that profile GH was recorded with a slightly higher frequency filter (80-250 Hz). However, we cannot resolve any discontinuity shallower than about 100 ms below the seafloor on this profile.

Summary of seismic reflection profiles

We recognise two major, regional reflectors - Reflectors 2 and 4 of Duin & Kuijpers (1983). We interpret Reflector 4, at a depth of generally 200 to 400 m (but locally up to 560 m) below the seabed, as marking the base of the turbidites (unit AB) in the western part of the region and in areas of shallower basement. We provisionally interpret the bulk of the sediments below Reflector 4 in these areas as pelagic, probably predominantly clay. Elsewhere, especially where the basement is deep, turbidites appear to extend much deeper into the section, although many of these may be pelagic, not terrigenous, turbidites. Reflector 4 generally marks an unconformity (between pelagics and turbidites), but Reflector 2 does not. We are unable at present to date either reflector with any degree of precision.

Sub-units A and B both have similar thickness ranges in the west and central parts of the region, but they thin somewhat to the east (Table 3.1). This is consistent with their being turbidites derived from the east and ponding in central and western GME. The denser seismic data of Duin & Kuijpers (1983) show that the topography of Reflector 4 is a subdued version of that of the basement, as would be expected if unit AB consists of basin-fill turbidites. The relief on Reflector 4 is about 300 m. By contrast, Reflector 2 has a relief of only about 50 m, but again it roughly follows, in a subdued way, the shape of the basement and of Reflector 4.

Vertical discontinuities in the sediment column appear to be absent in the western part of the region but become more common eastwards (Fig. 3.11). Observable offsets of reflectors across these features do not exceed about 20 m, and none has been seen to come shallower than about 100 m on the airgun profiles, though they can be seen at shallower levels on some 3.5 kHz records (see below).

3.5 High-resolution seismic studies

In addition to air-gun seismic profiling, we have also carried out a certain amount of high-resolution profiling using a surface towed 3.5 kHz source and a deep-towed wide-band (5-10 kHz) source. However, the RGD has carried out the bulk of the 3.5 kHz profiling in the area, and this has been reported by Kuijpers (1982) and Duin & Kuijpers (1983).

We can divide the information obtained from these high-resolution records into three categories: sediment facies inferred from acoustic echo character; distribution of closely-spaced near-surface reflectors; and distribution of near-vertical discontinuities or faults.

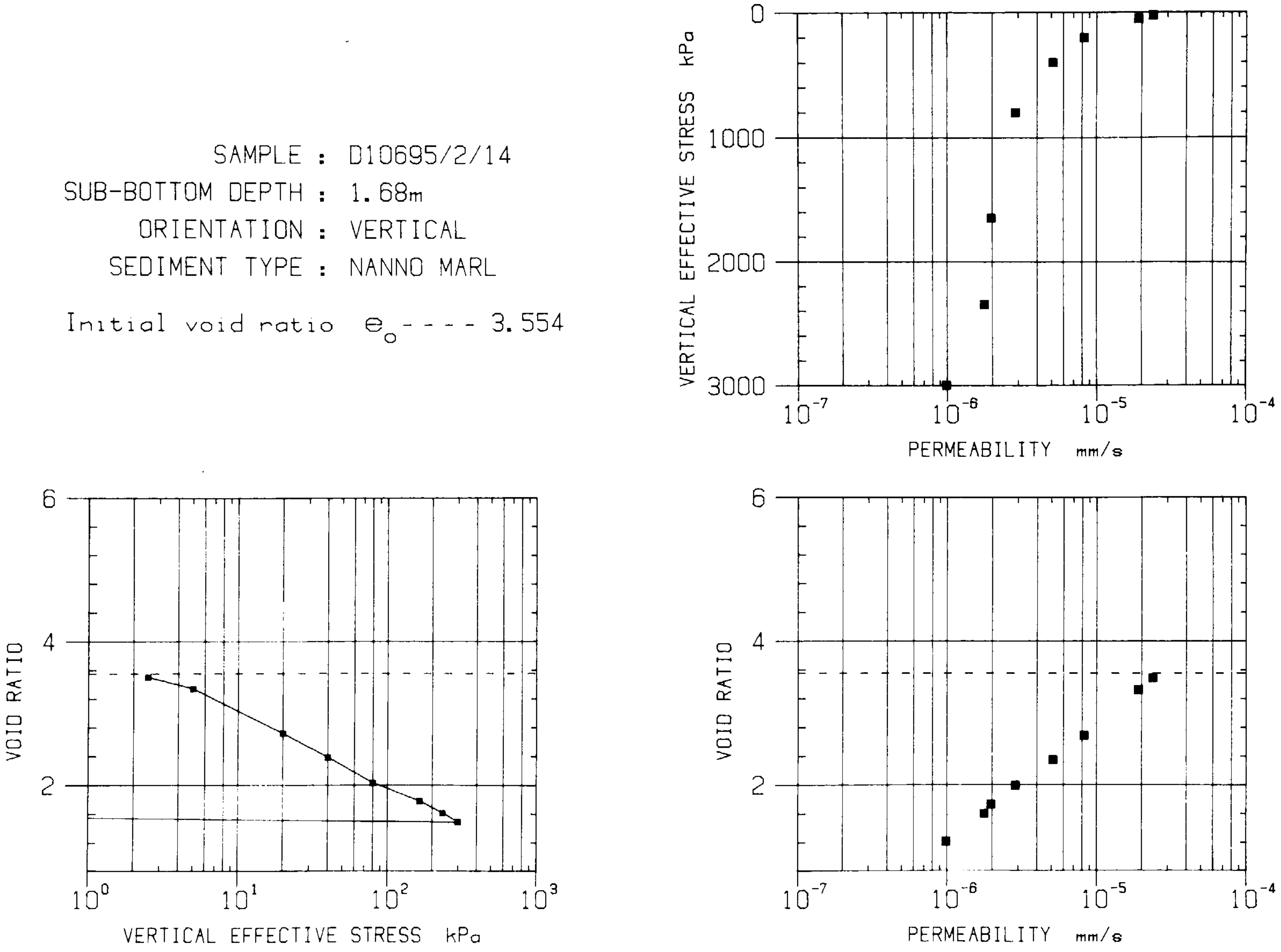

SAMPLE : D10695/2/14
SUB-BOTTOM DEPTH : 1.68m
ORIENTATION : VERTICAL
SEDIMENT TYPE : NANNO MARL

Initial void ratio e_o - - - - 3.554

Figure 5.5 Graphical representation of the results of a typical consolidation/permeability test on nanno marl turbidite B(Sample D10695/2/14).

3.5.3 Fault-like features

The presence of acoustic discontinuities in the area was first noted by Duin & Kuijpers (1983) and subsequently documented by Duin *et al.* (1984). These authors interpreted the features as faults, some with a reverse sense of offset.

The interpretation of the records is not straightforward. Surface-towed seismic profiling equipment uses broad-beam transducer arrays; in the case of 3.5 kHz profiles, the beam is approximately a 90° cone, whereas for airgun or watergun profiling the beam is completely undirectional in the vertical plane normal to the ship's track. This means that reflections can be received from features up to several kilometres away from the nadir, so that point-reflectors are drawn out into long hyperbolae (Hoffman, 1957; Krause, 1962; Smith, 1977; Flood, 1980). Further complications arise from the fact that curved reflectors will tend to focus or defocus energy and this can lead to the spurious impression of a fault plane. Also, it is impossible to resolve curvature on a reflector that has a smaller radius of curvature than the acoustic wavefront and this, for a surface-towed transducer, will be always greater than the water depth. There was therefore a real possibility that the apparent faults in fact arose from relatively gentle synclines or monoclines. Certainly it did not seem possible to be certain of the angle of the fault plane, and therefore that some are reverse faults, on the basis of existing surface-towed records. Finally, the Dutch authors were unable to correlate their faults from track-to-track (with an average track spacing of about 15 km) so the strike was unknown.

Part of *Discovery* cruise 134 was therefore devoted to a closely spaced (approximately one nautical mile) 3.5 kHz profiler survey and a number of deep-towed profiler runs over an area known to show a number of these apparent faults (Figs. 3.11, 3.12). GLORIA sidescan and airgun seismic reflection profiles obtained in this area by *Farnella* were closely re-examined to try to find evidence of these features.

The appearance of the acoustic discontinuities on the 3.5 kHz records from *Discovery* cruise 134 is very striking (Fig. 3.13). The majority of the discontinuities run to within 20 metres of the sediment surface, although some appear to extend higher. Occasionally the first sub-bottom reflector, at a depth of about 6 m, is affected by an apparent offset of 1-2 m or by a sharp change in reflection intensity. There is rarely a topographic expression at the seabed and this is always < 1 m. These shallow effects are therefore very close to the resolution limit of the profiling system. The vertical offset of the sedimentary reflectors increases with depth, and normally extrapolates to zero at the seabed (Duin et al. 1984). Near the discontinuities, reflectors tend to be upbowed with a final downwarp toward the apparent fault on its downthrown side. This 'rollover', or reverse-drag on the downthrow side of the discontinuity is very common, although better developed on some profiles than others (Fig. 3.13). Not all discontinuities are as simple as this; graben-like and other structures have also been observed.

Away from a discontinuity the reflectors return to approximately the same level, which is characteristic of growth faults associated with differential compaction, but not of ordinary normal or reverse faults. Many of the apparent faults are highlighted by a concentration of reflected energy along the plane of the acoustic discontinuity on the side where the rollover is observed, and a lens-shaped area on the other side that shows a drop in reflected energy. These effects can give rise to the appearance of a fault plane, but careful examination of the records convinces us that we cannot determine the dip of any such plane with sufficient precision to say whether the apparent faults are normal or reversed.

Positions of the apparent faults observed during the Discovery 134 survey are shown in Figure 3.12, together with the basement topography from Figure 3.6. Clearly most of the faults are aligned in a NNE-SSW direction, parallel to the dominant basement grain, although details of the basement morphology are not well resolved here.

Figure 3.14 shows the depth below the seabed of an arbitrary reflector from the Discovery cruise 134 3.5 kHz profiles, chosen solely for its easily identifiable character and its occurrence throughout the study area. To some extent the depth of this reflector below the seabed may reflect the detailed morphology of the basement in this area, but it is also clearly affected by the general upbowing and rollover of reflectors near the acoustic discontinuities, and it is difficult to separate these two effects. However, a detailed airgun survey carried out on Discovery cruise 144 while this report was being prepared showed that most of the acoustic discontinuities actually lie over the crests of basement highs.

Re-examination of GLORIA data in this area yielded only one target that coincided with a discontinuity mapped from the Discovery 134 survey. However, the GLORIA target is very small (less than 1 km long) and is right at the limit of resolution of the system. Detailed near-bottom surveys will be needed to check whether this is really the outcrop of a fault on the seafloor.

Some discontinuities can also be seen on the airgun seismic reflection profiles obtained during Farnella cruise 3 (see Section 3.4). On these airgun records it is difficult (especially at depth) to determine if there is any increase in offset with depth. Most of the discontinuities are subvertical, and although one can tell the 'downthrow' side, these features should not be classified as normal or reverse faults as the true angle of the apparent fault planes cannot be resolved.

The geographical distribution of the discontinuities as picked from the Farnella airgun records is shown in Figure 3.11. They are plotted together with the thickness of Unit AB to emphasize the concentration of the features in areas of maximum thickness of this unit. Duin & Kuijpers (1983) and Duin et al. (1984) found a similar relationship. Few fault-like features occur in areas where the unit is less than 300 m thick.

From the evidence it seems clear that the features seen on the records reflect a real change in the attitude of the sediments, and are not artifacts of the acoustic profiling systems. These changes in attitude of the reflectors are concentrated along clearly defined trends, probably governed by some form of structural (basement) control. There are three geological features that would give records such as those examined: small synclines, monoclines, and faults. The general structure of the features, and especially the asymmetrical growth on one side of the discontinuity, suggests that they are not synclines. One of the most diagnostic features is the 'rollover' or reverse-drag which is commonly found in conjunction with growth faults (e.g. Honea, 1956; Hamblin, 1965). The fact that far from the discontinuities the reflectors return to the same level suggests that the discontinuities are not monoclines; also to give the seismic traces seen on the record, monoclines would have to be migrating growth folds, probably turning into growth faults at depth.

It was hoped that the deep-towed profiler runs of Discovery cruise 134 would resolve the ambiguity between monoclines and faults. Three runs were carried out, and it was thought that these included at least one crossing of a discontinuity as mapped from the surface. No offsets of reflectors were seen on the deep-tow record. However, there were residual doubts about the accuracy of the navigation (the deep-towed vehicle was not navigated by acoustic beacons) and the question remained open. During acoustically navigated deep-tow runs on Discovery cruise 144, at least one instance of offset reflectors was seen on the deep-towed record. The shallowest reflector offset was about 17 m below the surface and at 30 m depth the offset was 2 m over a minimum horizontal distance of 18 m. This could still be a monocline at this level, but may develop into a fault at greater depth if the offset increases sufficiently.

TABLE 3.1 - Depths to reflectors and thicknesses of seismic units, in milliseconds of two-way time.

Profile	CD	GH	KL
Depth to R2	120-180 ms	120-190	90-160
Depth to R3	200-280	190-280	120-200
Depth to R4	240-450	280-560	150-440
Maximum depth to basement	700	1300 (1650?)	1400
Thickness of A	120-180	120-190	90-160
Thickness of B	180-310	140-400	40-290
Thickness of AB	240-450	280-560	150-440

FIGURE CAPTIONS

Figure 3.1 Contoured magnetic anomalies reduced to IGRF 1975.0 (IAGA, 1981). Contour interval 100 nT. Ship's tracks shown by broken lines (*Discovery* 118 and 134; *Farnella* 3/81). Heavy lines indicate fracture zones inferred from the basement topography. Circled numbers give magnetic anomaly identifications; bold numbers give interpolated crustal (basement) age in My.

Figure 3.2 Bathymetric chart of GME, in metres corrected for velocity of sound in seawater. Based on soundings collected along tracks of Figure 1.1, with interpolation of contours between tracks guided by GLORIA data (Fig. 3.3).

Figure 3.3 Physiography of GME deduced from GLORIA images. Fine stipple: areas of moderate-to-high GLORIA backscattering, corresponding to basement outcrop or abyssal hills and small seamounts draped by pelagic sediment; broken lines: acoustic lineations reflecting turbidity current pathways; coarse stipple: area of debris flow. Heavy lines outline area insonified by GLORIA. Boxes indicate positions of GLORIA sonographs shown in Figure 3.4.

Figure 3.4 Three individual GLORIA sonographs over parts of GME. For location see Figure 3.3.

Figure 3.5 Total sediment thickness inferred from seismic reflection profiles. IOS data have been combined with the data presented in Enclosure 3 of Duin & Kuijper (1983). Two-way travel-time observations have been converted to depths using the expressions shown: see text for further details. Isopach interval is 250 m, with heavy lines every 1000 m.

Figure 3.6 Total depth to basement inferred from seismic reflection profiles, assuming the same travel-time/depth relation as for Figure 3.5. Contour interval 250 m. IOS data have been combined with data from Enclosure 2 of Duin & Kuijper (1983). Heavy lines show locations of profiles in Figures 3.8 to 3.10.

Figure 3.7 Variation of carbonate compensation depth (CCD) with time in the North Atlantic, after Van Andel (1975) and Tucholke & Vogt (1979). Cross-hatching indicates areas of uncertainty or finite range of CCD. Also shown is the predicted track for 92 My old seafloor, assuming that it was created at the Mid-Atlantic Ridge

	at a depth of 2600 m and subsequently followed the normal age-depth curve of Parsons & Sclater (1977). The effects of a simple two-stage sedimentation model are also shown, though it is emphasised that the actual history may have been more complex (see text).
<u>Figure 3.8</u>	Part of seismic reflection profile CD, with interpretation. See Figure 3.6 for location, and see text for details of interpretation. Recording frequency band was 50 to 150 Hz.
<u>Figure 3.9</u>	Part of seismic reflection profile GH, with interpretation. Arrowheads above section indicate positions of small faults. See Figure 3.6 for location. Recording frequency 50 to 150 Hz.
<u>Figure 3.10</u>	Part of seismic reflection profile KL, with interpretation. Arrowheads above section indicate positions of small faults. See Figure 3.6 for location. Recording frequency 80 to 250 Hz.
<u>Figure 3.11</u>	Plot of acoustic discontinuities (fault-like features) observed by seismic reflection profiling in GME.
<u>Figure 3.12</u>	Location of fault-like features observed in the detailed survey of Discovery cruise 134. Tracks of this survey are shown as light lines. Isopachs to basement are also shown, taken from Figure 3.5. Heavy lines show location of profiles in Figure 3.13.
<u>Figure 3.13</u>	Examples of 3.5 kHz records across apparent faults. Profile locations shown in Figure 3.12.
<u>Figure 3.14</u>	Isopachs (in metres) to a prominent, deep reflector observed on 3.5 kHz records in the 'fault' survey. Locations of apparent faults are also shown.

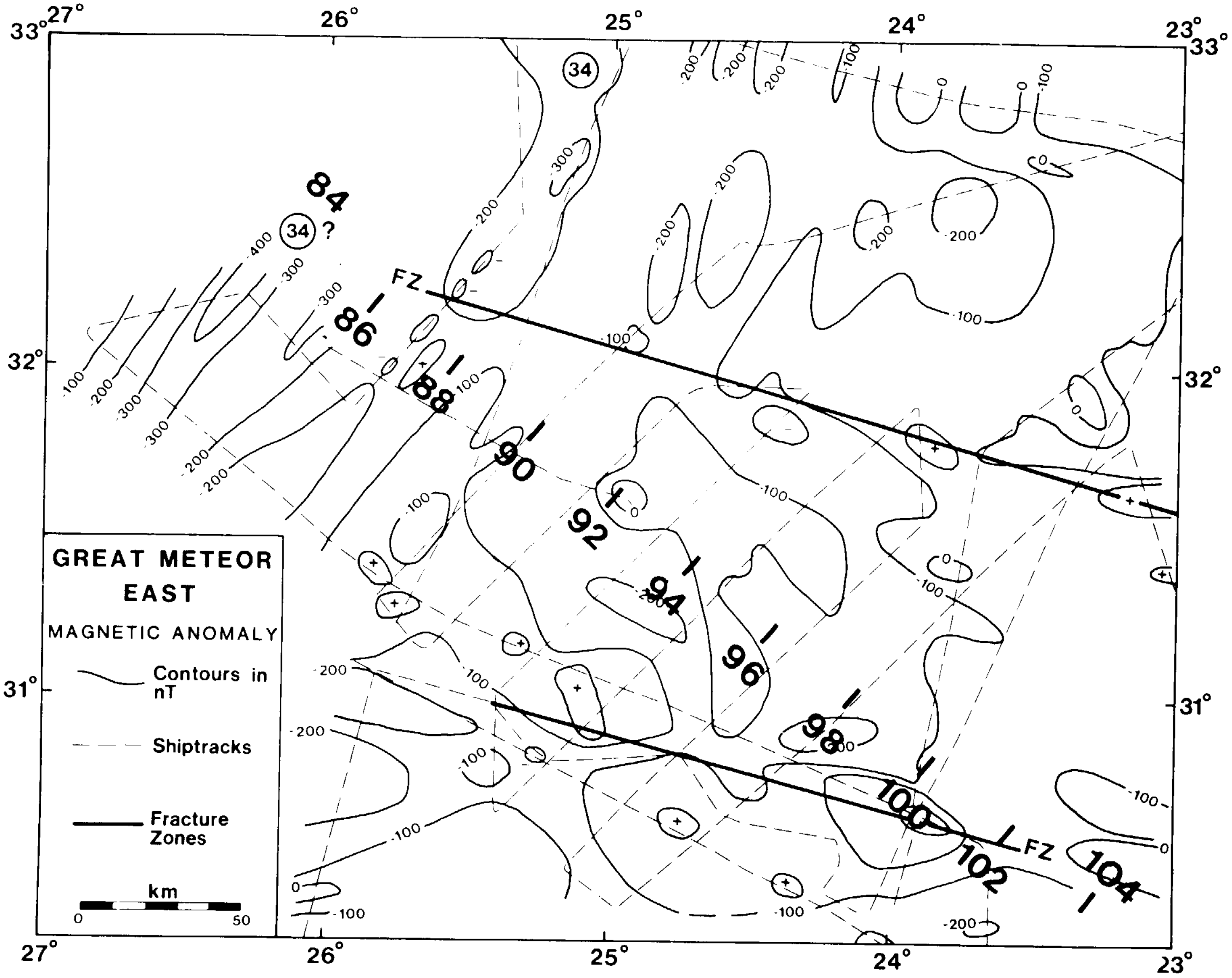

Figure 3.1 Contoured magnetic anomalies reduced to IGRF 1975.0 (IAGA, 1981). Contour interval 100 nT. Ship's tracks shown by broken lines (Discovery 118 and 134; Farnella 3/81). Heavy lines indicate fracture zones inferred from the basement topography. Circled numbers give magnetic anomaly identifications; bold numbers give interpolated crustal (basement) age in My.

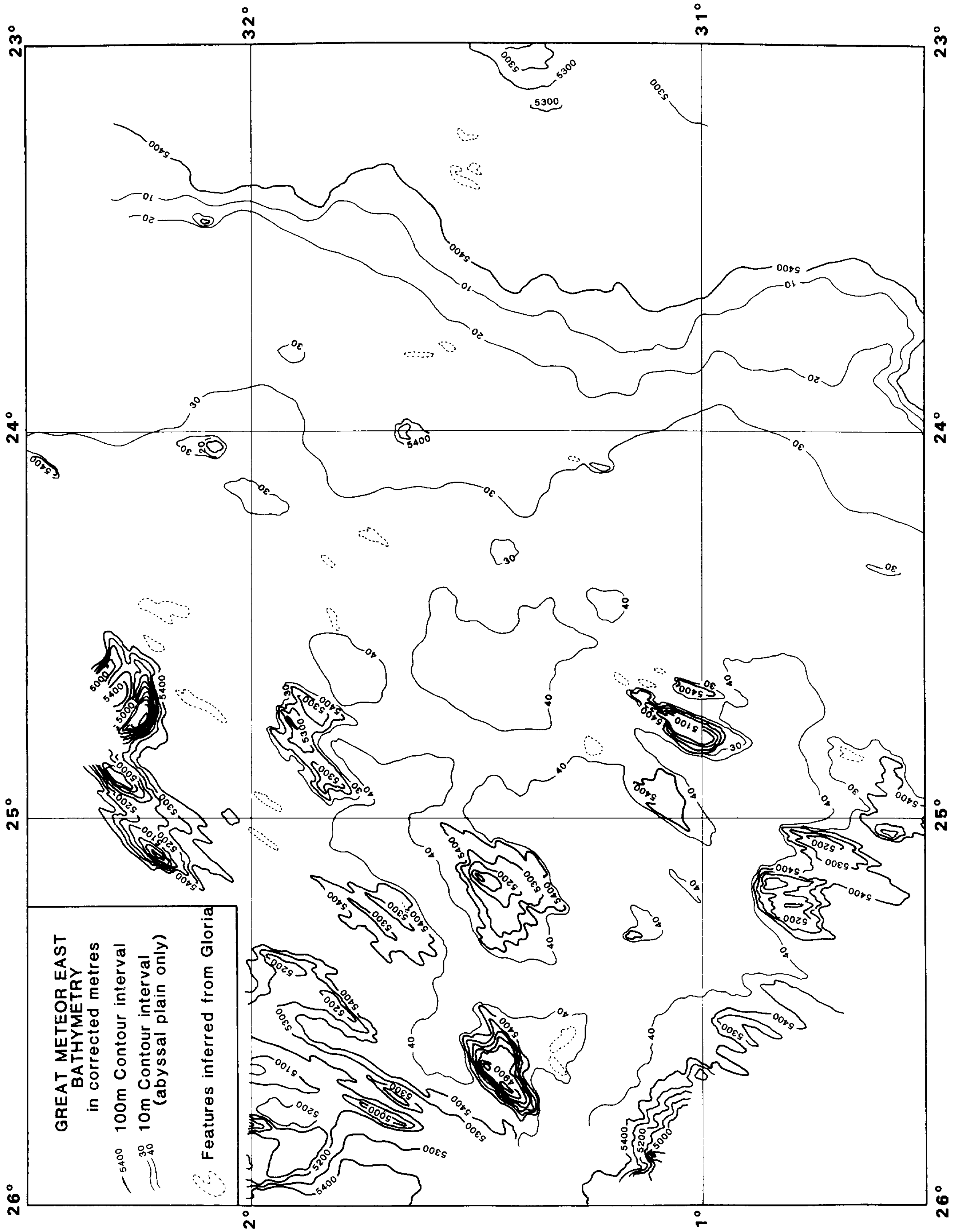

Figure 3.2

Bathymetric chart of GME, in metres corrected for velocity of sound in seawater. Based on soundings collected along tracks of Figure 1.1, with interpolation of contours between tracks guided by GLORIA data (Fig. 3.3).

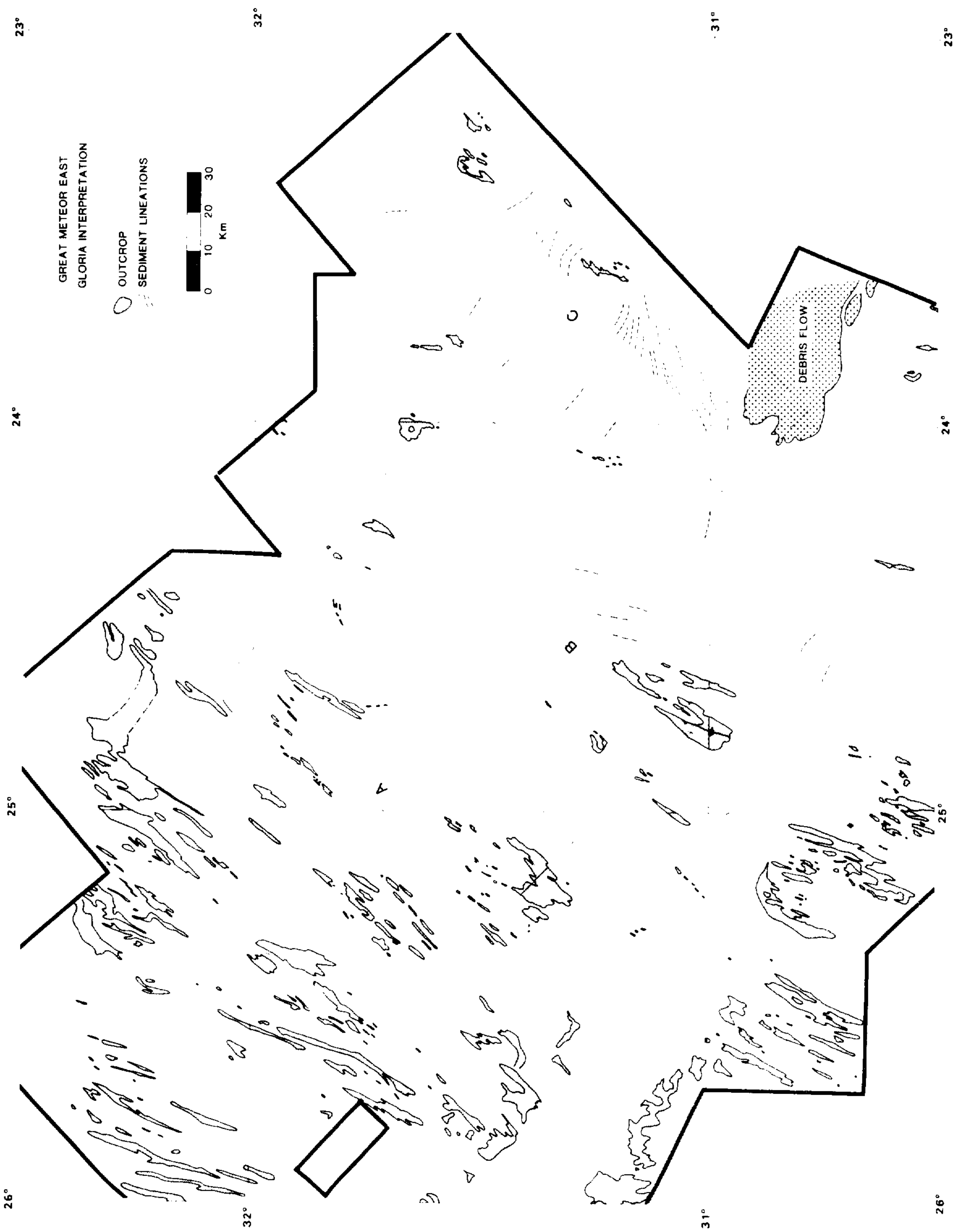

Figure 3.3 Physiography of GME deduced from GLORIA images. Fine stipple: areas of moderate-to-high GLORIA backscattering, corresponding to basement outcrop or abyssal hills and small seamounts draped by pelagic sediment; broken lines: acoustic lineations reflecting turbidity current pathways; coarse stipple: area of debris flow. Heavy lines outline area insonified by GLORIA. Boxes indicate positions of GLORIA sonographs shown in Figure 3.4.

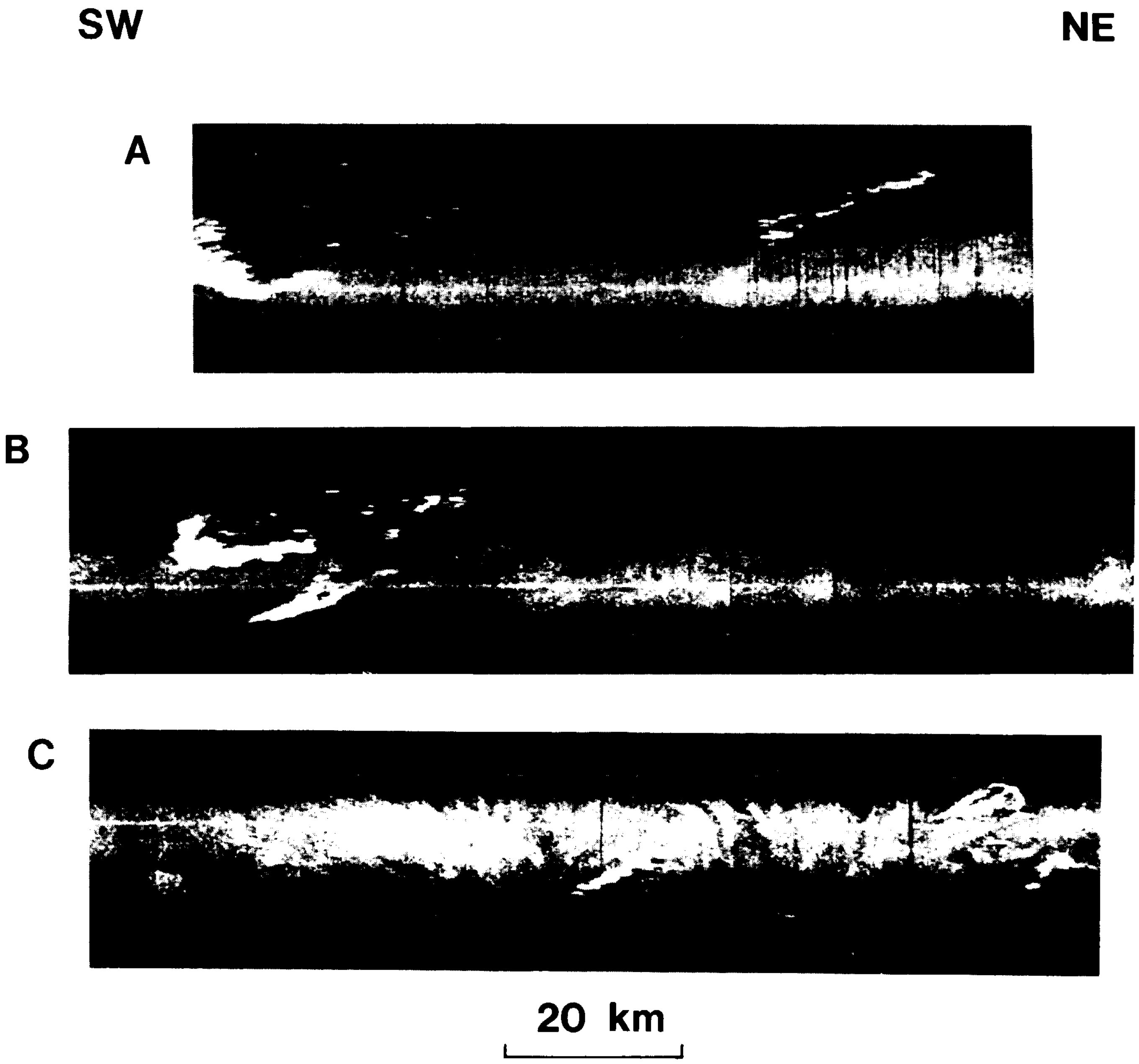

Figure 3.4 Three individual GLORIA sonographs over parts of GME. For location see Figure 3.3.

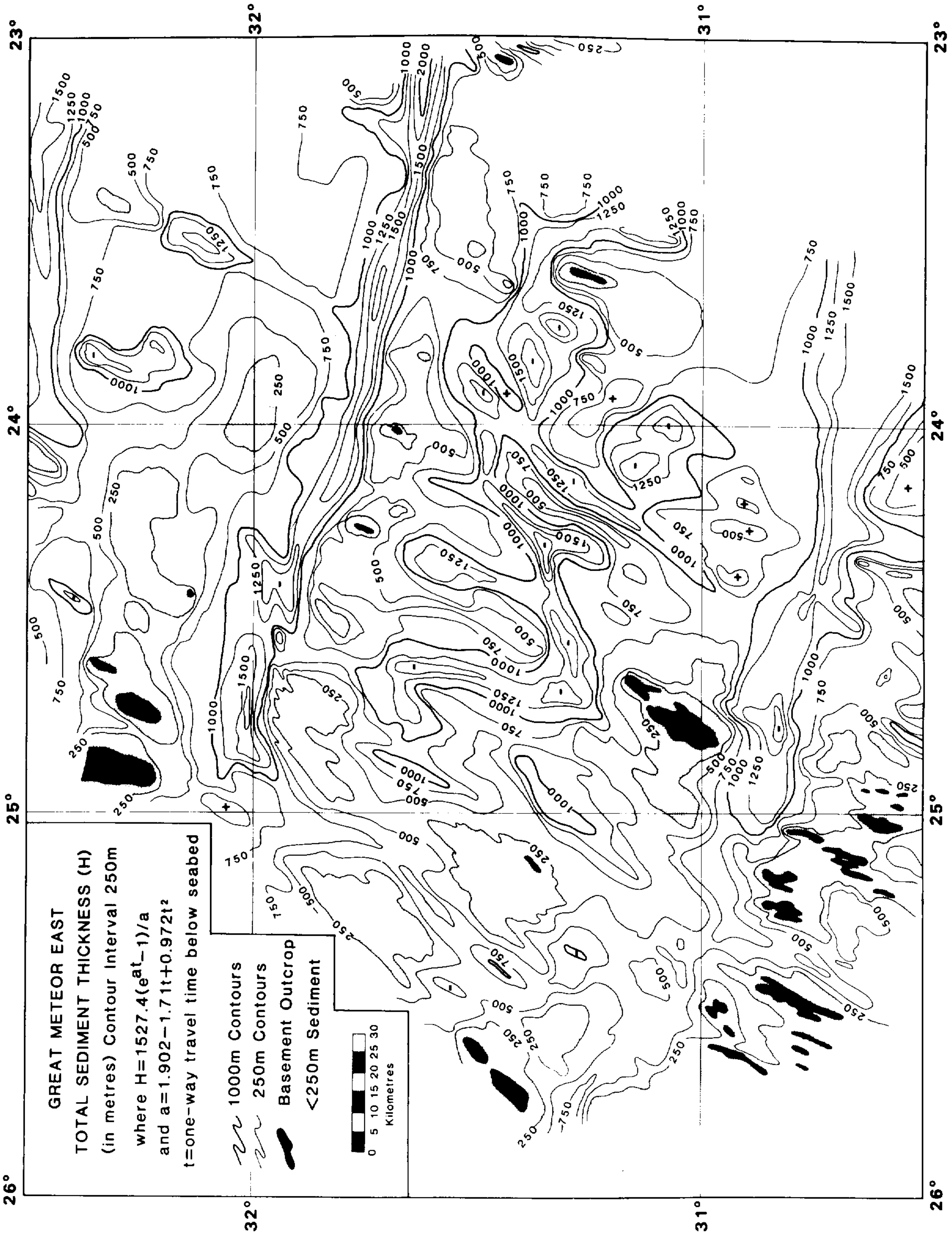

Figure 3.5 Total sediment thickness inferred from seismic reflection profiles. IOS data have been combined with the data presented in Enclosure 3 of Duin & Kuijper (1983). Two-way travel-time observations have been converted to depths using the expressions shown: see text for further details. Isopach interval is 250 m, with heavy lines every 1000 m.

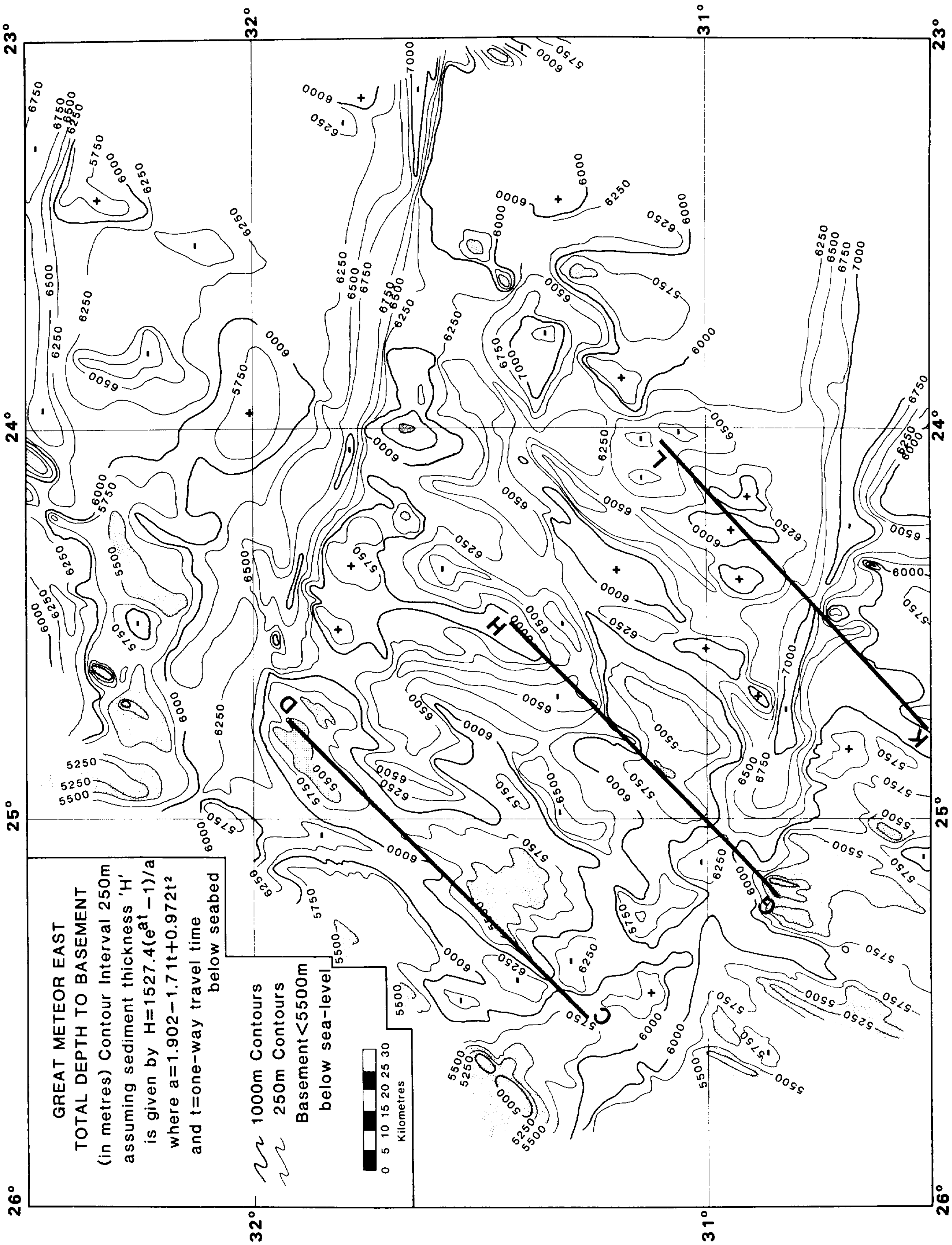

Figure 3.6

Total depth to basement inferred from seismic reflection profiles, assuming the same travel-time/depth relation as for Figure 3.5. Contour interval 250 m. IOS data have been combined with data from Enclosure 2 of Duin & Kuijper (1983). Heavy lines show locations of profiles in Figures 3.8 to 3.10.

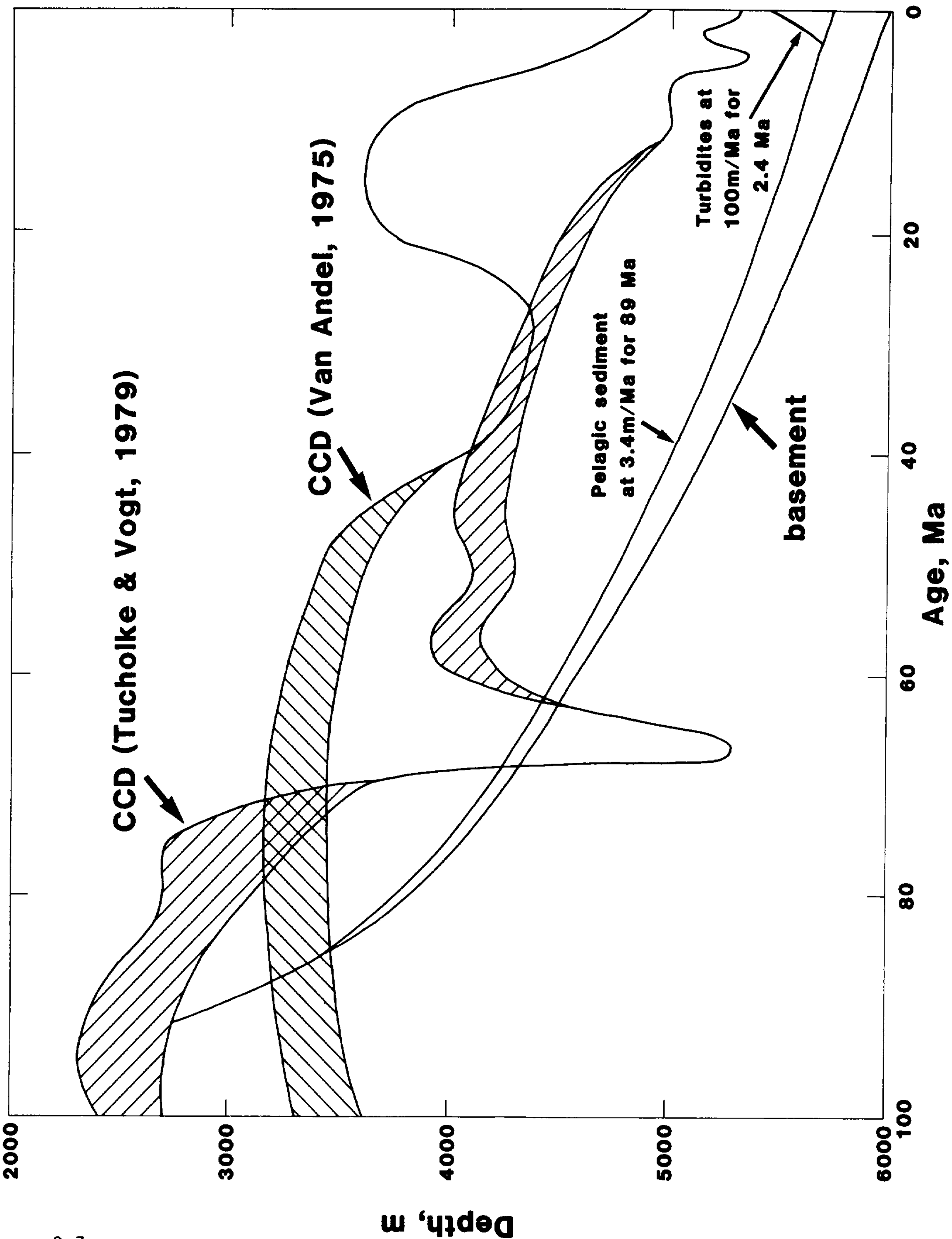

Figure 3.7

Variation of carbonate compensation depth (CCD) with time in the North Atlantic, after Van Andel (1975) and Tucholke & Vogt (1979). Cross-hatching indicates areas of uncertainty or finite range of CCD. Also shown is the predicted track for 92 My old seafloor, assuming that it was created at the Mid-Atlantic Ridge at a depth of 2600 m and subsequently followed the normal age-depth curve of Parsons & Sclater (1977). The effects of a simple two-stage sedimentation model are also shown, though it is emphasised that the actual history may have been more complex (see text).

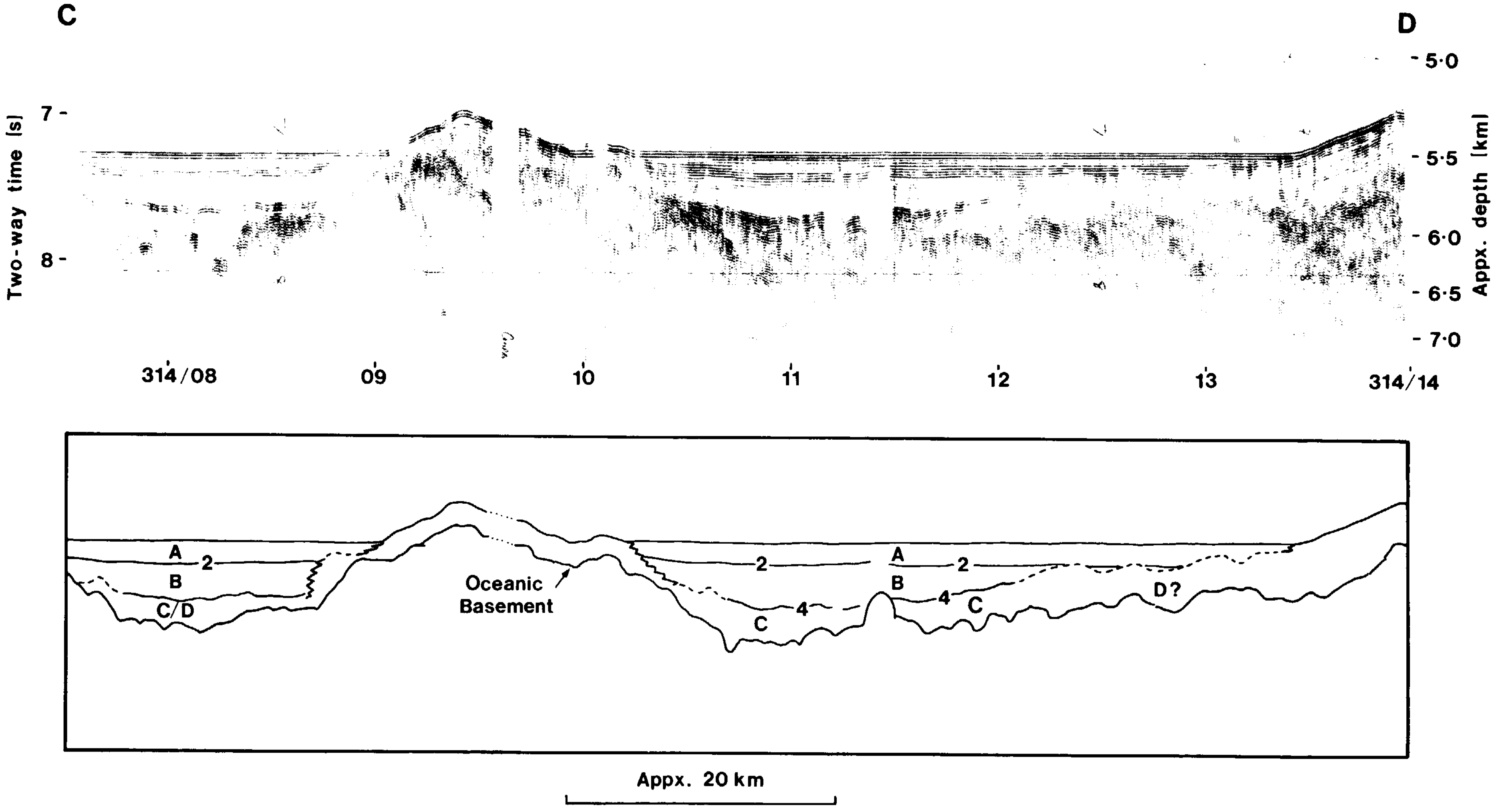

Figure 3.8 Part of seismic reflection profile CD, with interpretation. See Figure 3.6 for location, and see text for details of interpretation. Recording frequency band was 50 to 150 Hz.

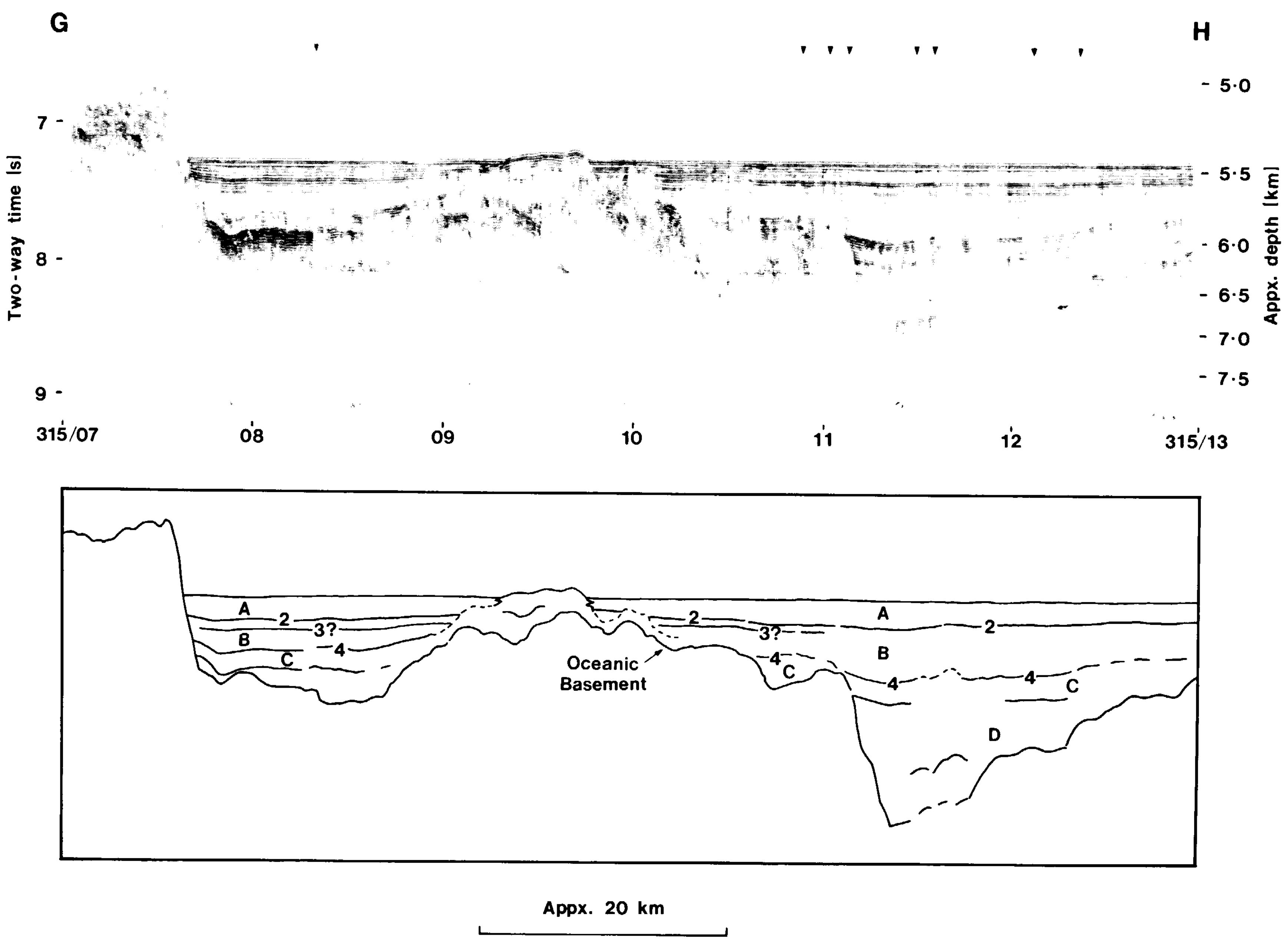

Figure 3.9 Part of seismic reflection profile GH, with interpretation. Arrowheads above section indicate positions of small faults.See Figure 3.6 for location. Recording frequency 50 to 150 Hz.

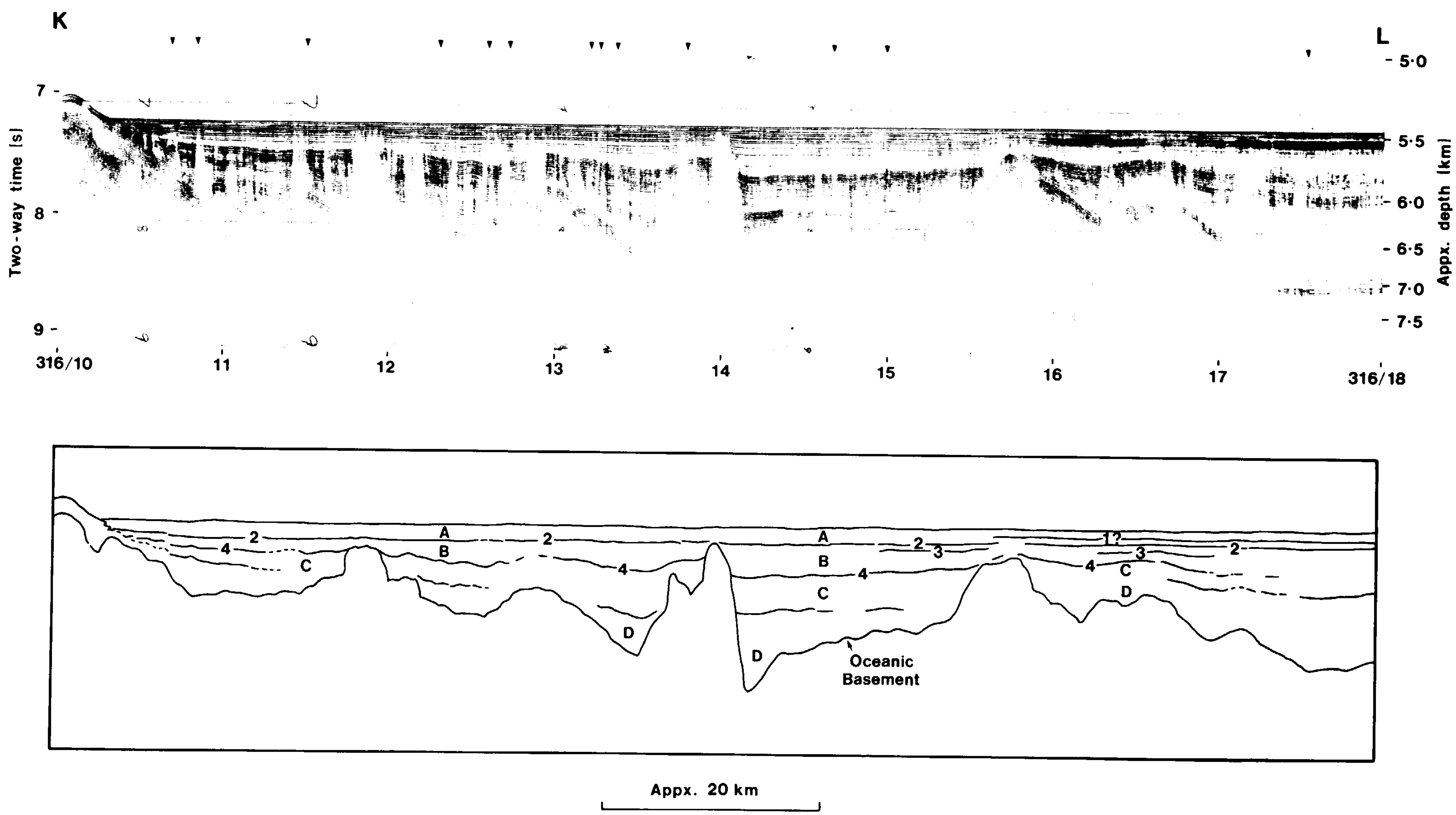

Figure 3.10 Part of seismic reflection profile KL, with interpretation. Arrowheads above section indicate positions of small faults. See Figure 3.6 for location. Recording frequency 80 to 250 Hz.

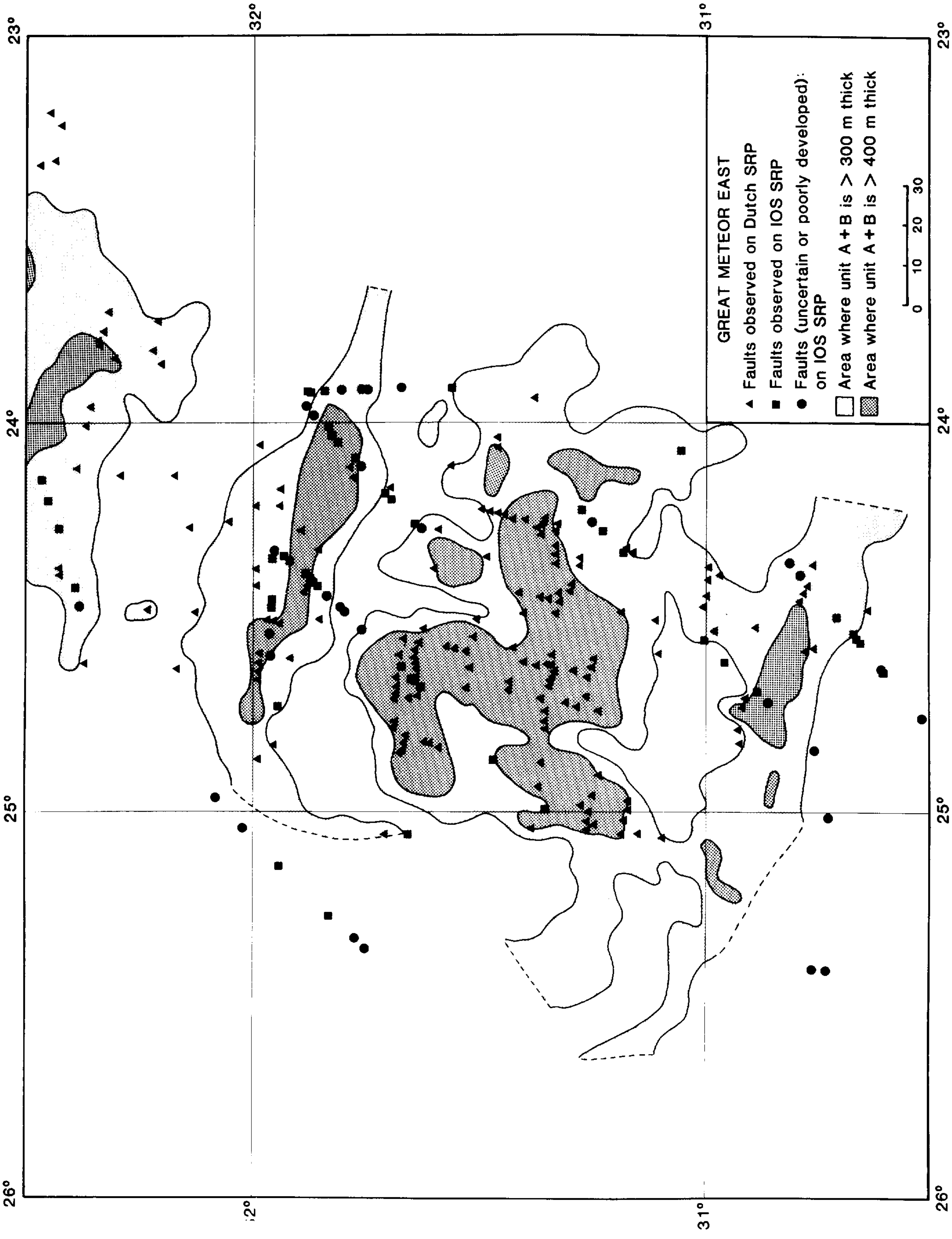

Figure 3.11

Plot of acoustic discontinuities (fault-like features) observed by seismic reflection profiling in GME.

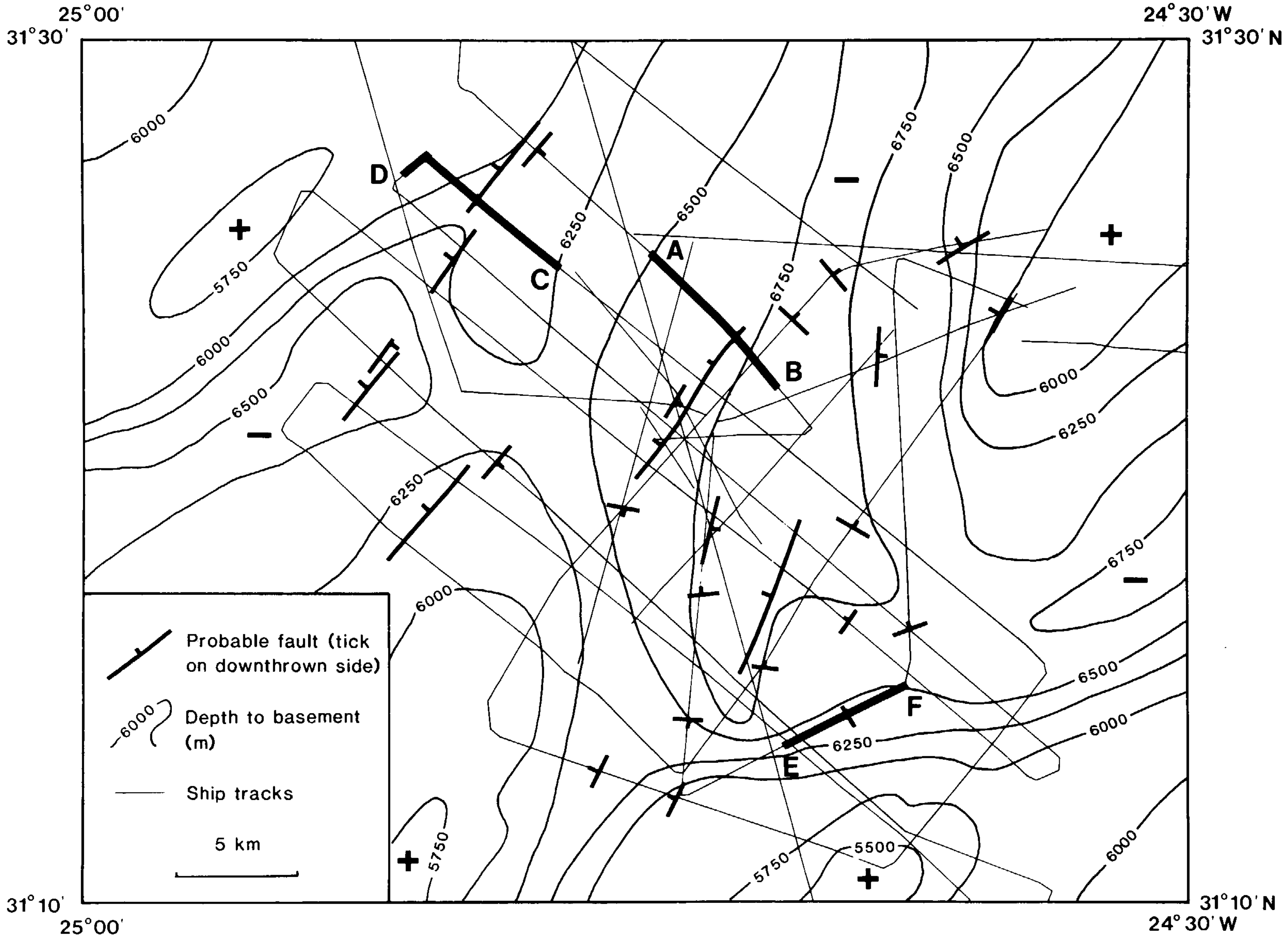

Figure 3.12 Location of fault-like features observed in the detailed survey of *Discovery* cruise 134. Tracks of this survey are shown as light lines. Isopachs to basement are also shown, taken from Figure 3.5. Heavy lines show location of profiles in Figure 3.13.

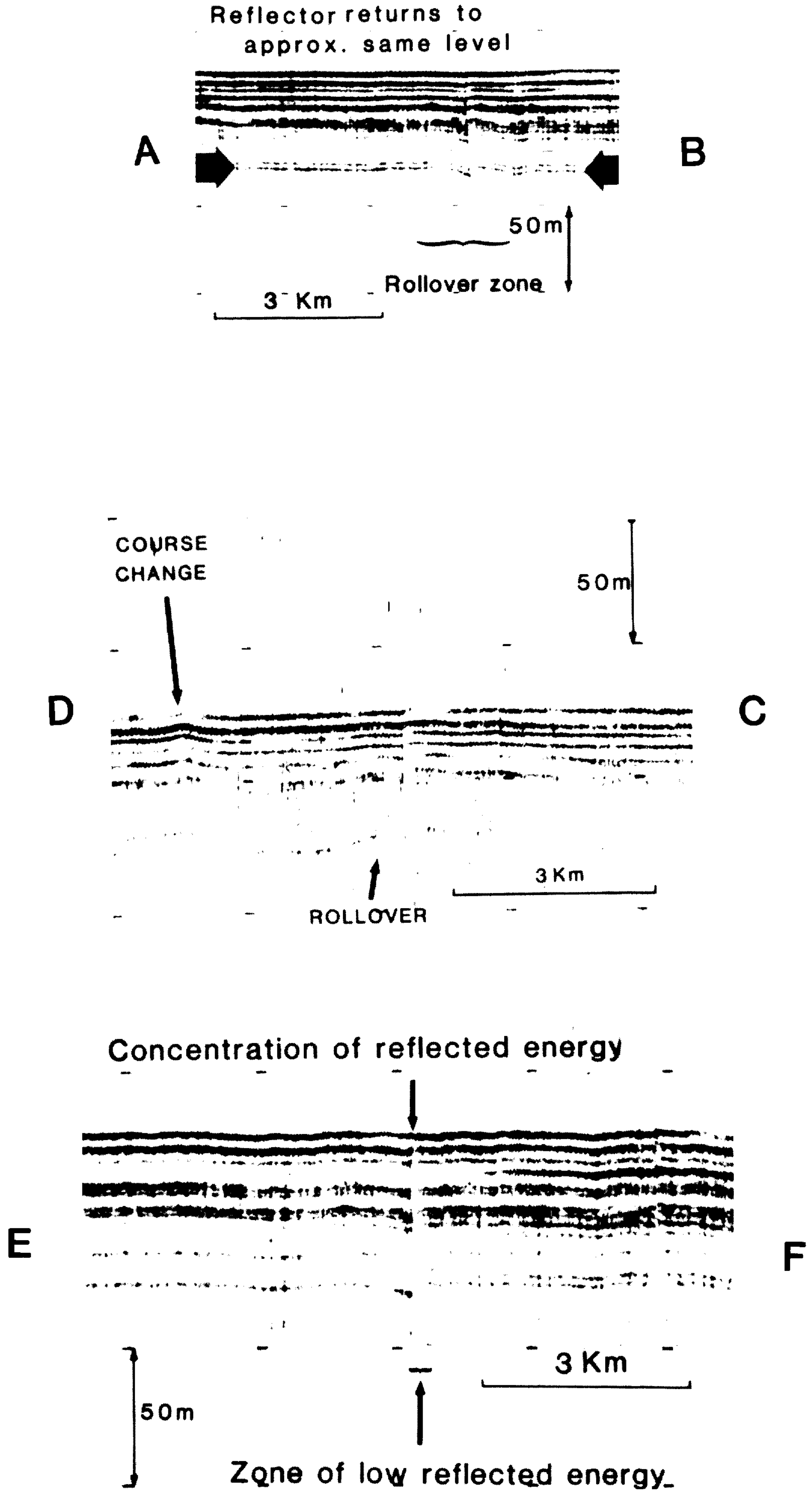

Figure 3.13 Examples of 3.5 kHz records across apparent faults. Profile locations shown in Figure 3.12.

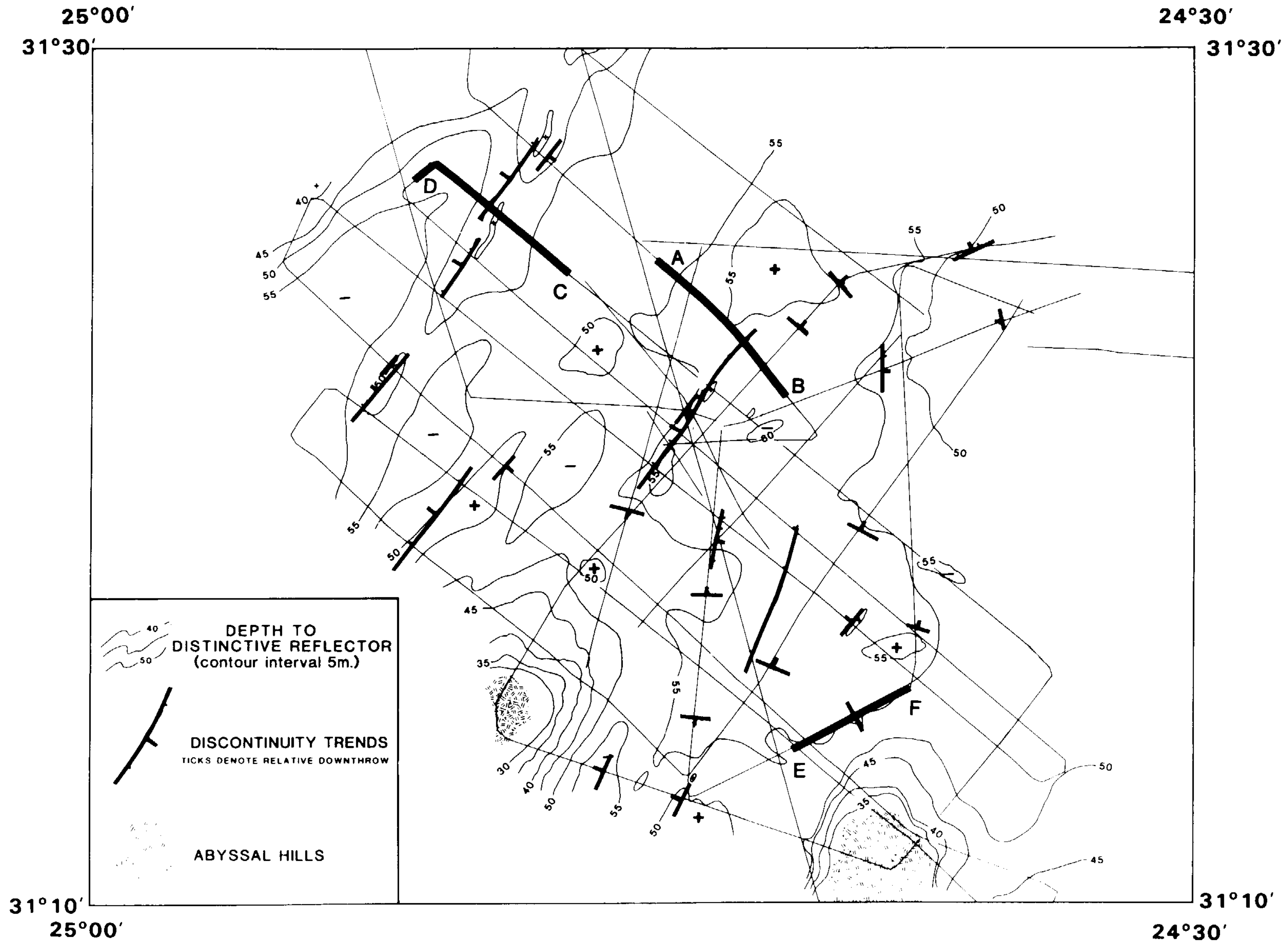

Figure 3.14 Isopachs (in metres) to a prominent, deep reflector observed on 3.5 kHz records in the 'fault' survey. Locations of apparent faults are also shown.

4. SEDIMENTOLOGY AND STRATIGRAPHY

Surficial sediments in the GME area fall into two basic types - those derived from turbidity current transport (turbidites) and those derived from surface water productivity in the area (pelagic sediments). These two types alternate, generally with thick turbidite units separated by thin layers of pelagic sediment. Studies have been carried out to date on four IOS piston cores and six IOS gravity cores, but stratigraphic analyses have also been completed on four Dutch piston cores in conjunction with the Rijks Geologische Dienst (RGD), Haarlem (Table 4.1; Fig. 1.2; Weaver & Kuijpers, 1983). Interpretation of sediment distribution between cores is derived mainly from 3.5 kHz records. Because turbidites are transported sediments, many factors can affect their eventual composition and it is stressed that the parameters described here refer only to those turbidites studied. Deeper turbidites may have quite different compositions and the presence of thick sandy layers at depth cannot be ruled out.

4.1 Pelagic Sediments

The area today lies in the lysocline but above the CCD (Thunell, 1982). Thus, a proportion of the calcium carbonate reaching the seafloor is dissolved before burial and the resulting sediment appears relatively enriched in non-carbonate components. The amount of dissolution depends on the corrosiveness of the bottom water and this is greatly increased during glacial periods (Crowley, 1983). During the severest glacial periods, in the GME area dissolution exceeds supply of calcium carbonate and the resulting sediment is pelagic clay. Less severe glacials and interglacials produce marly clays, marls or marly oozes. Because the clays have resulted from removal of material they usually form thinner layers than the marls.

Three cores consisting predominantly of pelagic sediment (D10320, D10323 and 82PCS17; Fig. 4.1) have been taken in the area. These cores show the history of pelagic deposition, generally unaffected by turbidity currents (Weaver & Kuijpers, 1983). Cores D10323 and 82PCS17 were located to the south in a slightly shallower region while core D10320 was located to the west in the low abyssal hills. All three show alternations of more marly and less marly units. Core D10320 has the shallowest location and contains marls and marly oozes with rare pelagic clay layers. Cores D10323 and the upper part of 82PCS17 show alternations of marl and pelagic clay, while the lower part of 82PCS17 shows alternations of calcareous oozes, marls and pelagic clays. Typically, marl units vary from 10-30 cm thick, pelagic clays from 6-10 cm and oozes from 7-60 cm. Some unaccountably thick pelagic clay units are found in 82PCS17.

The carbonate fraction of the cores consists exclusively of coccoliths and planktonic foraminifera. The latter are often corroded and broken in the marls, while both are absent from the pelagic clays.

Median grain sizes of the pelagic units range between $Md\phi$ 7.6 and $Md\phi > 8$, or from fine silt to clay (Fig. 4.2). No grain size analyses have been carried out on the clay fraction to date.

4.2 Turbidites

Turbidites comprise most of the sediment recovered from the area. Turbidites are sediments deposited from turbidity currents which are capable of transporting sediment over more than a thousand kilometres. Such currents will continue to flow downslope until their sediment load is depleted by deposition en route or, if their load is sufficiently large, they will continue to the base of the slope. The GME site lies at the base of the continental rise and turbidites have become ponded between the base of the rise to the east and the hills of the mid-Atlantic Ridge to the west.

The turbidites all belong to the E division of Piper (1978). They consist of ungraded massive silts (E3 division), in some cases with graded laminated basal layers (E1 and E2 divisions; Fig. 4.3, plate 1). Grain sizes in the silty bases vary across the area and from turbidite to turbidite. Out of cores D10688 and D10695, the coarsest sample we have measured is the base of turbidite B in core D10695. This has a median grain size of $Md\phi$ 4.6 (coarse silt). The ungraded parts of all turbidites have a median grain size in the clay range ($Md\phi > 8$). No subdivision of grain sizes in this range has been carried out to date. The basal layers contain an assemblage of particles including basalt fragments, glass shards, micas, heavy minerals and foraminifera. The massive silts consist of about 50-60% calcium carbonate, predominantly coccoliths, with clay minerals (illite and montmorillonite). The oldest turbidites recorded consist of over 70% calcium carbonate which may reflect a different source area (Fig. 4.4).

Many, but not all, of the turbidites consist of a couplet of two distinctly coloured units - a lower deep olive green unit and an upper pale green or grey unit. Mineralogically there is no difference between these two but chemically the dark green unit contains 1-2% of organic carbon as opposed to the pale units which contain less than 0.5% organic carbon. A series of bluish laminae around the colour change suggest the presence of chemical fronts; this will be discussed further in Chapter 6.

4.3 Stratigraphy

Cores D10320, D10323 and 82PCS17, which consist predominantly of pelagic sediment, provide good reference sections for a combined bio-lithostratigraphy. This stratigraphy can be compared directly to oxygen isotope stages (Emiliani, 1955; Shackleton & Opdyke, 1973),since the degree of dissolution of the sediments varies according to the corrosiveness of bottom water which is directly linked to ice production (Crowley, 1983). The alternating lithologies, therefore, represent alternating glacial/interglacial conditions with the more carbonate-rich units reflecting interglacial conditions. Used in isolation, this stratigraphy could not identify missing units, but when it is used in conjunction with the coccolith stratigraphy, particular glacial and interglacial stages can be identified. The main elements of the coccolith stratigraphy are: dominance of Emiliania huxleyi since late oxygen isotope stage 5 (Thierstein et al., 1977), dominance of Gephyrocapsa aperta in oxygen isotope stage 7 (Weaver, 1983), dominance of Gephyrocapsa caribbeanica below oxygen isotope stage 7 (Kidd et al., 1983a), and the extinction of Pseudoemiliania lacunosa in oxygen isotope stage 12 (Thierstein et al., 1977). This stratigraphy can be clearly seen in cores 82PCS17 and D10320 (Figure 4.5).

Core 82PCS17 extends considerably further back in time, with the extinction point of Calcidiscus macintyrei recognisable at 690 cm giving an age of 1.45 My for this level (Fig. 4.1). No discoasters were found in this core, however, and so its base must be younger than 1.88 My (Backman & Shackleton, 1983). The estimated age for the base of this core is 1.67 My, based on extrapolation of the average sedimentation rate between the extinction point of P. lacunosa (450,000 years) at about 200 cm and the extinction of C. macintyrei at 690 cm. The average sedimentation rate for this interval is 0.49 cm/1000 years. Thus the pattern of pelagic sedimentation with alternating thin bands of ooze, marl and pelagic clay is continued to at least 1.67 My.

To compare the rate of deposition of pelagic sediment in the turbidite cores to that in the non-turbidite cores, the pelagic intervals in cores 82PCS13, 82PCS20 and 82PCS34 have been plotted in Figure 4.5 without the intervening turbidites. Cores 82PCS13 and 82PCS20 show complete suites of oxygen isotope stages back to stages 6 and 7 respectively, while core 82PCS34 shows a record to beyond stage 11 with oxygen isotope stages 2 and 8 missing. The reasons for these two missing glacial intervals are uncertain but, by comparison to cores D10320 and D10323, both would be very thin and they may have been removed by locally increased current activity around an adjacent hill. Increased current strengths have been recorded around small abyssal hills and such currents may have been stronger during glacial intervals (Gould et al., 1981). Comparisons of pelagic sediment deposition in cores 82PCS13 and 82PCS20 with D10323 (taken at approximately the same water depth) in Figure 4.5 show slightly higher sedimentation rates in the turbidite cores than in purely pelagic cores, but this may be due to bioturbation of turbidite material up into the pelagic units. Certainly, there is almost no evidence of erosion of the pelagic intervals in these two cores by incoming turbidity currents (Weaver & Kuijpers, 1983). Core 82PCS34 shows slightly slower deposition rates than the other cores and lacks oxygen isotope stages 2 and 8.

If we now consider the cores complete with their turbidites, the correlations of the pelagic units give a framework within which the turbidites must correlate (Figs. 4.6, 4.7 and 4.8). The turbidites are lettered consecutively from the top, with thin turbidites which cannot be traced across the whole area given numbered suffixes. The coccolith floras of the turbidites themselves, although containing both young and old elements due to mixing during the turbidity flow, correlate well between cores. Certain turbidites can be identified by high or low percentages of particular coccolith species e.g. turbidite E in Figures 4.6 and 4.7 contains a high proportion of G. aperta whereas turbidite D contains a high proportion of Gephyrocapsa muellerae. Other features of each turbidite, such as relative thickness, presence of a silty base, calcium carbonate content or even colour also serve to distinguish some turbidites. The B, E, and F turbidites are always the thickest and the G turbidite is always a buff colour throughout. The A1 turbidite is generally deep green in colour with a calcium carbonate content around 30% - in most of the other turbidites the calcium carbonate content averages 50-60% but in the J, L and M turbidites it is around 80%. Enough criteria exist, therefore, to identify each turbidite in all of the cores, and with the 3.5 kHz coverage we can correlate individual turbidites across the whole area. Table 4.2 summarises the lithological units of both pelagic and turbiditic origin.

4.4 Lateral distribution of sediments

The pelagic units can generally be found throughout the study area. Exceptions occur in core 82PCS34 from north of 32°30'N. In this core, oxygen isotope stage 2 is absent and below stage 7 the stratigraphy is not readily comparable to the other cores (Fig. 4.6). At present, we believe this may be due to local conditions at this core site, i.e. the hill which lies very close to the south.

The turbidites are also laterally continuous although variations occur in their individual thicknesses and particularly in the thickness of any coarse basal layers they may possess. IOS core coverage is currently insufficient to enable us to contour isopach maps for individual turbidites. One such contour map for the coarse silt at the base of turbidite B has been produced by Duin & Kuijpers (1983) and this shows a strong eastward thickening of this layer, from less than 0.1m west of 25°W, to over 1.0m east of 24°W. Such variations reflect the transport pathway of the turbidity current since coarser grains will be deposited first, as the flow decelerates. Turbidite E has a very restricted basal coarse layer, but the thickness of the whole turbidite increases from less than 0.5m, east of 23°30'W, to over 4m west of 25°20'W (A. Kuijpers, pers. comm.). We intend to examine variation in thickness of turbidite units in more detail in the near future when more cores become available from further IOS and Dutch investigations. For the purposes of this report we have included maximum and minimum measured thicknesses of each turbidite in Table 4.2.

Turbidites which do not cover the whole area are given numbered suffixes in the figures. These turbidites do not form a significant proportion of the sediments, even where they do occur, and none of them has a coarse base. The A turbidite has not been found in all cores but this is most probably due to coring difficulties. This turbidite is very soupy and it may be difficult for such a sediment to open the core catcher. Duin & Kuijpers (1983) suggest this turbidite can only properly be cored with wider diameter piston corers. However, it was not present in IOS box core No. D10554-5 (T.R.S. Wilson, personal communication), so it is possible that its distribution is irregular or patchy. Other coring difficulties are responsible for several metres of sediment being missing from the top of core D10699 and a few metres being missing from the top of core D10698 (Fig. 4.7).

4.5 Sedimentation Rates

Sedimentation in the area is cyclical, with the pelagic units being deposited very slowly and the turbidites rapidly. The rates for the pelagic units vary from about 0.6 cm/1000 years for the marls, to about 0.25 cm/1000 years for the pelagic clays. The rate of deposition of a single turbidite is not known but it is likely that such a unit would be deposited in less than one year (Bowen et al., 1984). The mean sedimentation rate over the last 190,000 years (base of isotope stage 6), taking into account both turbidites and pelagic units, varies from 4.6 cm/1000 years for core D10688 to 10.5 cm/1000 years for core 82PCS13.

4.6 Origin and Frequency of Turbidity Currents

One of the interesting results to emerge from the stratigraphic analysis is the timing of the turbidity currents (Weaver & Kuijpers, 1983). The pelagic lithologies in the cores are almost invariably different at the top and base of each turbidite e.g. turbidite D has marl above and pelagic clay beneath, while turbidite E has clay above and marl beneath. Since we have evidence that the turbidity currents cause no significant erosion of the pelagic sediments in the area where the cores were collected, the turbidites must be deposited during the transition from one sediment type to another. These transitions reflect global climate changes between glacial and interglacial conditions (Crowley, 1983; Gardner, 1975) and, thus, major turbidite deposition in this area is associated with climate change.

The most likely association is via eustatic sea-level changes. Correlation between the rate and relative amount of sea-level rise and fall with oxygen isotope stage boundaries (Cronin, 1983) show that the most major changes occur at the boundaries between oxygen isotope stages 5/6, 4/5 and 1/2. These boundaries coincide with the three largest turbidites in the cores (F, E and B, respectively). Less severe sea-level changes occur at the stage 3/4 and 2/3 boundaries (Cronin, 1983) and, in these cases, a turbidite is associated with the 3/4 stage boundary (turbidite D) but not with the 2/3 stage boundary. The more minor sea-level changes within stage 5 (Cronin, 1983) are associated with the oxygen isotope subdivisions of this stage (Shackleton, 1969). A minor turbidite occurs within stage 5 in cores from the west and central parts of the area (Figs. 4.6 and 4.7). Cores 82PCS20, D10688 and D10699 received no mid-stage 5 turbidite but all received a mid-stage 7 turbidite. Cronin did not consider sea-level changes earlier than stage 6 but a short-lived period of rapid ice growth has been postulated during stage 7 (Ruddiman & McIntyre, 1981) which would be associated with sea-level fluctuations. Thus, there may be some relationship between magnitude of sea-level change and the volume of material moved in a single mass-flow event. Below stage 7 the turbidites are much thinner (Figs. 4.6 and 4.7) and turbidites J, L and M contain much more calcium carbonate. A different source area could produce this change but why the source area should change is uncertain.

We believe the turbidites originate on the upper continental slope off NW Africa or possibly from the Madeira Rise. Some of the turbidites contain relatively high organic carbon contents (over 1%) which suggests initial deposition in areas of relatively high productivity such as the shelf or upper continental slope. The silty bases of the turbidites also contain benthonic foraminifera such as Brizalina spathulata, B. pseudopunctata and Gavelinopsis praegeri, which are typical of the continental shelf/upper slope environment, together with deep-sea species (J. Weston, pers. comm.).

A series of submarine slides and debris flows have been mapped along the NW African continental margin (Embley & Jacobi, 1977; Embley, 1982). These are all of considerable magnitude and could be responsible for initiating some of the turbidity currents discussed here. The Saharan slide has been dated as 15,000 to 16,000 BP (Embley, 1982) which corresponds with the initial rapid early deglaciation at the end of oxygen isotope stage 2, dated as 16,000 to 13,000 BP (Ruddiman & McIntyre, 1981). The large-scale sediment mass movements on the upper continental slope off NW Africa thus seem to be triggered during major sea-level rises and falls and probably do not operate at random as previously reported (Embley, 1982).

Eustacy has been proposed as a controlling mechanism for turbidity current initiation (Embley, 1980; Sarnthein, 1978) but only in that such currents would be preferentially produced during low stands of sea-level. However, our work suggests that, at least in the Upper Quaternary succession of the Madeira Abyssal Plain, major turbidity currents were initiated only during transgressions and regressions and not during the quiet intervals between. An apparent link exists between the magnitude of eustatic sea-level change and the volume of material associated with a single sediment instability on the NW African continental slope.

4.7 Bioturbation

Bioturbation can be seen in the form of open and filled burrows. The filled burrows occur mainly in the pelagic sediments but they do penetrate into the upper parts of the turbidites. The most common burrows are of Planolites, Chondrites and, more rarely, Zoophycos . Turbidites are deposited very rapidly (probably in 1-2 months) and so the maximum vertical penetration of burrows into the top of a turbidite indicates the maximum extent of bioturbation. In the present cores this varies from a few centimetres to a maximum of about 40 cm for the filled burrows, although the burrowing is generally concentrated at the top of each turbidite.

Open (i.e. water-filled) burrows are also common in the GME sediments. These fall into two types - large and small diameter. Their distribution and effect on the physical properties of the sediment has been described by Weaver & Schultheiss (1983) but a brief account is also included here.

The large open burrows are about 5 mm in diameter and of unknown length (Fig. 4.9). They have been found on several occasions in Kastenlot gravity cores while occasional soupy burrow infills in piston cores suggest that they may be partially destroyed by piston coring. Their distribution in the sediment is, therefore, unknown, as is the maximum depth to which they can be found. Similar open burrows have been reported to sub-bottom depths of 64 metres in the eastern equatorial Pacific (Prell, Gardner *et al*., 1982, p. 168). It is unlikely that such burrows form a continuous interconnecting network through the sediment but they may enable rapid transport of radionuclides to take place across short intervals within the sediment column.

The second type of open burrow is much narrower - up to 1.2 mm, but commonly less than 0.5 mm in diameter. These probably belong to the genus *Trichichnus* being long, thin and numerous with up to 50 per 100 cm^2. They have only been found in Kastenlot cores and we believe that they would be closed, and thus obliterated, by the action of coring in piston cores. Since maximum core lengths so far recovered with the Kastenlot corer are about 4m, we have only been able to observe these burrows in the upper part of the sediment column, i.e. the upper part of the B turbidite. Kasten cores have so far not penetrated further than the base of this turbidite.

The *Trichichnus* burrows seem to be restricted to the turbidites, where they occur in the upper pale-coloured (originally oxidised) unit. This may be due to the organism's preference for oxidising conditions or the presence of numerous open burrows could provide the supply of oxygen necessary to oxidise previously reduced sediment. Calculations based on the size of burrow and their density suggest that they have a profound effect on the sediment permeability. It can be shown that, for a mass of sediment containing smooth open parallel tubes (assuming Darcian and Poiseuille flow in the sediment and tubes respectively), the permeability (strictly the hydraulic conductivity) in the direction of the tubes k ($mm\ s^{-1}$) is given by:

$$k = 10\ \{k_s\ (1 - n\pi r^2) + n\pi r^4 \rho g / 8\mu\} \qquad (4.1)$$

where k_s is the permeability of the unburrowed sediment (mm s^{-1}), n is the number of tubes per square centimetre, r is the radius of the tubes (cm), ρ is the density (g cm^{-3}), g is the acceleration due to gravity (cm s^{-2}) and μ is the viscosity (Poise). Figure 4.10 illustrates the influence of open burrows on the permeability of deep sea clays using the above equation for a range of values of r and n. k_s becomes negligible in the above equation when the values fall below 10^{-4} mm s^{-1}. Most deep-sea sediments have permeabilities ranging between 10^{-4} and 10^{-6} mm s^{-1}, so the increase by two orders of magnitude produced by the open burrows (where n = 0.5 and r = 0.2 mm) becomes most significant.

Laboratory measurements on these cores give k_s values around 10^{-5} mm s^{-1} for the interval below the open burrows. In the burrowed interval, however, values of 10^{-4} mm s^{-1} were recorded. The reason for values much lower than those predicted in Figure 4.10 may be two-fold. Permeability measurements at low effective stresses are often inaccurate due to sample sealing problems; and such delicate burrows may close, at least partially, during sampling.

So far our studies of open burrows relate only to the B turbidite. The turbidite above turbidite B is too soupy to retain any delicate structures during coring, while turbidites beneath have so far not been penetrated with the Kastenlot corer. Until such recovery of deeper turbidites is achieved, it must be assumed that the upper half of each turbidite can potentially carry a series of vertical open burrows. Consequently, the sediment column must be regarded as having alternating layers of more and less permeable sediments.

4.8 Glacial Erratics

Rock material deposited by drifting icebergs (glacial drift) has been found in several places in the GME region (Pratt, 1961; Von Rad, 1974; Huggett, 1985, in preparation). This material consists of glacial erratics which may vary in size from rock flour to large boulders. The purpose of this study is to calculate the distribution of glacial erratics and to estimate the probability of a penetrator impacting an erratic of any given size.

From a literature study of 288 dredge hauls and 1164 deep sea cores it was found that glacial erratics from the N. Atlantic did not reach further south than 26°N (Huggett, in prep.). The GME region lies close to this limit and was therefore expected to have relatively low concentrations of glacial erratics.

The data from Pratt (1961) and Von Rad (1979) consist of a collection of five glacial erratics, the largest of which has a diameter of 19 cm. These have only been used as indicators that ice rafting has taken place in the area, and not for quantitative determinations since the area covered in each survey is not known. Also, the top of the Great Meteor Seamount, from where the samples came, is a high energy environment in which sediment erosion and redeposition is taking place. Thus, the depositional age of these samples cannot be estimated and therefore they cannot be related to ice-rafted input rates for pelagic sediments.

The rate of ice rafting varies with time. The most recent high input period in the North Atlantic was at the end of the last glacial period (11,000 years B.P.). Cores taken from the GME area have shown that, in the flat-lying abyssal areas, sedimentation is dominated by an episodic input of fine-grained turbidites (see Section 4.1). The emplacement of a very recent turbidite (turbidite A), probably in the last few thousand years, may therefore have covered most, if not all, of the glacial erratics deposited around 11,000 B.P. In addition, the surface of this recent turbidite is very soupy thus any more-recently deposited erratics are likely to penetrate this turbidite rather than come to rest on its surface.

The probable scarcity of erratics at the sediment surface in the GME area makes quantitative sampling problematic. Two techniques have been used for sampling, dredging and sea-floor photography.

4.8.1 Dredging

Two areas of pelagic sediments lying above and out of reach of the turbidites have been dredged (see Table 4.3). Station D10328 was a measured run covering about 4400 m^2 of 'draped' pelagic sediments to the south of GME. This run collected six glacial erratics larger than 1.5 cm in diameter. Station D10978 was a run over a low abyssal hill to the north of the study area. It was not a measured run owing to the roughness of the topography and it collected in-situ basalts and manganese nodules but no glacial erratics.

4.8.2 Photography

Four camera runs using a new survey camera system developed at IOS were carried out (see Table 4.3). Station S126/6 covered about 43,000 m^2 of sea floor just to the east of the GME area over a more proximal part of the recent turbidite. Two rocks were observed, the largest of which was 17 cm in diameter. Their occurrence conflicts with current ideas on sedimentation in the region since the surface sediment is expected to be a soupy turbidite into which any large rocks should sink. A GLORIA sonograph taken over the same site as this camera run has revealed sediment lineations in these proximal turbidites which may be related to turbidite pathways (Section 3.2; Figs. 3.3 and 3.4, box C; Kidd et al., 1985). Further work is in progress to study these features and whether the observed rocks are associated with them. Station D10678 covered about 5900 m^2 of sea floor over the distal part of the A turbidite in the study area. No rocks were observed. Station D10689 covered approximately 40,000 m^2 (exact figure not known) of sea floor over an abyssal hill to the north. Abundant rock material was observed but was later found to be in-situ basalts and manganese nodules (see dredge station D10978; Table 4.3). Station D10693 covered 41,532 m^2 of sea floor over the distal part of the recent turbidite in the GME study area. No rocks were observed.

4.8.3 Discussion

(1) Data from the GME area

From the above results two points emerge. First, there are insufficient data from the GME area itself to study the size distribution of glacial erratics there. Second, the recent turbidite has blanketed the sea floor to such an extent that the erratics within the flat-lying areas cannot be reliably sampled.

The two rocks observed in camera run S126/6 may be visible because they lie off the recent turbidite which may be restricted to a pathway identified on the GLORIA sonograph. The size and shape (angular, 17 cm maximum dimension) of the larger rock suggests that it is a lithic fragment rather than pumice or indurated sediment. The observation of this material may, therefore, be significant in understanding the mechanisms of turbidite flow in the proximal areas. The only data from GME that may be used is, therefore, from station D10328 (dredge) and even this cannot be used to determine a size distribution as the sample size is too small.

(2) Distribution of erratics

In order to predict impact risks, size distributions of glacial erratics from areas to the north of the GME area are used. Data from the King's Trough Flank area (KTF; 42°N, 23°W; Kidd et al., 1983a) include samples from 21 good dredge stations. There appears to be no appreciable difference in the size distributions between these stations. This confirms the view that, in the open oceans, ice rafting mixes material from different sources to such an extent that no trends or provenance can be observed from whole dredge collections. The size distributions are, therefore, all derived from the same population which exhibits a log-normal distribution. The only difference between stations is in the bulk quantity (i.e. number of particles/km^2) of material on the sea bed which is a function of distance from source (latitude). Thus, it is argued that the log-normal distribution derived from stations in the North Atlantic can be applied to all the abyssal areas where ice rafting has taken place. The sparse data from the GME region (i.e. station D10328) may, therefore, be used to provide the bulk quantity of material for the distributions already established.

Detailed analysis of a sediment core in the KTF region has provided data on fluctuations in the rate of input of ice-rafted material down to the last interglacial (oxygen isotope stage 5). This has been used to provide a cumulative impact risk curve for pelagic sediments in the King's Trough Flank and other regions (Huggett, in prep.) (Fig. 4.11). For the turbidites in the GME region, however, a new curve must be drawn since the pelagic units are separated by thick turbidite layers. To this end, core 82PCS13 has been used to correct Figure 4.11 to include the turbidites (Fig. 4.12). These turbidites do not carry glacial erratics so they merely vertically stretch the record to give predictions down to 12.5 m (as opposed to 1.7 m in the pelagic oozes of the King's Trough Flank).

4.8.4 Conclusions

Impact probabilities for point (i.e. dimensionless) projectiles may be extrapolated in the GME area back to oxygen isotope stage 5 (or 12.5 m sediment depth). It is estimated that the maximum cumulative impact risk (for all erratics greater than 1.5 cm diameter) at 12.5 metres in the GME area is 0.015%. This assumes that no erratics overlap and has been calculated for a point projectile. The mean erratic size within this size range is 2.3 cm. In a 10 x 10 m square of sediment 0.015% becomes 150 cm^2 of erratics or 30 particles with a diameter of 2.3 cm. The average horizontal distance between particles is therefore 2 m, which is small compared with the cross-sectional area of a penetrator and justifies the assumption of a point projectile.

These estimates are based upon sparse data and, if considered significant, require further sampling to augment the available information on the GME area.

Table 4.1 - Cores studied for stratigraphy

Core No.	Type	Position		Water Depth corr. m	Core Length (m)
D10320	Gravity	31°05'.2N	25°50'.0W	5005	1.96
D10323	Gravity	30°21'.7N	24°06'.8W	5405	1.67
D10684	Kasten	31°21'.9N	24°45'.3W	5434	5.20
D10688	Piston	32°03'.0N	24°12'.1W	5428	10.01
D10690	Kasten	32°40'.8N	24°22'.3W	5421	2.06
D10695	Piston	31°23'.7N	24°46'.3W	5433	12.19
D10698	Piston	31°38'.2N	24°49'.8W	5433	12.96
D10699	Piston	30°43'.8N	24°29'.0W	5431	12.18
S126/2	Kasten	31°33'.2N	24°50'.5W	5446	4.15
S126/4	Kasten	31°31'.7N	24°25'.3W	5446	3.83
82PCS13	Piston	31°09'.5N	25°36'.2W	5433	21.83
82PCS17	Piston	30°19'.5N	24°39'.2W	5423	8.88
82PCS20	Piston	30°22'.8N	25°02'.9W	5433	15.30
82PCS34	Piston	32°41'.3N	24°23'.3W	5417	21.00

Table 4.2 - Summary lithology

Turbidite or Pelagic Stage	Present in cores	Max. and min. thickness of turbidite (cm)/core no.	Remarks colour, silty base, $CaCO_3$
A turbidite	82PCS13 82PCS20 82PCS34 S126/2 D10684 D10688	123/82PCS34 20/82PCS20 Complete recovery never certain	Very soupy, about 60% $CaCO_3$. Frequently not recovered probably because of coring problems. May have an irregular distribution since it was not present in IOS box core D10554.5 (31°30'.1N, 24°26'.6W)
stage 1	all cores		Marl, subdivided by A1 turbidite if this is present. May appear anomalously thick but this may be due to reworking of the A1 turbidite into the marl.
A1 turbidite	82PCS20 S126/4 D10684 D10688 D10695 D10698	17/83PCS20 2/D10695	Distinctive olive-green turbidite usually with a buff-coloured upper part which may be difficult to distinguish from overlying stage 1 material. $CaCO_3$ constant approx 30%. Not present in the west.
B turbidite	all cores	524/82PCS13 142/D10688	50-60% $CaCO_3$. Silty base usually present - may be over 1m thick east of 24°W but progressively less in a westward direction. Open burrows have been observed in this turbidite (Weaver & Schultheiss, 1983).
stage 2	all cores except 82PCS34 D10688		Pelagic clay. Always a very thin unit. Missing in 82PCS34, possibly as a result of current erosion near an abyssal hill, and in D10688 where it was possibly eroded by silty base of B turbidite.
C turbidite	see remarks		This is a problematical unit. In core 82PCS34 it may be an artefact produced by coring since it is extremely soupy.
stage 3	all cores		Marl. In cores D10688 and D10698 subdivided by a thin silt.

Table 4.2 - continued 2

Turbidite or Pelagic Stage	Present in cores	Max/min thickness of turbidite cm	Remarks colour, silty base, $CaCO_3$
D turbidite	all cores	167/82PCS13 35/D10688	$CaCO_3$ 40-50%
stage 4	all cores		Pelagic clay
E turbidite	all cores	371/82PCS13 139/D10688	$CaCO_3$ 50-60% Becomes progressively thicker towards the west (A. Kuijpers, pers. comm.)
stage 5	all cores		Marl. Often subdivided by E1 turbidite in central and western part of area.
E1 turbidite	82PCS13 82PCS34 D10698	46/82PCS13 35/D10698	$CaCO_3$ 50-60%. No greenish lower part may suggest originally with low organic carbon content. A second thin turbidite underlies E1 in 82PCS13.
F turbidite	all cores	500/D10699 329/D10688	$CaCO_3$ about 50%. Consistently the thickest turbidite. With a thick silty laminated base in D10699 and a thin silty base in 82PCS20, D10688, D10695 and D10698. Very green with a short paler green upper part.
stage 6	all cores		Pelagic clay. This unit does not appear to have been eroded by the thick silty base of the F turbidite in D10699.
G turbidite	all cores	195/D10698 129/D10688	$CaCO_3$ 50-60%. No greenish lower unit suggests originally deposited with low organic carbon content. Silty laminated base in D10688.
G1 turbidite	D10688 D10698	18/D10698 3/D10688	Appears very similar to G turbidite but slightly paler. May have been eroded by silty base of G in D10688.
stage 7	all cores		Pelagic clay and marl. Although predominantly an interglacial stage, stage 7 does have a short severe glacial within it. In the cores this seems to be reflected by a combination of pelagic clay and marl. These units are separated by the H turbidite.

Table 4.2 - continued 3

Turbidite or Pelagic Stage	Present in cores	Max/min thickness of turbidite cm	Remarks colour, silty base, $CaCO_3$
H turbidite	all cores	82/PCS20 37/D10688	$CaCO_3$ about 50% Thin silty laminated base in 82PCS20, D10699.
I turbidite	82PCS20 D10688 D10699	46/D10699 9/D10688	$CaCO_3$ about 30% in D10699 but in D10688 about 40%. This is probably due to bioturbation effects in such a thin unit. Strong green colour in D10699, but pale grey in D10688 presumably due to oxidation in such a thin unit.
stage 8	all cores except 82PCS34		Pelagic clay.
J turbidite	D10688 D10699	35/D10699 25/D10688	$CaCO_3$ about 80%. White ooze turbidite. Very thin sandy base in D10699. No green layers.
K turbidite	D10688 D10699	36/D10699 13/D10688	$CaCO_3$ 45% in D10699, 60% in D10688. Deep green colour in lower part of D10699; pale green in D10688. The reasons for these differences are at present unclear.
stage 9	D10688 D10699		Marly ooze.
L turbidite	D10699		$CaCO_3$ about 85%. White ooze turbidite.
stage 10	D10699		Pelagic clay.
M turbidite	D10699		$CaCO_3$ about 80%. White ooze turbidite.

TABLE 4.3 - Observations of erratic rocks in the GME area

STATION No.	MEAN POSITION		DEPTH (m)	AREA COVERED (m^2)	ERRATICS RECOVERED
A. Dredge Runs					
D10328	30°25.0'N	24°05.0'W	5412	4444	6
D10978	32°38.0N	24°19.0W	5300	Not known	0
B. Camera Runs					
S126/6	31°09.9'N	23°48.5'W	5418	43,353	2
D10678	31°23.8'N	24°34.6'W	5422	5862	0
D10689	32°39.5'N	24°19.5'W	5422-4871	approx. 4000	> 1000*
D10693	31°39.9'N	24°48.3'W	5433	41,533	0

* These "erratics" were later identified as manganese nodules and in-situ basalts.

FIGURE CAPTIONS

Figure 4.1: Lithology and coccolith stratigraphy of core 82PCS17. Blank intervals on the coccolith curve are due to absence of coccoliths in pelagic clay intervals. See Figure 4.5 for key.

Figure 4.2: Plot of sediment grain size distribution and lithology for cores D10688 and D10695.

Figure 4.3: Lithology of turbidite cores. Turbidites numbered as explained in text. Turbidites are missing at tops of cores D10698, D10699, D10695, D10690 and S126/4 owing to coring disturbance.

Figure 4.4: Calcium carbonate percentages through three piston cores. Note high carbonate values in turbidites J, L and M.

Figure 4.5: Pelagic intervals of turbidite cores 82PCS13, 82PCS20 and 82PCS34 plotted without intervening turbidites and compared with pelagic cores D10320, D10323 and 82PCS17 (upper part only). Coccolith stratigraphy plotted as cumulative percentages of five coccolith species. Blank sections are due to complete dissolution. Oxygen isotope stage boundaries are placed within the constraints of the coccolith stratigraphy at lithological changes.

Figure 4.6: Correlation of turbidite cores 82PCS13, 82PCS20 and 82PCS34 using correlation lines as derived in Figure 4.5. Turbidites present in all three cores are lettered consecutively from the top.

Figure 4.7: Correlation of turbidite cores D10688, D10698, D10699 and D10695.

Figure 4.8: Correlation of turbidite cores D10684, D10690, S126/2 and S126/4.

Figure 4.9: Large, open burrow and several small, vertical, open Trichichnus burrows on fractured surface of Kasten core S126/2. Ruler is aligned in vertical direction, scale (in centimetres) increasing down core.

Figure 4.10: Influence of open burrows on the permeability of deep-sea clays using Equation 4.1, n is number of tubes per square centimetre.

Figure 4.11: Graph showing the cumulative risk (per cent) of encountering glacial erratics ranging in size from 1.5 cm to 7800 cm (the largest credible erratic) in the pelagic oozes of the Great Meteor East area. This graph was derived from core D10333.

Figure 4.12: Graph showing the cumulative risk (per cent) of encountering glacial erratics ranging in size from 1.5 cm to 7800 cm (largest credible erratic) in the turbidite basin of the GME area. This graph was compiled from Figure 4.11 and core 82PCS13.

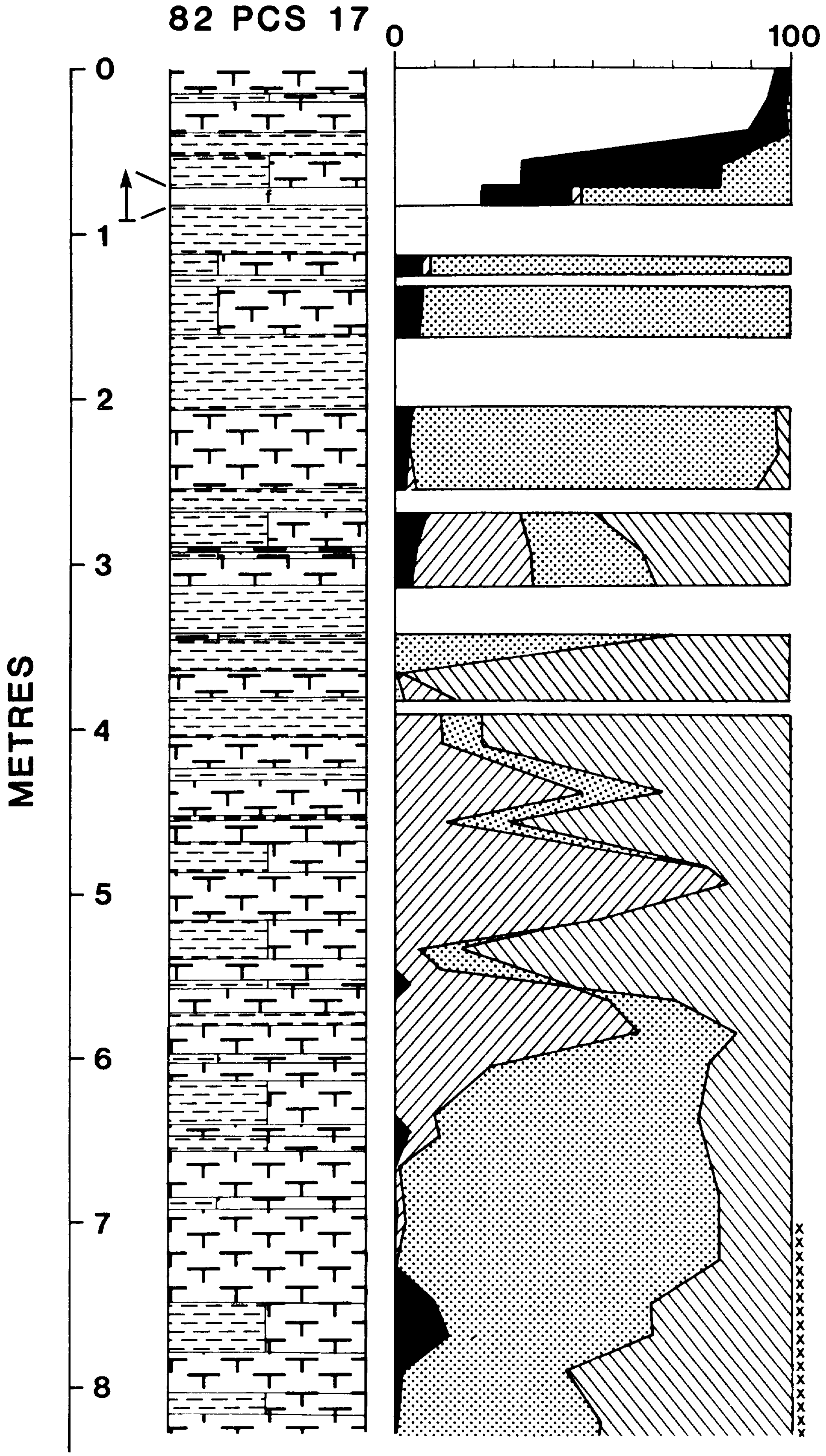

Figure 4.1 Lithology and coccolith stratigraphy of core 82PCS17. Blank intervals on the coccolith curve are due to absence of coccoliths in pelagic clay intervals. See Figure 4.5 for key.

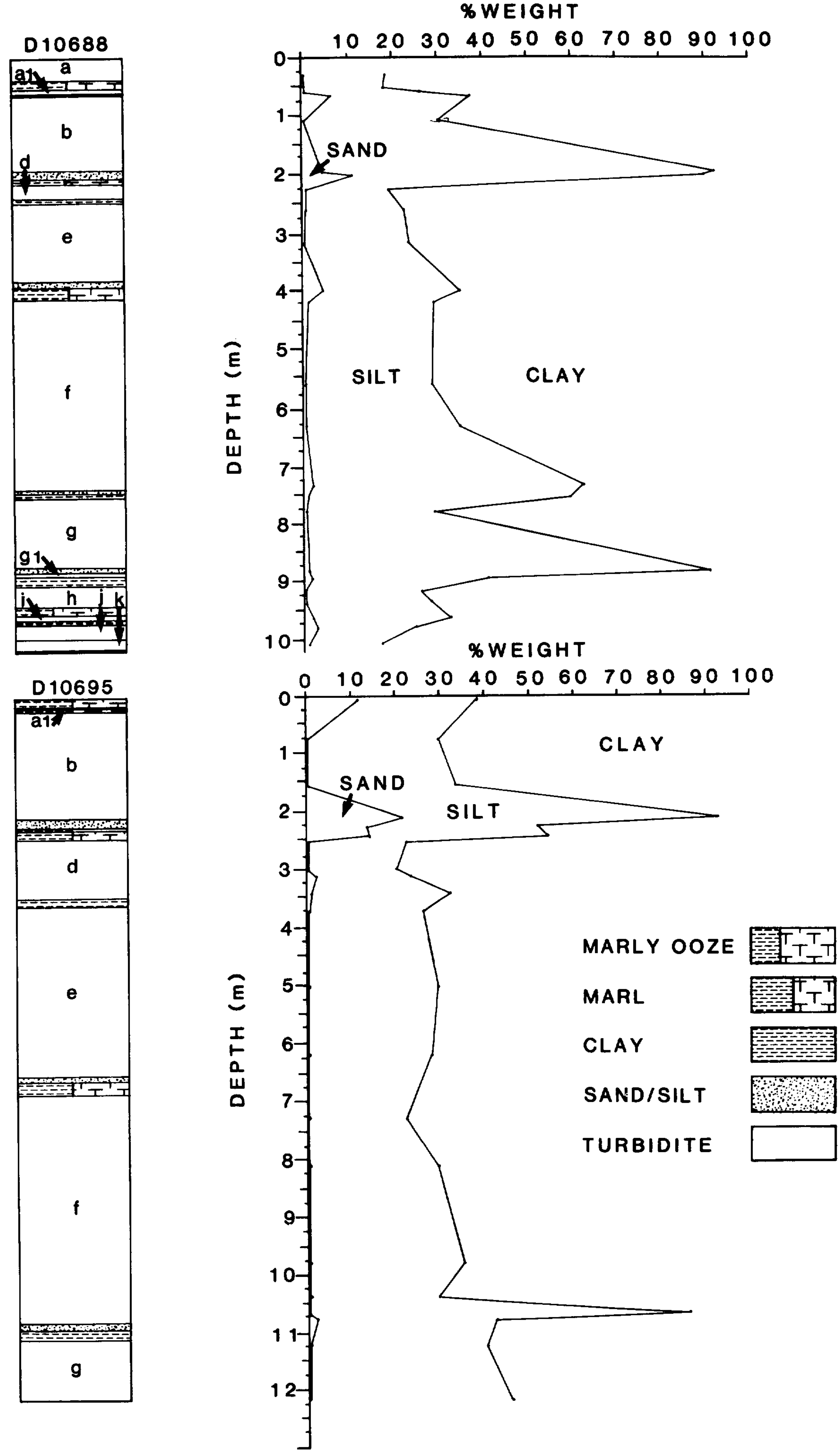

Figure 4.2 Plot of sediment grain size distribution and lithology for cores D10688 and D10695.

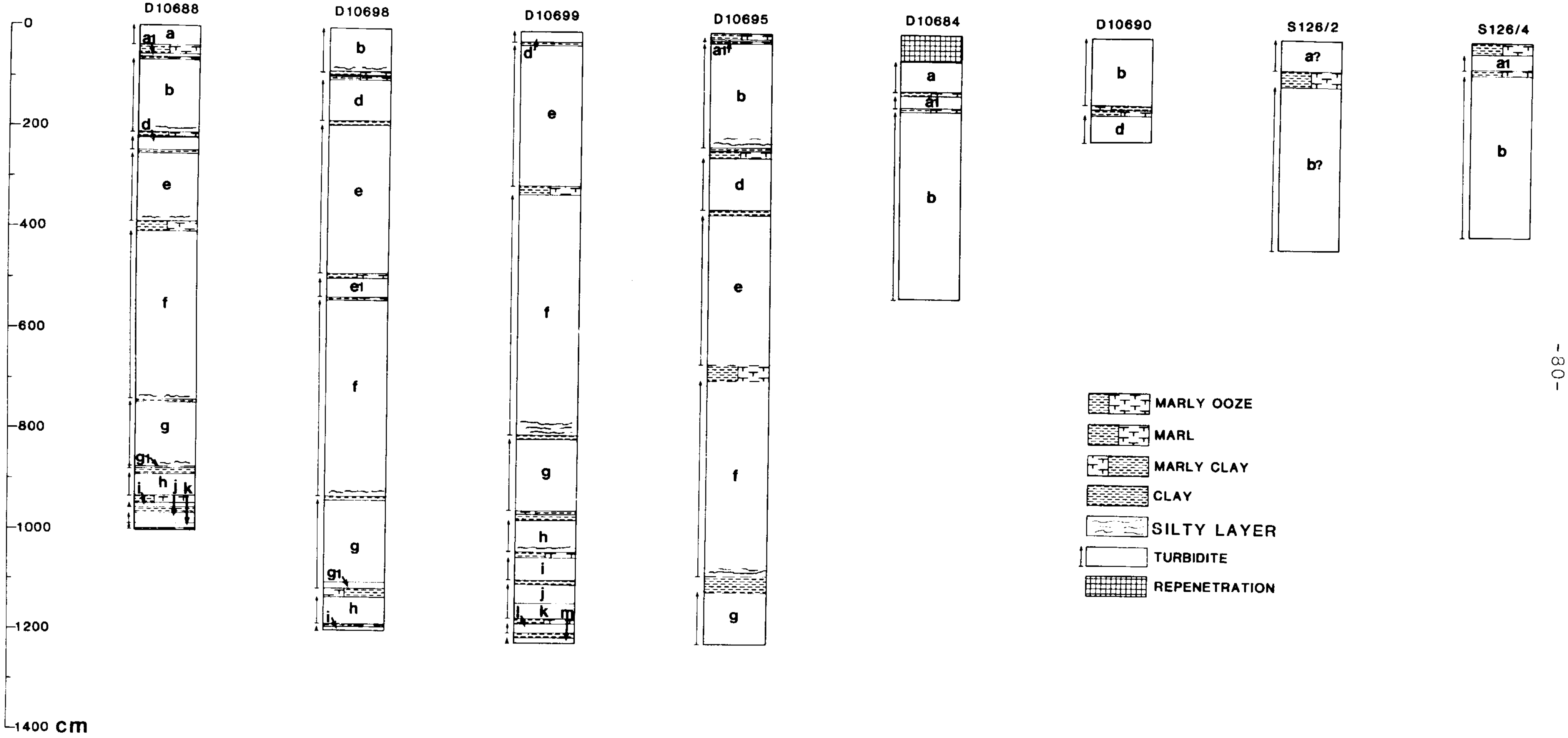

Figure 4.3 Lithology of turbidite cores. Turbidites numbered as explained in text. Turbidites are missing at tops of cores D10698, D10699, D10695, D10690 and S126/4 owing to coring disturbance.

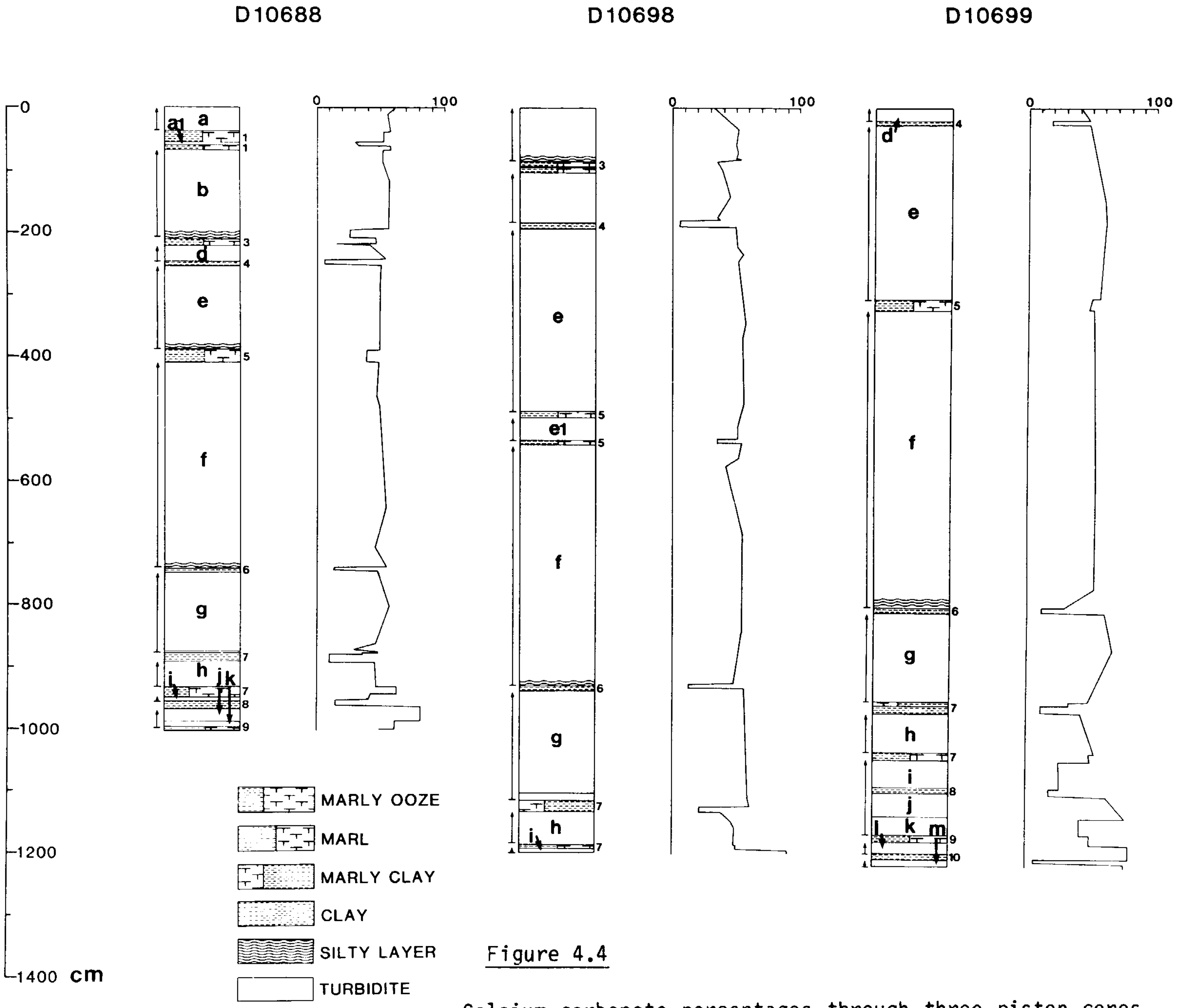

Figure 4.4

Calcium carbonate percentages through three piston cores. Note high carbonate values in turbidites J, L and M.

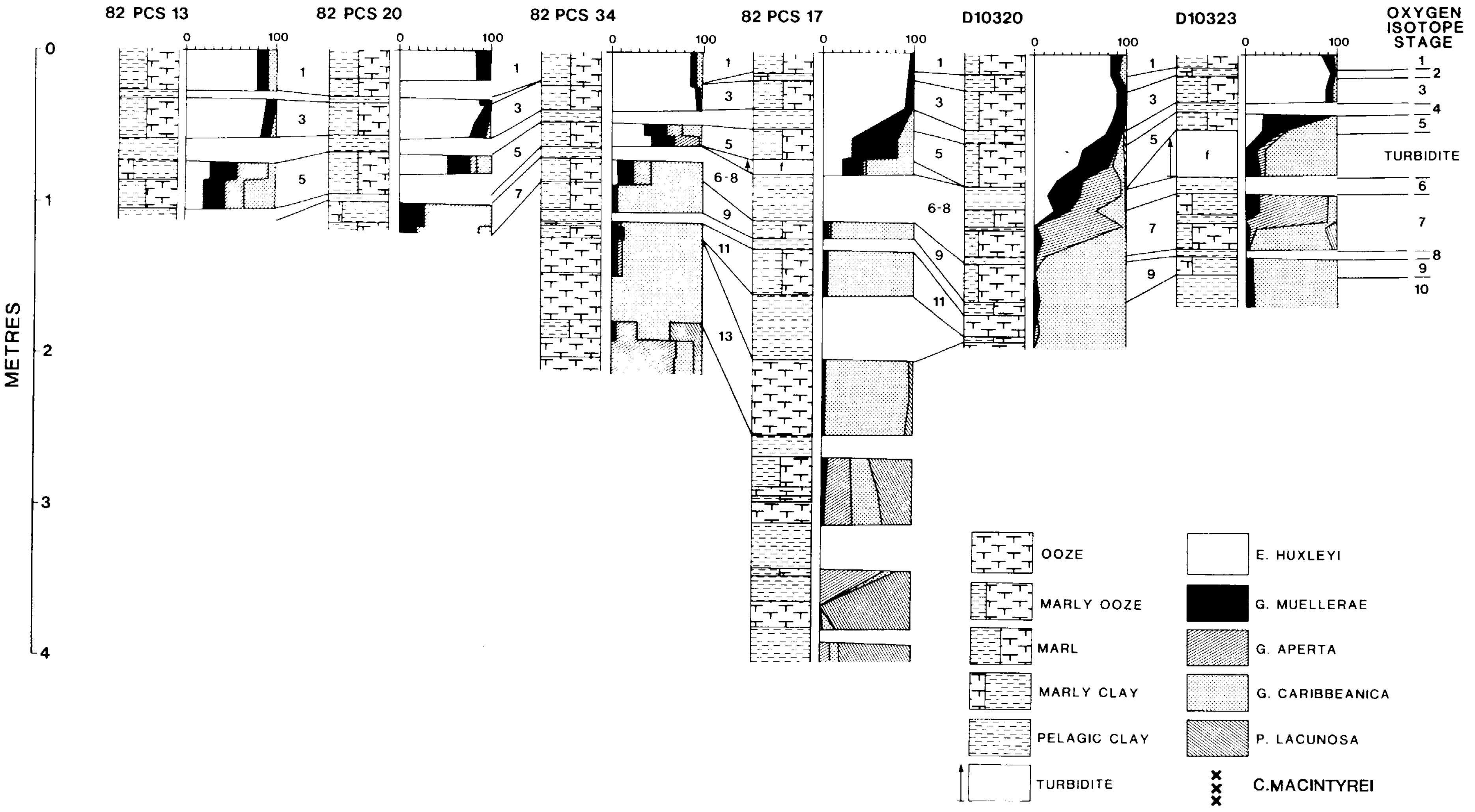

Figure 4.5 Pelagic intervals of turbidite cores 82PCS13, 82PCS20 and 82PCS34 plotted without intervening turbidites and compared with pelagic cores D10320, D10323 and 82PCS17 (upper part only). Coccolith stratigraphy plotted as cumulative percentages of five coccolith species. Blank sections are due to complete dissolution. Oxygen isotope stage boundaries are placed within the constraints of the coccolith stratigraphy at lithological changes.

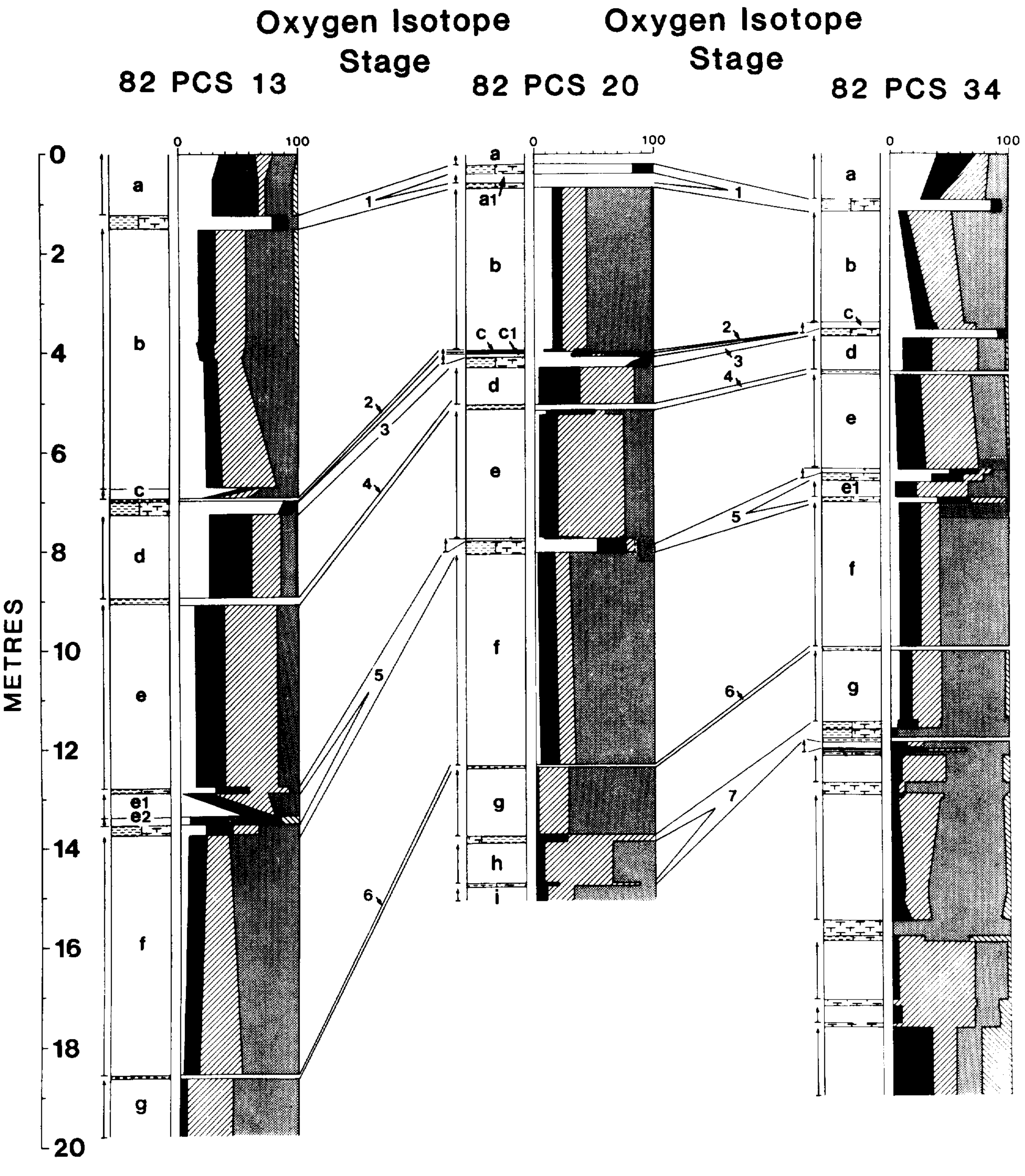

Figure 4.6 Correlation of turbidite cores 82PCS13, 82PCS20 and 82PCS34 using correlation lines as derived in Figure 4.5. Turbidites present in all three cores are lettered consecutively from the top.

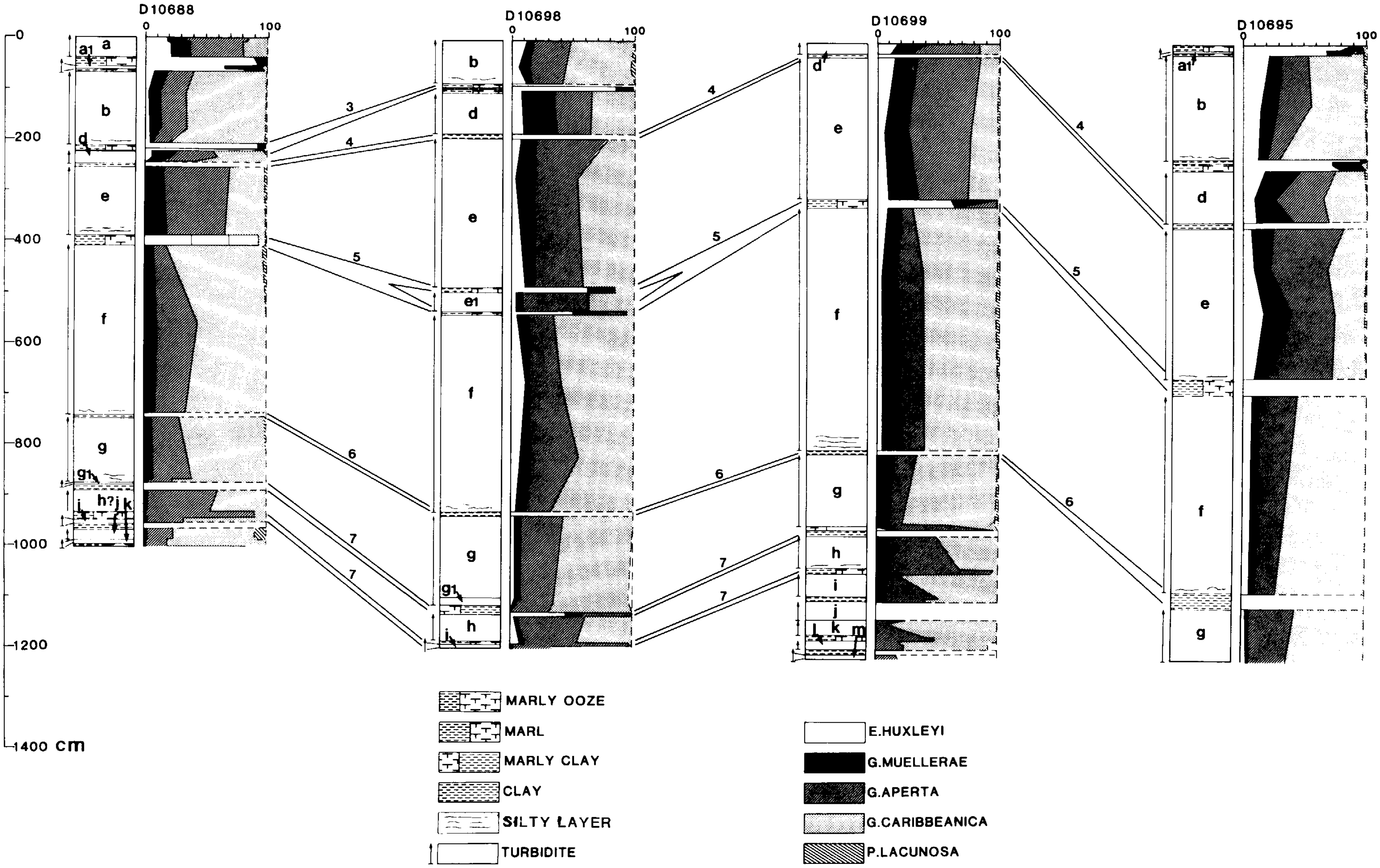

Figure 4.7 Correlation of turbidite cores D10688, D10698, D10699 and D10695.

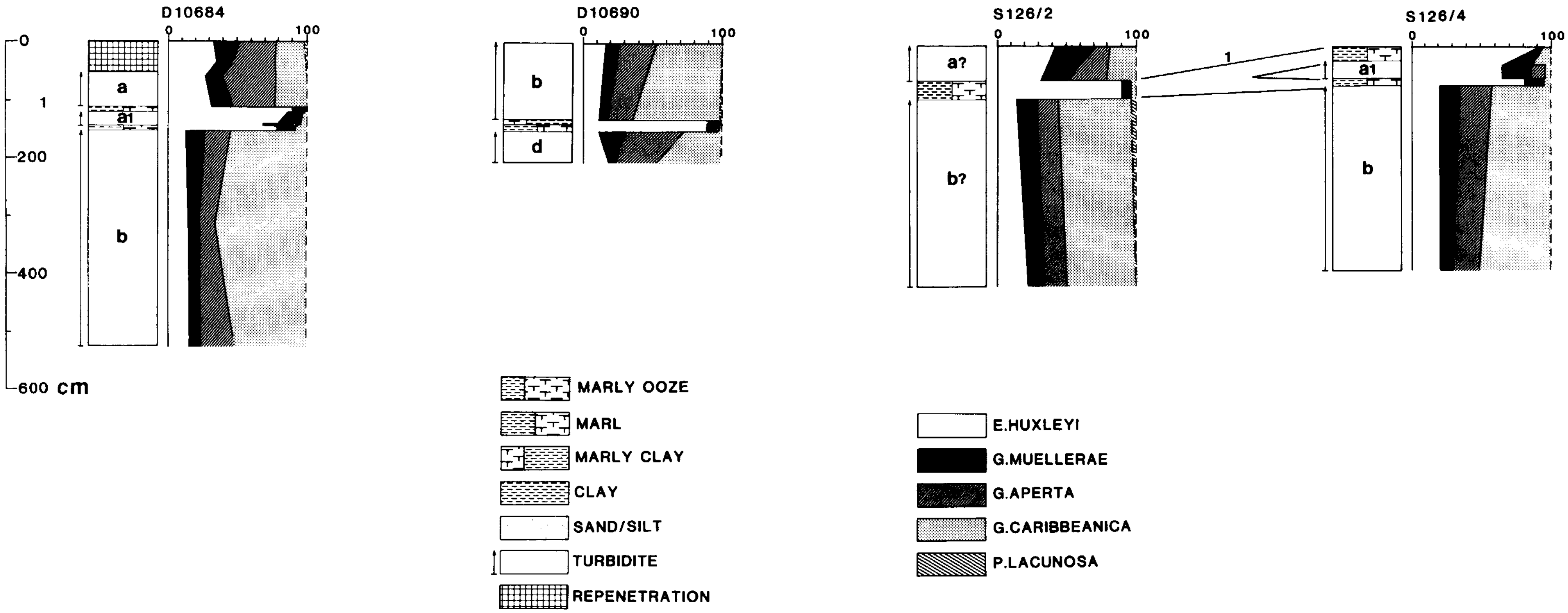

Figure 4.8 Correlation of turbidite cores D10684, D10690, S126/2 and S126/4.

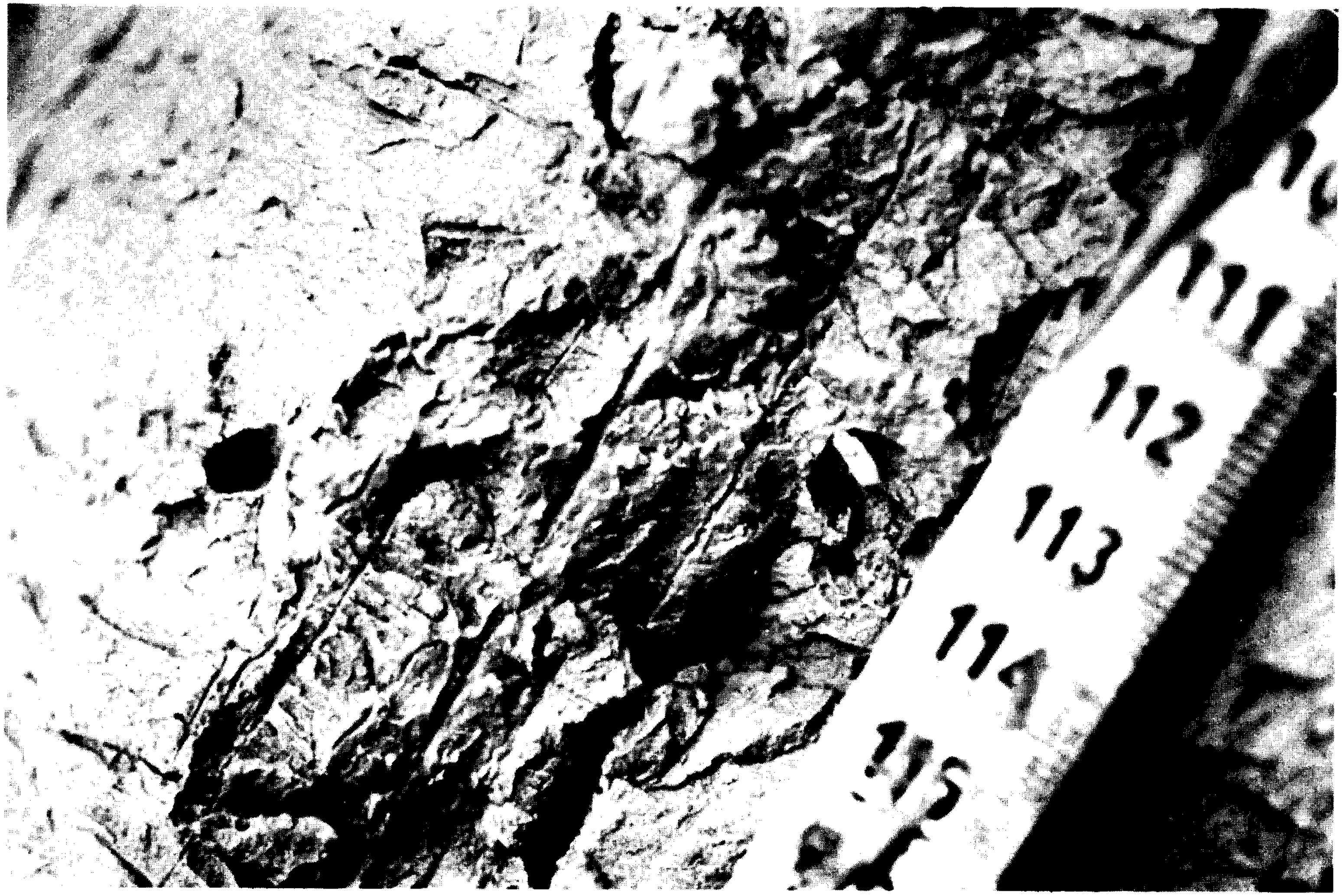

Figure 4.9 Large, open burrow and several small, vertical, open Trichichnus burrows on fractured surface of Kasten core S126/2. Ruler is aligned in vertical direction, scale (in centimetres) increasing down core.

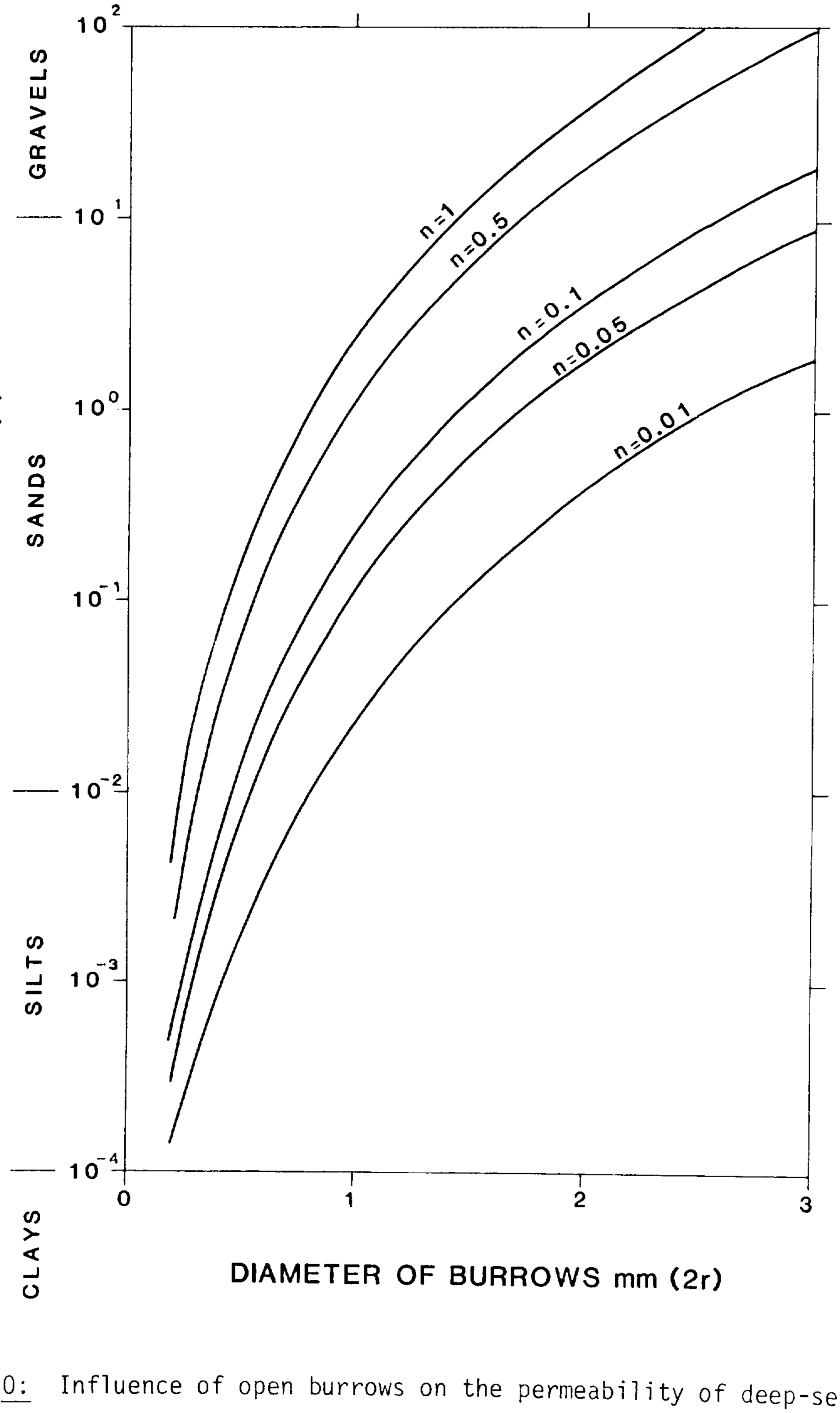

Figure 4.10: Influence of open burrows on the permeability of deep-sea clays using Equation 4.1, n is number of tubes per square centimetre.

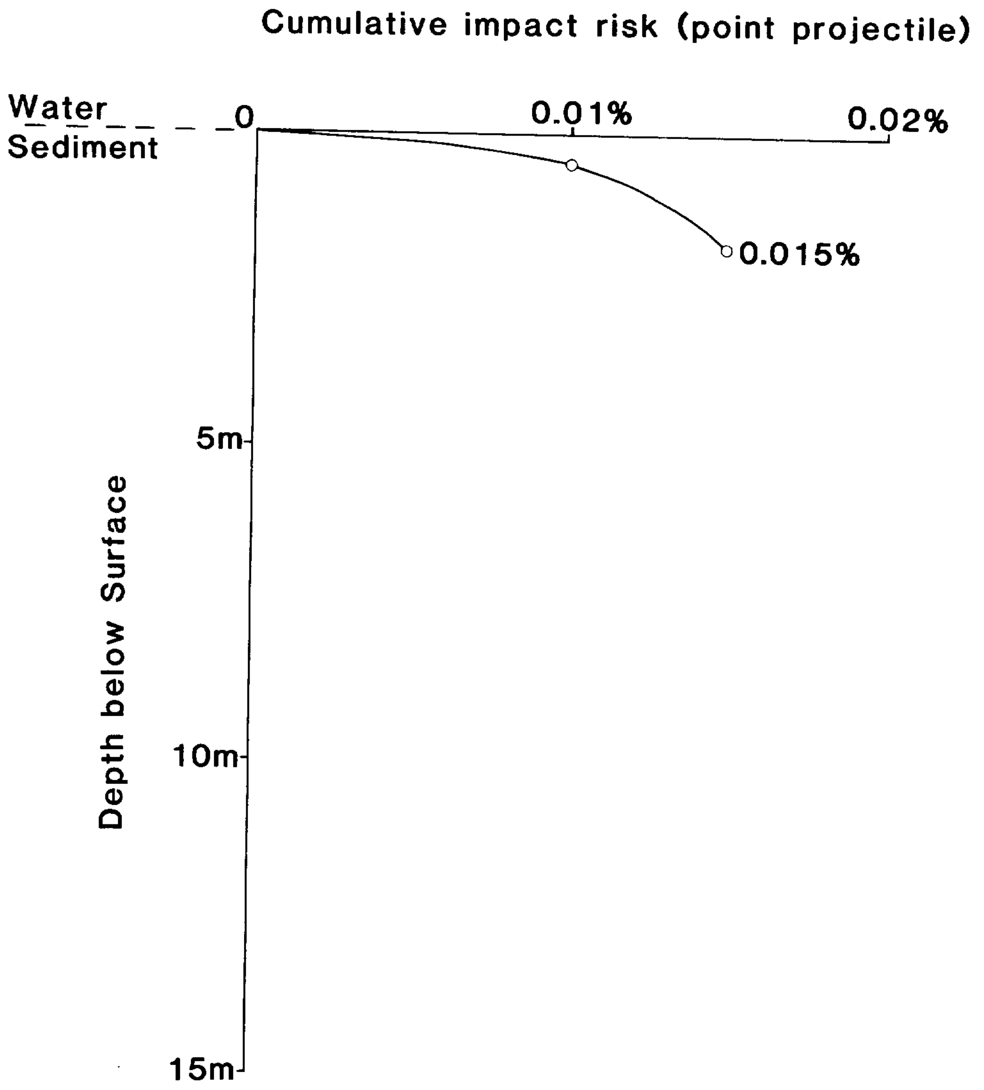

Figure 4.11 Graph showing the cumulative risk (per cent) of encountering glacial erratics ranging in size from 1.5 cm to 7800 cm (the largest credible erratic) in the pelagic oozes of the Great Meteor East area. This graph was derived from core D10333.

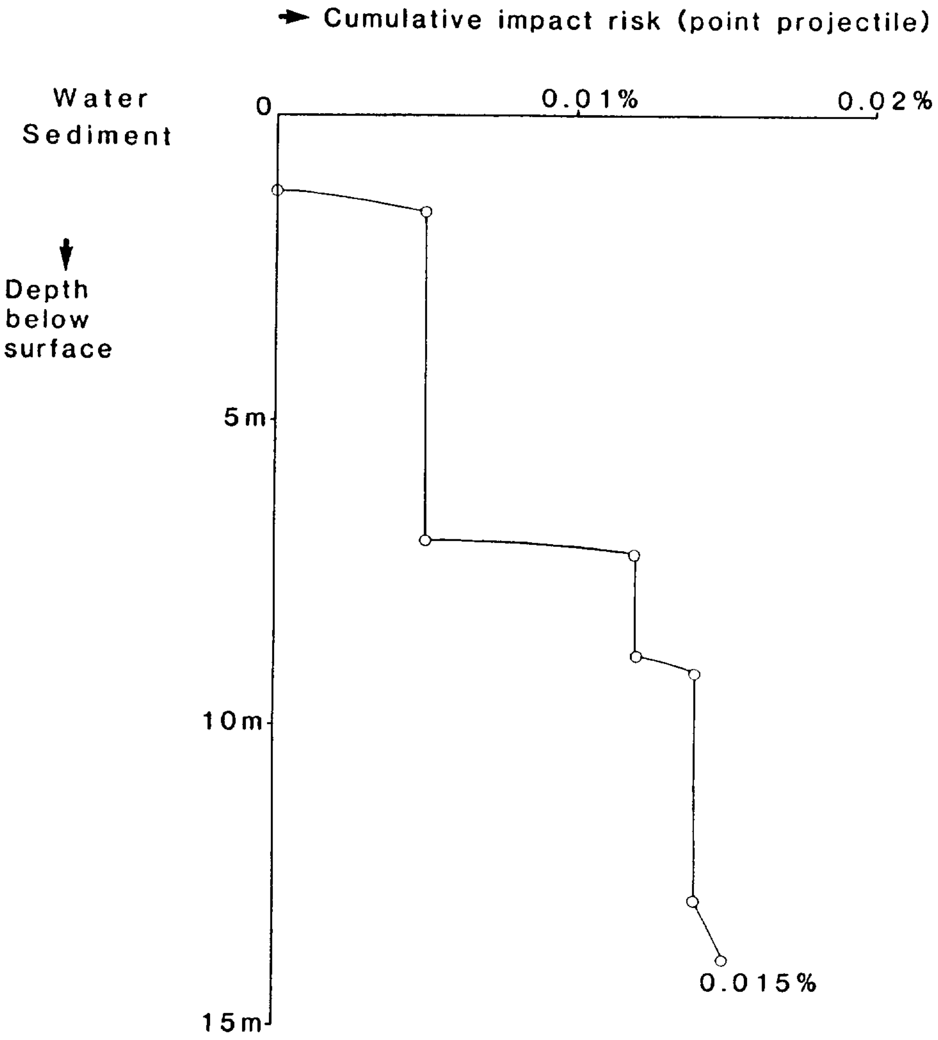

CUMULATIVE RISK OF IMPACT WITH ERRATICS
BETWEEN 1.5cm AND 7800cm DIAMETER
(COMPILED FROM CORE 82PCS13)

Figure 4.12 Graph showing the cumulative risk (per cent) of encountering glacial erratics ranging in size from 1.5 cm to 7800 cm (largest credible erratic) in the turbidite basin of the GME area. This graph was compiled from Figure 4.11 and core 82PCS13.

5. PORE WATER ADVECTION AND PHYSICAL PROPERTIES OF SEDIMENTS

5.1 Introduction

Although the GME study area lies within an abyssal plain in the NE Atlantic, it is possible that some advection of pore water might be occurring. Even very low advection velocities (a few mm yr^{-1}) would be very significant to the overall feasibility of disposing of high-level radioactive waste in the area. The 'physical properties' programme at IOS has concentrated its major effort into determining the magnitude and direction of any pore water advection in the area. In addition, a number of geotechnical and acoustic properties have been measured which may be of relevance to other aspects of the feasibility study. The following data have been obtained from some or all of the cores from the area: grain size and specific gravity, bulk density, porosity, void ratio, water content, permeability, vertical effective stress profile, over-consolidation ratio, compressibility index, compressional wave velocity and acoustic impedance profile.

Although any mechanism for pore water advection must be considered, the most realistic hypothesis is that pore water could be driven convectively by variations in temperature gradients between the igneous basement and the ocean water. It is generally accepted that anomalously-low measured values of conductive heat flux in areas close to active spreading centres can be accounted for by hydrothermal circulation through the highly-permeable ocean crust (Williams et al., 1974; Anderson et al., 1979; Becker et al., 1982; Becker & Von Herzen, 1983). As the ocean crust ages it is overlain by a blanket of sediments with low permeabilities. Consequently, any remaining convection is confined to the basement and heat flow through the sediments should occur by conduction only (Langseth et al., 1983). This change in pattern is shown schematically in Figure 5.1. However, pore-water advection through sediments has been inferred from the non-linearity of temperature profiles in the Crozet and Madagascar Basins (Anderson et al., 1979), the Sohm Abyssal Plain (Burgess & Judge, 1981), the Brazil Basin (Langseth & Herman, 1981), the Galapagos Rift (Becker & Von Herzen, 1983; Williams et al., 1979) and the Mariana Trough (Abbot et al., 1983). In these reports, the advection velocities estimated from non-linear temperature profiles, using techniques described by Noel (1984b), are typically 1m y^{-1}.

Crowe and McDuff (1979) have compared pore-water velocities calculated from both temperature profiles and pore-water chemistry from three sites in the equatorial Pacific. It was found that the velocities calculated using sulphate diffusion-convection-reaction models were two to three orders of magnitude lower than velocities calculated from the non-linear temperature profiles. This inconsistency led Noel (1984a) to consider mechanisms other than advection that might give rise to the now widely-reported non-linear temperature profiles. He concluded that several other mechanisms could be responsible including: sediment disturbance (caused by the entry of the probe), bottom-water temperature changes of only a few hundredths of a degree, and modest topographic relief. Consequently, while the heat flux measurements and direct observations indicate that hydrothermal convection does exist (especially at active spreading centres) there is considerable doubt about the reliability of temperature profiles in providing accurate assessments of pore water advection in sediments. In view of the importance of this topic to the feasibility of high-level radioactive waste disposal, another technique, which involves directly measuring the differential pore pressures and permeability in sediments, has also been pursued.

5.2 Pore-water fluxes

Any movement, or flux, of water through a porous medium will be accompanied by a pressure gradient. The relationship between pore pressure and volume flow was found by Darcy (and confirmed by many others) and can be simply expressed as:

$$Q = kAi \qquad (5.1)$$

where Q is the rate of flow ($m^3\ s^{-1}$)
k is the permeability ($m\ s^{-1}$)
A is the cross-sectional area (m^2)
and i is the hydraulic gradient = h/l

The hydraulic gradient, i, is the ratio of the pressure difference across the sample (expressed as a height of water, h) and the thickness of the porous sample, l (see Fig. 5.2). The velocity of an element approaching the porous layer, V_a (approach velocity) is given by:

$$V_a = Q/A = ki \qquad (5.2)$$

and the velocity of an element of water in the porous layer, V (seepage velocity) is given by:

$$V = V_a/n = ki/n \qquad (5.3)$$

where n is the porosity of the porous layer.

It is readily apparent that this simple expression could be used to determine the velocity of an element of water in deep-sea sediments.

For a simple model consisting of layers of sediments with different permeabilities and porosities and a vertical pore-water flux, it has been shown

(Schultheiss et al., 1984) that the time taken for an element of water to move through m layers is given by:

$$T = \sum_{j=1}^{j=m} n_j Z_j^2/k_j \Delta u_j \tag{5.4}$$

where n_j is the porosity of layer j
Z_j is the thickness of layer j
k_j is the permeability of layer j
Δu_j is the pressure gradient across layer j
and m is the number of layers.

Consequently, to determine T we need to know the permeability, thickness, porosity and pore-pressure gradient of each layer. The pore-pressure gradient of all the layers can be calculated from a single pore-pressure measurement in any layer, once the permeabilities are known, because

$$Q = k_1 i_1 = k_2 i_2 = k_3 i_3 \dots\dots\dots\dots \text{etc.} \tag{5.5}$$

Permeability (n), thickness (z) and porosity (k) can all be measured from core samples, although core size and disturbance will limit the accuracy to which the measurements can be made (Schultheiss & Gunn, 1982). The differential pore pressure (Δu) is the only parameter that cannot be measured in the laboratory and must be measured in situ. The complete programme to measure pore-water advection using the above theory is shown as a flow chart in Figure 5.3.

5.3 Coring

Two types of coring systems have been used in the GME area to obtain samples for laboratory testing: (a) a piston corer (PC) which takes a 65-mm diameter sample up to 12m in length, and (b) a Kastenlot gravity corer (KC) which takes 150-mm square sections up to 4m in length. The advantage of the Kastenlot corer is that it provides samples of very high quality but of limited length, whereas the piston corer takes long samples but the disturbance factor is probably greater owing to the narrow diameter of the barrel.

Cores taken on or close to the GME study area which are discussed in this section are listed in Table 5.1. The lithology and general description of these cores appears elsewhere in this report (Chapter 4; Table 4.2).

5.4 Laboratory consolidation and permeability testing

The technique used to measure the permeability characteristics of samples taken from cores is based around a one-dimensional, back-pressured consolidation system. A schematic diagram of the apparatus is shown is Figure 5.4. A full description of the equipment is given by Schultheiss (1984). The testing procedure is briefy as follows:

A sample, 75 or 50 mm in diameter and 20 mm thick, is uniaxially consolidated in incremental steps under a back pressure which ensures complete saturation of the sample. The stress-strain data provides a consolidation curve which gives information on the compressibility of the sample (compressibility index, CI) and the natural consolidation state expressed as the over-consolidation ratio (OCR). At the end of each incremental consolidation stage, a constant head permeability test is performed. The sample, of known thickness, is subjected to a hydraulic gradient by adjusting the relative heights (ΔH) of the air/water interface units. Water flows through the system and sample at a constant rate which is measured in the high precision capillary tubes. The test is repeated at different heads, ΔH, and the results plotted as flow rate versus hydraulic gradient. The permeability is obtained from the slope of the best straight line through these points according to Darcy's Law (equation 5.1). Consequently, the permeabilaity characteristics are measured as a function of load (or effective stress) on the sample and at different void ratios as the sample consolidates. Results from these tests are plotted as three graphs for each sample, an example of which is given in Figure 5.5. Graph 1 (bottom left) is an e-log σ plot (void ratio versus log vertical effective stress); this graph depicts the consolidation behaviour of the sample. Graph 2 (bottom right) is an e log k plot (void ratio versus log permeability); this graph characterises the permeability of the sediment type throughout the range of void ratios in the consolidation test. Graph 3 (top right) is a σ-log k plot (vertical effective stress versus log permeability); this graph illustrates the change in permeability with increasing overburden pressure assuming normal consolidation.

5.4.1 Results of permeability and consolidation tests

A summary of the pertinent consolidation and permeability parameters is given in Table 5.2. A few samples have been tested at the Universities of Oxford and North Wales and these have been designated OX and UCNW respectively. Differences in testing procedures for these samples are given by Schultheiss (1984). Orientation refers to the axis of the sample; hence, V (vertical) implies that the consolidation direction and the water flow was parallel to the core axis; H (horizontal) implies that the flow was normal to the core axis.

R is a remoulded sample. Sediment type is given by a broad definition based on carbonate analysis and microscope observation. The following broad classification has been used:

Per cent carbonate	
100 - 70	- ooze
70 - 30	- marl
30 - 5	- calcareous clay
5 - 0	- clay

The carbonate fraction is divided up into percentages of forams and nannofossils:

Per cent forams	Per cent nannofossils	
100 - 70	0 - 30	foram
70 - 30	30 - 70	foram nanno
30 - 0	70 - 100	nanno

Hence the following initials represent the sediment types shown in the table:

NM - nanno marl
FNM - foram nanno marl
CPC - calcareous pelagic clay

SUB BOTTOM DEPTH is the depth from the top of the core. In general this is assumed to be the sediment surface, although it is known not to be in D10695 and S126/4. e_0 is the initial void ratio. OCR is the over-consolidation ratio given by σ_c/σ_0. σ_c is an estimate of the maximum past pre-consolidation stress obtained from the e-log σ curve using the technique proposed by Casagrande (1936) and σ_0 is the vertical effective stress on the sample in situ (calculated by integrating the bulk density profile to the required depth). C_c is the compressibility index for the 'straight line' part of the e-log σ plot where C_c is given by

$$C_c = -\frac{\Delta e}{\Delta(\log \sigma)} .$$

C_c is thus the change in void ratio per logarithmic cycle of stress. The permeability of the sample at e_0 (k at e_0) is obtained from the e-log k plot at e_0. The in-situ permeability should strictly be predicted when $\sigma = \sigma_0$. However, with samples from sub-bottom depths less than four metres, σ_0 is less than 20 kPa and the permeability difference between 20 kPa and 0 cannot be accurately measured.

k_c is the permeability index which is defined by

$$k_c = \frac{\Delta e}{\Delta(\log k)}$$

and is taken from a straight line estimated from the e-log k plot. k_c is thus the change in void ratio per logarithmic cycle of permeability.

The GME study area is dominated by a sequence of distal nannofossil turbidites (thicknesses vary between a few centimetres and a few metres). The bases of some of the turbidites contain sands and silts which thin and eventually disappear as the units become more distal (i.e. in the west of the area). Between each turbidite unit a thin pelagic interval of marl or calcareous clay is present and is typically only a few centimetres thick (see section 4.1).

Figure 5.5 (D10695/2/14, sample from 168 cm below top of core D10695) is typical of the behaviour for the nannofossil turbidites. It exhibits a high void ratio and has a high compressibility index of 1.1. Samples from the same turbidite B in core S126/4 exhibit even higher void ratios towards the top (up to 5.2) with C_c values as high as 1.5.

At the base of some turbidites (in particular B and F) the silt component increases rapidly. Figure 5.6 (D10695/8/16, 1087 cm below top of core 10695) illustrates the behaviour of a very silty base. The void ratio is below 2 with a C_c value of only 0.5. To illustrate the change in permeability that occurs the profile for core D10695 is shown in Figure 5.7. It should be noted that the permeability in the silty bases can be over two orders of magnitude higher than in the bulk of the turbidite unit.

5.5 Correlation of cores and 3.5 kHz records

The 3.5 kHz records in the GME area are dominated by continuous parallel reflectors over most of the area. To enable the reflectors to be identified, four piston cores were acoustically logged before being split. Compressional wave velocities (V) were measured at intervals along the core not exceeding 5 cm, using a 1 MHz pulse technique, and were corrected to ambient pressure and temperature. Bulk density (ρ) measurements were taken at selected intervals along the cores after they were split. Acoustic impedance (ρV) profiles have been produced and are compared with the 3.5 kHz records below.

Figures 5.8 to 5.11 show the data for the four cores 10688, 10695, 10698 and 10699 respectively. The 3.5 kHz records have been enlarged considerably to the same scale and are shown next to the impedance profile. These profiles are dominated by sharp impedance contrasts at the turbidite bases which are caused by the coarser grain sizes producing high bulk densities and velocities.

The correlation between the 3.5 kHz records and the impedance profiles has been made by matching the reflections with the sharp impedance contrasts. It should be noted that about 3m of sediment is missing from the top of each piston core. This is consistent with observations made using the Kastenlot corer which puts the base of turbidite B at a sub-bottom depth of at least 4 metres.

At Station D10688 the IOS near-bottom high-resolution profiler (see Section 3.5) was run and the record is shown in Figure 5.8 alongside the 3.5 kHz record. The oscillatory nature of the record is a function of the ship's heave, not of the bottom topography. It is clear that the resolution of this type of record is far superior to that of the surface-towed 3.5 kHz profiler, although there is some indication of sub-bottom multiples in the record especialy within the E turbidite.

For the 3.5 kHz records it would seem that the observed reflectors do represent discrete geologic horizons and that they correlate with the bases of the major turbidites. Consequently, it is possible in an area such as GME to map the thickness and extent of the turbidites from 3.5 kHz records, hence eliminating the necessity to take large numbers of cores. Two sections across GME have been constructed on the basis of 3.5 kHz records calibrated by cores in this way and are shown in Figures 5.12 and 5.13.

5.6 Pore Pressure Measurements

To calculate the pore water advection velocity, given the permeability, it is necessary to know the differential pore pressure (section 5.2). A Pop-Up Pore Pressure Instrument (PUPPI) has been developed for this purpose. Because of problems associated with the very soft sediments in the GME area, no data were available at the time of writing. However, PUPPI had been used successfully on an area approximately 100 miles to the NE of GME.

The instrument is shown in Figure 5.14. It is allowed to free-fall through the water column and stops when the lance has penetrated the seabed. A differential pressure transducer and data logger monitor the pore pressure pulse and its decay. The instrument is designed to operate in water depths up to 6000 metres for periods of weeks or months if required, and measures the differential pore pressure at a depth of up to 3 metres into the sediment with a resolution of 0.05 kPa. A full decription of the instrument is given by Schultheiss *et al*. (1984).

In the region to the northeast of GME at Station D10943 (33°31.5'N, 22°58.05'W) an extrapolated pore pressure of 0.28 kPa was measured at 1.85m depth; this, when combined with suitable permeability estimates, gave an upward pore water advection velocity of less than 8 mm/y.

Further deployments of PUPPI in GME are planned for the latter half of 1984.

5.7 Heatflow and temperature gradients

The background to the geothermal studies has been given in section 5.1. Three stations have been made in the GME study area (D10318, S126.3 and S126.5; see Table 1.2 and Fig. 1.2), and a further three (D10301, D10405 and D10674) were made in the surrounding area (Fig. 5.15; Noel, 1984a). These stations were all made using heat-flow probes of the 'violin bow' type with repeated penetrations ('dips'). This allows both the geothermal gradient and the conductivity to be measured in situ.

If the heat and fluid flow are in the vertical, z, direction then the sediment temperatures can be obtained from the simplified differential equation

$$\frac{d^2T}{dz^2} - \frac{c\rho v}{K}\frac{dT}{dz} = 0$$

(de Vries, 1958; Stallman, 1963; Mansure & Reiter, 1979) where c, ρ and v are the specific heat, density and mean velocity of the moving incompressible fluid and K is the thermal conductivity of the sediment-fluid mixture. With boundary conditions $T(z) = T_0$ at $z = 0$ and $T(z) = T_L$ at depth $z = L$, Bredehoeft and Papadopulos (1965) obtain the following solution:

$$\frac{T(z) - T_0}{T_L - T_0} = \frac{e^{\beta z/L} - 1}{e^{\beta} - 1}, \text{ where } \beta = \frac{c\rho vL}{K} \qquad (5.6)$$

Advection causes the temperature profile to become convex in the direction of fluid motion. In general, when analysing the sediment temperature profiles presented in this report, it has proved satisfactory to estimate β by modelling a temperature profile using equation 5.6 and the method of least squares.

Further details of the experimental method and data tabulations are given in Noel (1984b).

5.7.1 Results

At the first successful station (D10301) ten penetrations were made by the probe along a 3 nautical miles transect on the northern Madeira Abyssal Plain to the NE of GME (Fig. 5.15). However, the temperature data clearly show that the probe had penetrated to depths of only one or two metres (Fig. 5.16). The mean geothermal gradient from these results is 0.076°C/m. No in-situ measurements of thermal conductivity were made. Assuming a typical thermal conductivity value for deep sea sediments of 2×10^{-3} cal cm^{-1} s^{-1} $°C^{-1}$, this gives a mean heat flow of 1.52 μcal cm^{-2} s^{-1}.

Station 10318 was located on the abyssal plain at the west end of GME (Figs. 1.2, 5.15). 500 lb of lead weights were attached to the probe and this ensured a full 5m penetration on four successive 'dips'. The data (Fig. 5.17) show temperature profiles which are linear within the resolution of the instrument. Again, assuming a sediment thermal conductivity of 2×10^{-3} cal cm^{-1} s^{-1} $°C^{-1}$, the mean heat flux for the station is 1.47 μcal cm^{-2} s^{-1}.

The new IOS/Cambridge heat probe was successfully deployed at three locations in or near the Great Meteor East study area during cruise 126 (Stations D10405, S126/3 and S126/5). Unfortunately, owing to failure of the heat pulse circuitry, no measurements of in-situ thermal conductivity were made.

At station 10405, on the abyssal plain to the NE of GME, six penetrations were made along an approximately 4 mile N-S transect. The results from Dips 1 and 3 reveal smooth, non-linear temperature profiles whose sense of curvature implies downward porewater advection (Fig. 5.18). This is discussed below. The remaining temperature profiles at this station are either linear within the measurement resolution (Dip 2) or show irregularities due to excessive thermistor drift (Dips 4, 5 and 6).

At the coincident stations S126.3 and S126.5 in the eastern part of GME the sediment temperature profiles were all linear within the resolution of the instrument (Figs. 5.19, 5.20). The mean geothermal gradient is 0.066 °C/m. Assuming a thermal conductivity of 2×10^{-3} cal cm^{-1} $°C^{-1}$ this gives a mean heat flux of 1.32 μcal cm^{-2} s^{-1}.

Needle-probe measurements of thermal conductivity were made on Kastenlot core 10406 (close to heat-flow station 10405). To test for the presence of thermal conductivity anisotropy, two measurements were made at each level in the core, viz: with the needle vertical and horizontal. Significant differences were found between most pairs of measurements. The maximum value is about 30% with no evidence for a correlation between enhanced anisotropy and lithostratigraphy. It is possible that the anisotropy reflects varying concentrations of platey minerals which are not necessarily confined to the marl or carbonate layers. In the absence of clear trends in the anisotropy profile, it seems very unlikely that a significant thermal conductivity anisotropy change with depth is in some way responsible for the non-linear temperature profiles recorded at the neighbouring station 10405.

Station 10674 was situated in the vicinity of the Plato and Atlantis seamounts, north of Great Meteor Seamount and NW of GME. Four dips were made along a 1.5 mile transect trending SE. The temperature records indicate partial penetration in each case to a depth of about 3m. However, the temperature profiles show consistent evidence for a gradient which decreases with depth which may imply upward porewater flow (Fig. 5.21). This is discussed further below. The mean heatflow was 1.15 μcal cm^{-2} s^{-1}.

Figure 5.22 shows the vertical sediment conductivity profile for each of the four dips of station 10674. There appears to be a consistent trend of decreasing thermal conductivity with depth, the total change amounting to about 40%. Studies of core samples have shown that the water content of deep-sea sediments is highly variable to depths of 10m or more. Since thermal conductivity is inversely related to water content (e.g. Ratcliffe, 1960) these results could thus be explained by a rapid increase in sediment porosity in the first 4m. Alternatively, it is possible that the penetration of the probe has in some way increased the water content of the deeper (disturbed) material by dragging down bottom water and surface material.

5.7.2 Discussion

The general locations of heat-flow stations in the vicinity of GME are shown in Figure 5.15 and in more detail in Figure 1.2. The world Heat Flow Data Collection (Jessop et al., 1976) lists no previous measurements in this study area.

Station 10674 was situated in a small sedimentary basin about 400 km NW of GME at a water depth of about 3400m. The results show consistent non-linear temperature profiles for Dips 2, 3 and 4 whose gradients decrease with depth. At Dip 1 the suggestion of a non-linearity is based on a single temperature reading and is, therefore, best discounted (Fig. 5.21). Assuming, initially, that the curvature is due to advection, the flow rates for Dips 2-4 have been calculated using equation 5.6 and range from 98 to 127 cm/y. The mean velocity is 112 cm/y and would be sufficient to raise buried waste materials in solution from a depth of 30m to the surface in only 27y. However, the data could also be explained by several alternative mechanisms. For example, if changes in bottom water temperature had occurred then a temperature wave could be present in the sediment. Enhanced current velocities may have been the cause of variable bottom water temperature. The curvature in the temperature profile would then reflect the amplitude and phase of the surface disturbance (Noel, 1984a). It does seem possible that, in this region of relatively shallow water, an increased instability in bottom water temperature could have caused these curved temperature profiles.

The curvature could also be explained by a continuous heat production in the sediment. Possible mechanisms include exothermic chemical reactions during diagenesis or biological activity; the conversion of potential energy into heat during compaction; the attenuation of continuous microseismic noise; or the heat released by radioactive decay. Other explanations include the disturbance caused by rapid sedimentation or erosion, or by uneven topography which can be particularly important when the topographic scale is comparable to the probe length. The insertion of the probe into the sediment may also disrupt the original temperature distribution. These and other factors have been discussed in detail by Noel (1984a). In the present context it seems unlikely that unstable sedimentation has been responsible for the non-linearity since the probability of the measurement occurring soon after an erosional event such as a slump is very low. However, the influence of large topographic features such as furrows or sandwaves cannot be ruled out without further detailed mapping. Hence this estimate of the rate of pore-water advection should remain tentative.

Station 10318 is located on the western extremity and 126.3/5 is near the centre of the Madeira Abyssal Plain, both within GME. Water depths are around 5400m. Both stations record remarkably linear temperature profiles from a total of eight penetrations. This reflects either the absence of pore water movement in the sediment or an increased stability of bottom water temperatures in this deep water basin.

In contrast, although similar physical conditions prevailed at Station 10405 (Fig. 5.15), two measurements (Dips 1, 3) recorded the largest departures from linearity of all the temperature profiles described in this report (Fig. 5.18). When the results are modelled using equation (5.6), downward advection velocities of around 6 m/y are suggested. This extreme result seems rather improbable in view of the large differential pore pressures that would be required to drive the pore water through the low permeability underlying sediments. Similarly, it is difficult to explain these results in terms of a change in bottom water temperature since the required fluctuation is excessive (> 1°C) when compared with deep-ocean mooring data from the same area of the Atlantic (Müller, 1981). Alternatively, the curvature may have arisen from a very large conductivity contrast in the surface sediments (rather unlikely), topographic features with wavelengths and heights of several metres, or by a slump or turbidity flow less than a year before the measurements were made (Noel, 1984a).

All dips at Station 10301 (Fig. 5.15) lacked sufficient penetration to assess accurately the probability of pore-water advection from the temperature data.

The two stations (10674, 10405) near the Great Meteor East study area that present possible evidence of rapid pore water advection should be checked by repeat measurements and by estimates based on other methods. These include O^{18}/O^{16} analyses of porewater linked to micropalaeontological studies, geochemical measurements, and direct recording of the sediment pore pressure gradient.

5.8 Controlled source seismology

During Discovery cruise 118, two ocean bottom seismographs were used to record Scholte waves (waves that travel along the sediment-water interface) and S-waves generated by artificial sources (Whitmarsh & Lilwall, 1982). The experiment was located near 32°35'N, 22°30'W, in a water depth of 5262 m on the lowermost continental rise. The seismic sources were large weights and projectiles dropped from the sea surface.

Two types of S-wave were recorded and were interpreted as S_H and S_V (i.e. with horizontal and vertical polarisation, respectively). S_H travelled 26% faster than S_V, indicating a strong seismic velocity anisotropy. This could result either from the preferential alignment of sediment grains within an essentially homogeneous medium, or from variations in physical properties between interlayered beds. Although the sediments were not sampled at this site, their regional setting suggests that they probably contain interlayered turbidites and pelagic material, so that the second explanation (perhaps with a contribution from the first) seems most likely.

The Scholte waves were dispersed; that is, the higher frequencies travelled more slowly than the low frequencies. This is because lower frequency (higher wavelength) components affect a greater vertical extent of sediment and therefore 'sample' a greater proportion of the higher velocities that occur deeper in the sediment column. The dispersion is mainly a function of the S-wave velocity structure of the sediment. The observed dispersion characteristics were well fitted by a model in which the S-wave velocity increases from about 30 m s^{-1} at the surface, via two zones of linear velocity gradient (16-17 s^{-1} down to 4 m, followed by 8-9 s^{-1}) to 170 ms^{-1} at 12 m depth. A quadratic, rather than bi-linear, increase in velocity with depth would fit the data equally well, though it is harder to model. Such a gradient would imply a linear increase of the dynamic elastic shear modulus with depth. The best-fit values for the shear modulus are 2 MPa at the surface increasing linearly to 52 MPa at 14 m (Figure 5.23).

5.9 Penetrators

Four penetrators were dropped from Discovery on cruise 134, and their decelerations through the sediments were monitored using a Doppler sonar technique (Freeman et al., 1984). Two penetrators were dropped at 31°26'N, 24°44'W (station D10686) and two at 31°24'N, 24°03'W (Station D10687). The penetrators were specially designed by the Building Research Establishment and the European Joint Research Centre for these experiments. They were made of solid steel, had dimensions of 3.2 x 0.325 m and weighed 1800 kg.

The penetrators achieved terminal velocities of around 50 ms^{-1} and penetrated over 30 m. By modelling the forces acting on the penetrators during deceleration it was possible to infer approximately the variation of undrained shear-strength with depth. This ranged from 3 kPa at the surface to a maximum of about 50 kPa at 30 m, although uncertainties concerning values of some of the parameters assumed in the calculation render these estimates provisional. Four distinct peaks were seen in the inferred shear strength profile, with peak to trough variations of up to 40%. These peaks may reflect the influence of stiffer silty layers within the sediment, but they could also be artefacts due to velocity variations.

Table 5.1 - Cores from GME on which physical property measurements have been made.

Core	Water Depth m	Latitude	Longitude
D10321 (KC)	4978	31°04'.8N	25°49'.3W
D10325 (KC)	5407	30°22'.9N	24°05'.8W
D10688 (PC)	5428	32°03'.0N	24°12'.1W
D10695 (PC)	5433	31°23'.7N	24°46'.3W
D10698 (PC)	5433	31°38'.2N	24°49'.8W
D10699 (PC)	5431	30°43'.8N	24°29'.0W
S126/2 (KC)	5446	31°33'.2N	24°50'.5W
S126/4 (KC)	5446	31°31'.7N	24°25'.3W
S126/15 (KC)	5330	30°22'.0N	23°35'.0W

Table 5.2

CORE	SAMPLE	TESTED AT	ORIENTATION	SEDIMENT TYPE	SUB-BOTTOM DEPTH m	e_o	OCR	C_c	k_c	k at e_o mm/s x 10^{-6}
D10321	6	OX	V	CPC	0.52	3.59	38.0	1.3	1.7	3.0
	7	OX	H	CPC	0.52	3.38	29.0	1.2	1.9	2.0
	10	OX	V	CPC	0.92	2.69	11.0	0.8	0.9	10.0
	11	IOS	V	CPC	0.92	2.67	2.9	0.8	1.2	20.0
	16	OX	V	FNM	1.46	2.42	12.0	0.5	0.6	10.0
D10325	4	OX	V	FNM	0.20	3.08	50.0	1.1	1.1	10.0
	5	IOS	V	FNM	0.28	2.49	117.0	0.9	1.0	150.0
	7	IOS	V	FNM	0.44	2.54	6.3	0.8	0.9	21.0
	12	OX	V	CPC	1.01	2.98	3.4	0.9	0.8	40.0
D10695	2/69	IOS	V	SILT	2.23		3.1		0.5	
	8/16	IOS	R	SILT	(10.77)	1.74	-	-	0.6	900.0
	3/82	IOS	V	NM	3.90	3.00	1.3	0.9	1.5	
	6/28	IOS	V	NM	7.94	3.68				
	2/14	IOS	V	NM	1.68					
	5/46	IOS	V		6.60					
S126/2	1	UCNW	V	NM	0.44	5.43	1.0	1.2	-	-
	3	IOS	V	FNM	0.62	2.43	7.0	0.5	1.5	85.0
	4	UCNW	V	FNM	0.70	3.44	10.0	0.8	-	-
S126/4	4	IOS	V	NM	0.74	4.76	18.0	1.4	1.4	150.0
	5	IOS	V	NM	1.02	5.20	5.5	1.5	1.8	160.0
	6	IOS	H	NM	1.02	5.46	5.5	1.5	2.2	70.0
	9	IOS	H	NM	3.44	3.54	2.3	1.2	1.8	30.0
	10	IOS	V	NM	3.44	3.73	5.0	1.2	1.8	30.0
S126/15	4	UCNW	V	CPC	1.66	2.22	5.0	0.7	-	-
	11	UCNW	V	CPC	1.79	2.54	1.8	0.7	-	-

FIGURE CAPTIONS

Figure 5.1: Schematic section through spreading centre and ageing ocean crust showing the postulated changes in hydrothermal circulation brought about by overlying sedimentation and reduction in basalt permeability. Graphs show predicted sediment pore pressure gradients (Δu).

Figure 5.2: Schematic diagram to illustrate the relation between hydraulic gradient and flow through a sample.

Figure 5.3: Flow chart for the IOS programme of natural pore water flux studies.

Figure 5.4: Schematic diagram of the IOS consolidation/permeability apparatus.

Figure 5.5: Graphical representation of the results of a typical consolidation/permeability test on nanno marl turbidite B (Sample D10695/2/14).

Figure 5.6: Results of consolidation/permeability test on the silty base of turbidite F (Sample D10695/8/16).

Figure 5.7: Lithology with measured permeability for core D10695.

Figure 5.8 Section of 3.5 kHz record and acoustic impedance profile for core D10688. Also shown is the record from the near-bottom profiler which was obtained nearby on Station D10691.

Figure 5.9: 3.5 kHz record and acoustic impedance profile for core D10695.

Figure 5.10: 3.5 kHz record and acoustic impedance profile for core D10698.

Figure 5.11: 3.5 kHz record and acoustic impedance profile for core D10699.

Figure 5.12: N-S transect across GME showing the depth to the base of turbidites B and D, E, and F, based on 3.5 kHz profiles and cores.

Figure 5.13: W-E transect across GME showing the depth to the base of turbidites B and D, E, and F, based on 3.5 kHz profiles and cores.

Figure 5.14: Pop-Up Pore Pressure Instrument (PUPPI).

Figure 5.15: Positions of heatflow stations in and near GME.

Figure 5.16: Sediment temperature profiles measured at station D10301. It is evident that the probe only penetrated to a depth of 1-2m.

Figure 5.17: Sediment temperature profiles measured at Station D10318.

Figure 5.18: Sediment temperature profiles measured at Station D10405.

Figure 5.19: Sediment temperature profiles measured at Station S126/3.

Figure 5.20: Sediment temperature profiles measured at Station S126/5.

Figure 5.21: Sediment temperature profiles measured at Station D10674.

Figure 5.22: Thermal conductivity measurements at Station D10674. (Note: $1 Wm^{-1}K^{-1} \simeq 0.24$ cal $m^{-1}K^{-1}s^{-1}$).

Figure 5.23: Modelled shear-wave velocity (left) and shear modulus to fit the observations of dispersed Scholte waves recorded from a weight-drop experiment at GME (after Whitmarsh & Lilwall, 1982). The two V_S curves shown approximate a bi-linear (dashed line) and a quadratic (solid line) increase with depth.

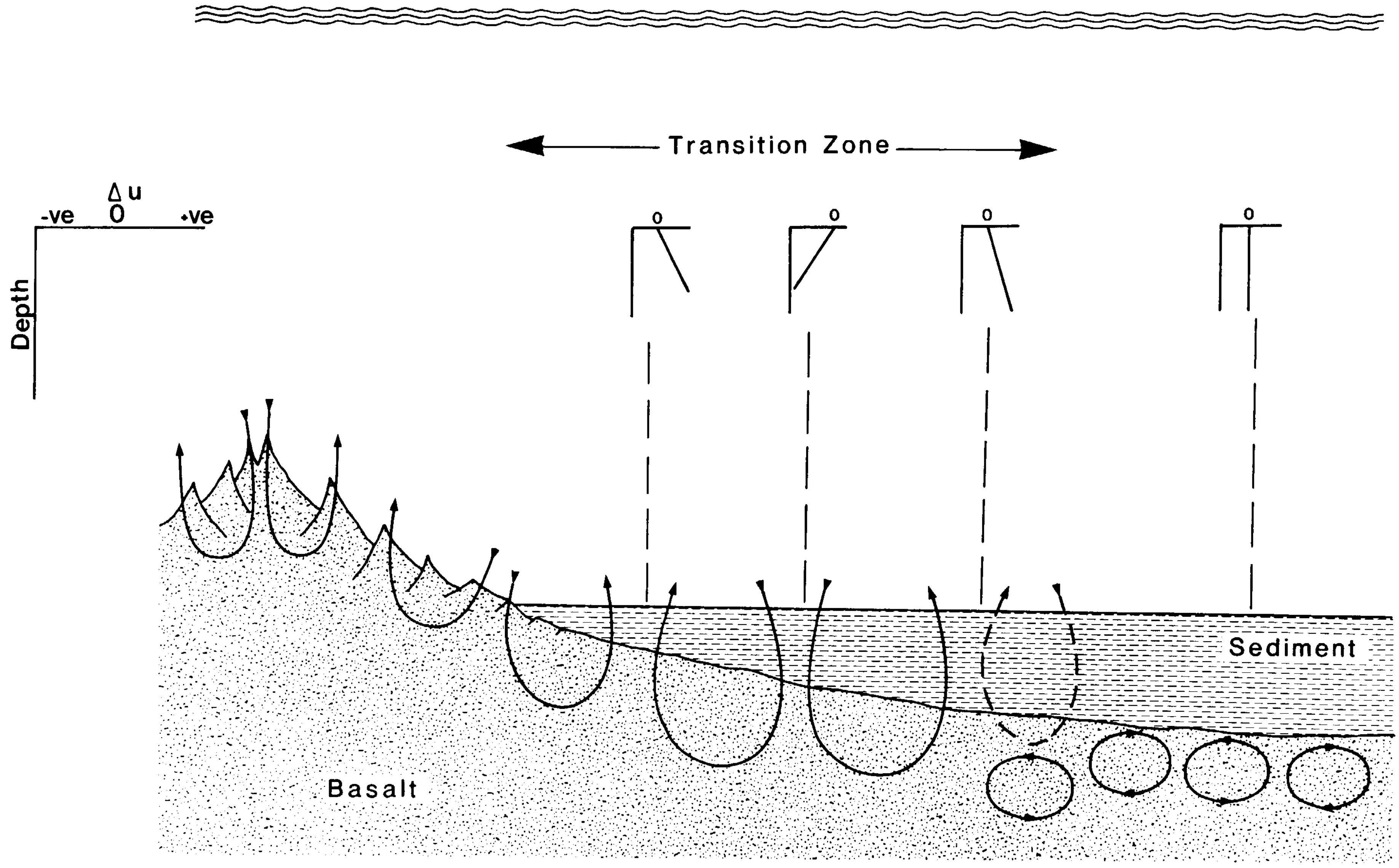

Figure 5.1 Schematic section through spreading centre and ageing ocean crust showing the postulated changes in hydrothermal circulation brought about by overlying sedimentation and reduction in basalt permeability. Graphs show predicted sediment pore pressure gradients (Δu).

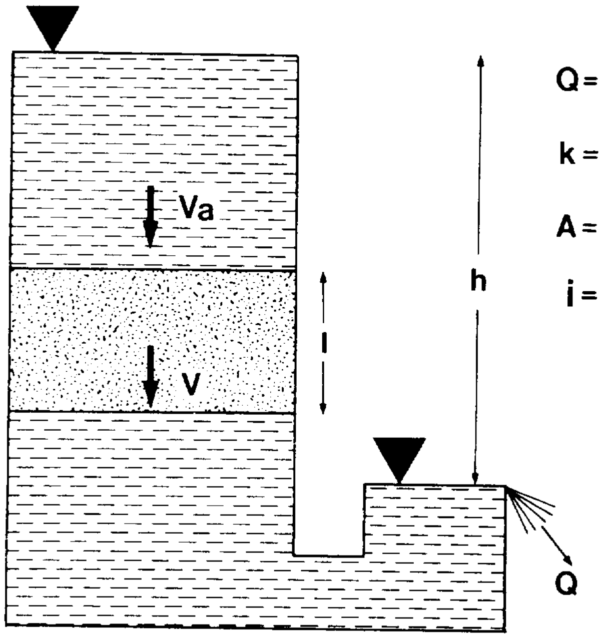

Q= flow rate ($m^3 s^{-1}$)

k=permeability ($m\,s^{-1}$)

A=cross sectional area (m^2)

i=hydraulic gradient (h/l)

Darcy's Law $Q = \frac{kAh}{l}$

Approach Velocity $V_a = ki$

Seepage Velocity $V = \frac{ki}{n}$

Figure 5.2 Schematic diagram to illustrate the relation between hydraulic gradient and flow through a sample.

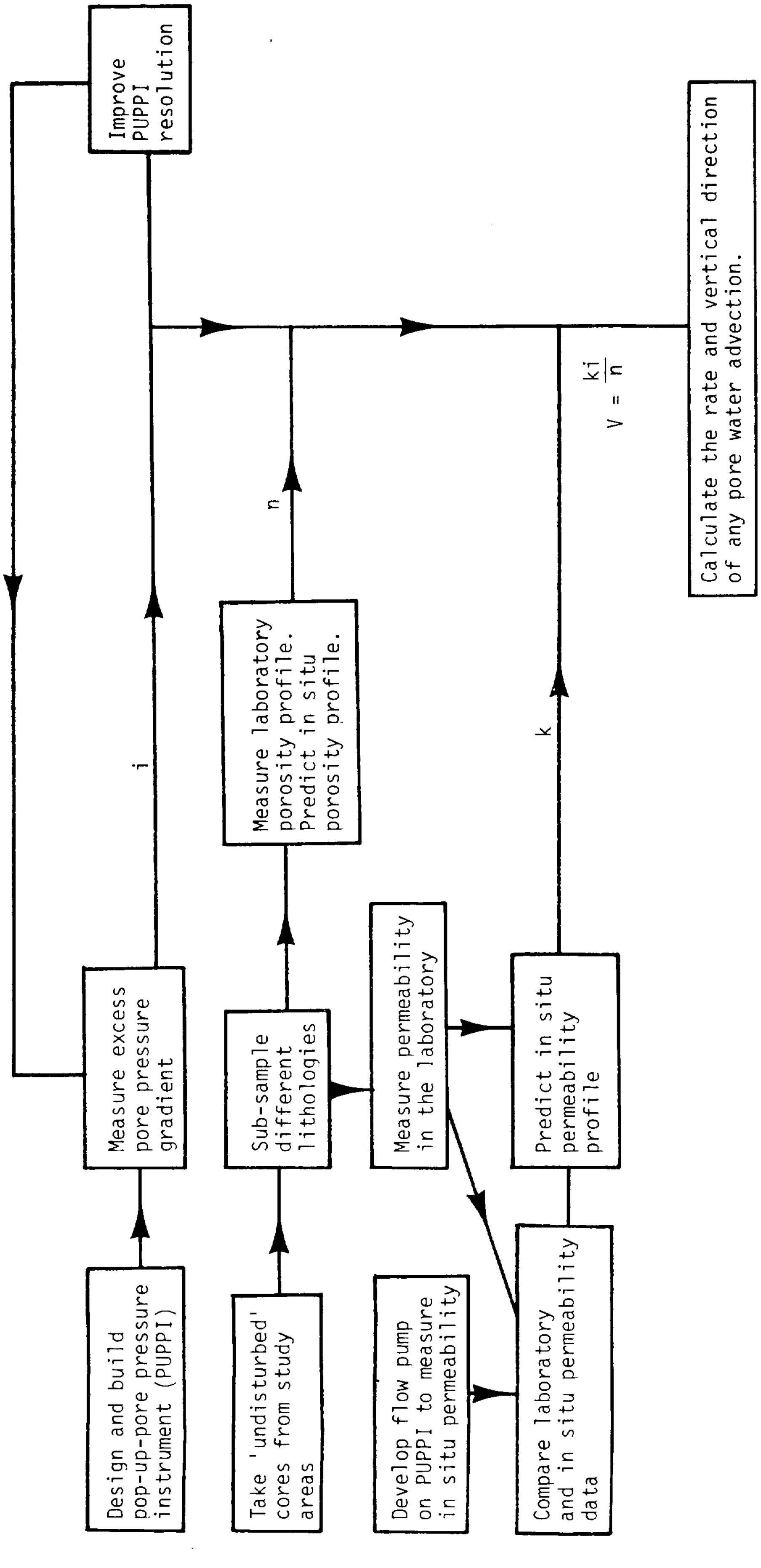

Figure 5.3 Flow chart for the IOS programme of natural pore water flux studies.

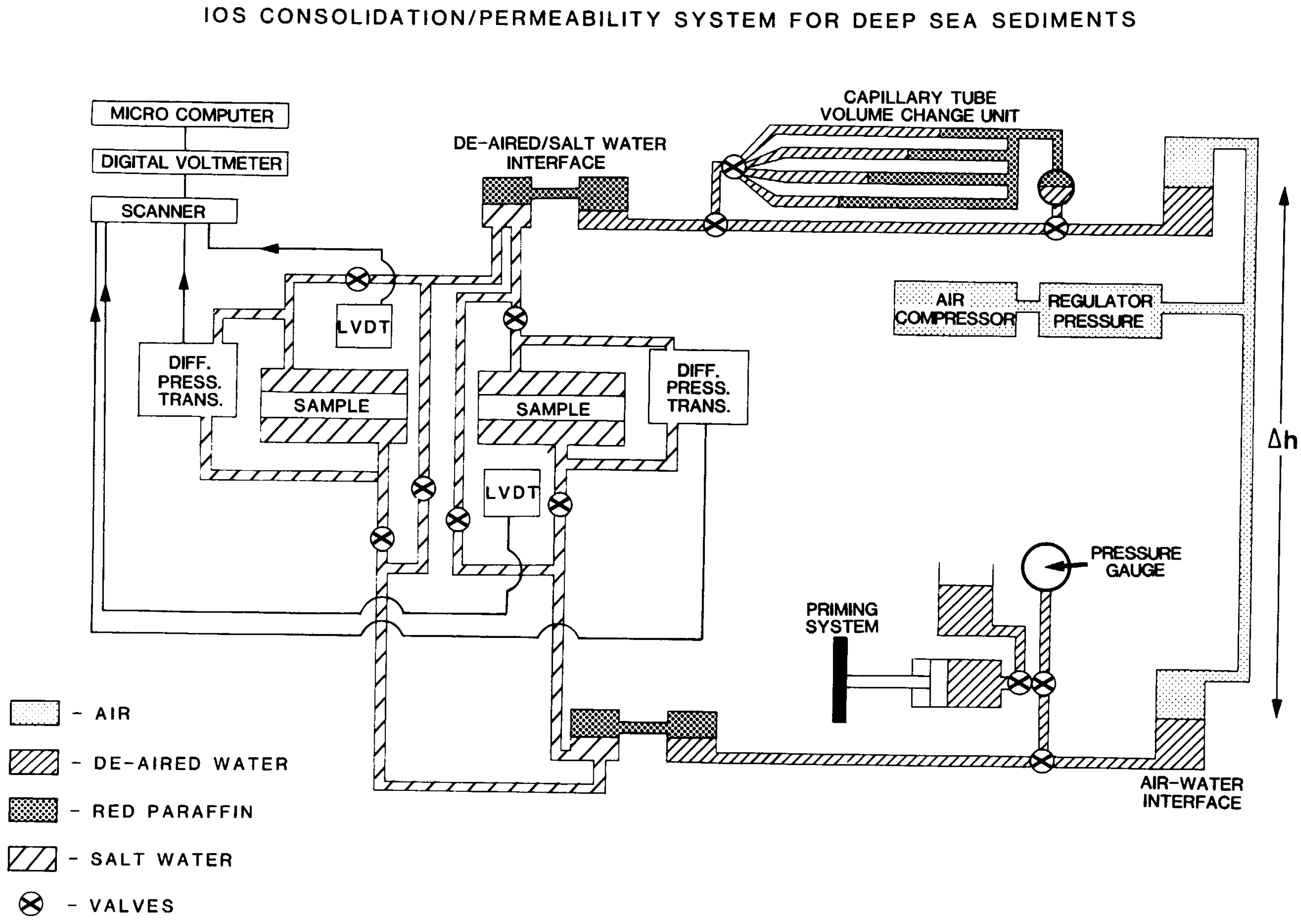

Figure 5.4 Schematic diagram of the IOS consolidation/permeability apparatus.

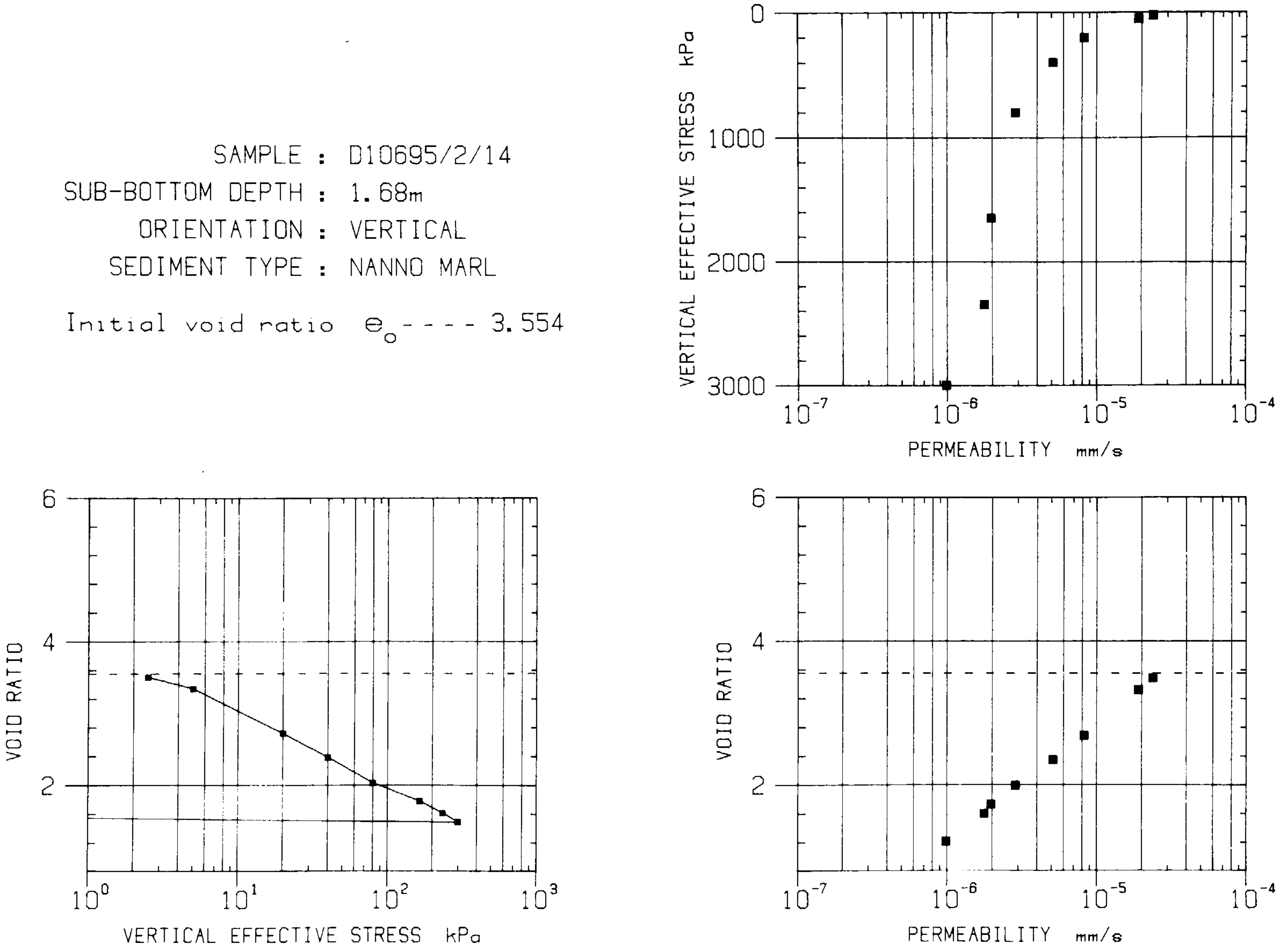

Figure 5.5 Graphical representation of the results of a typical consolidation/permeability test on nanno marl turbidite B(Sample D10695/2/14).

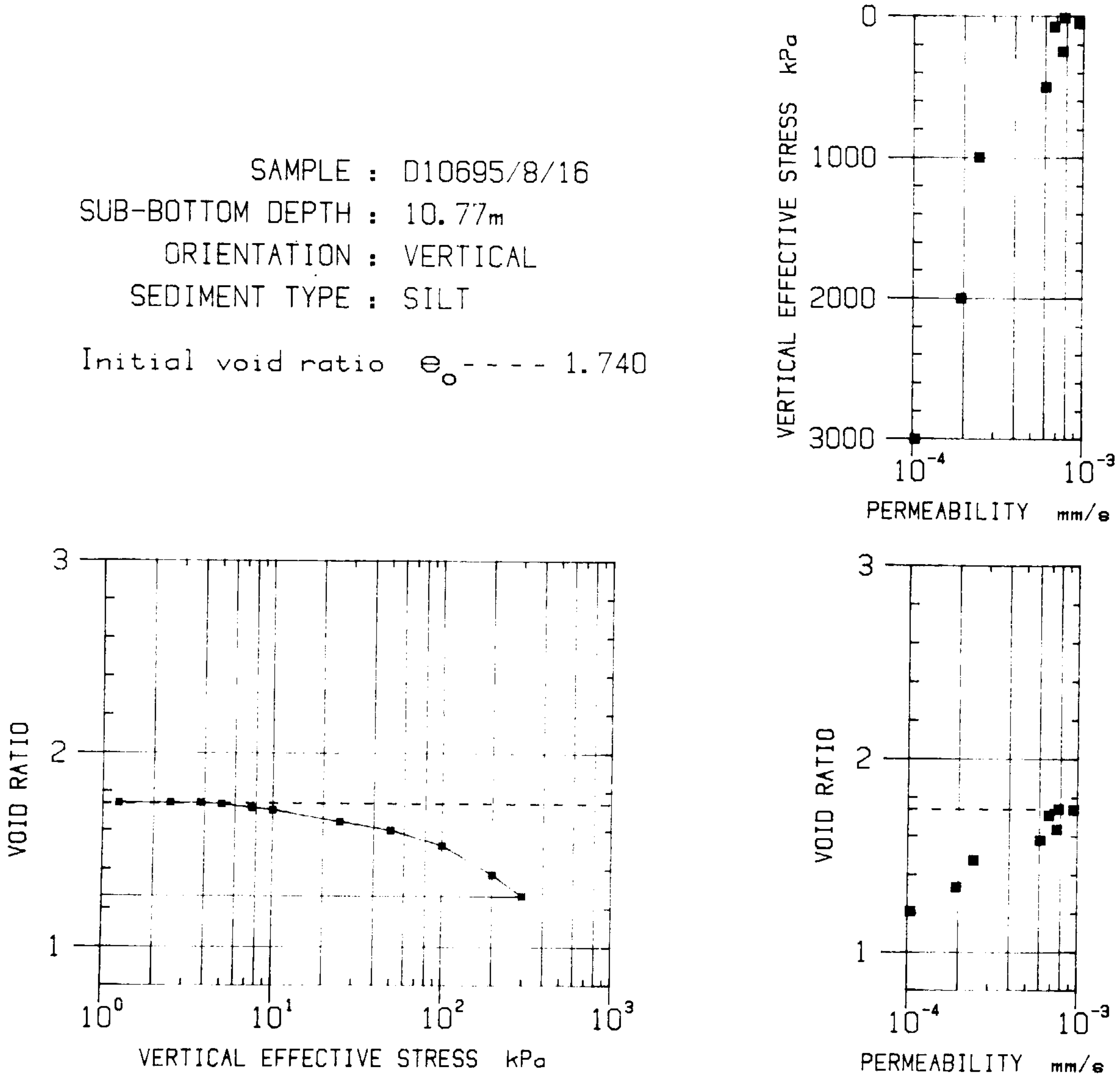

SAMPLE : D10695/8/16
SUB-BOTTOM DEPTH : 10.77m
ORIENTATION : VERTICAL
SEDIMENT TYPE : SILT

Initial void ratio e_o - - - - 1.740

Figure 5.6 Results of consolidation/permeability test on the silty base of turbidite F (Sample D10695/8/16).

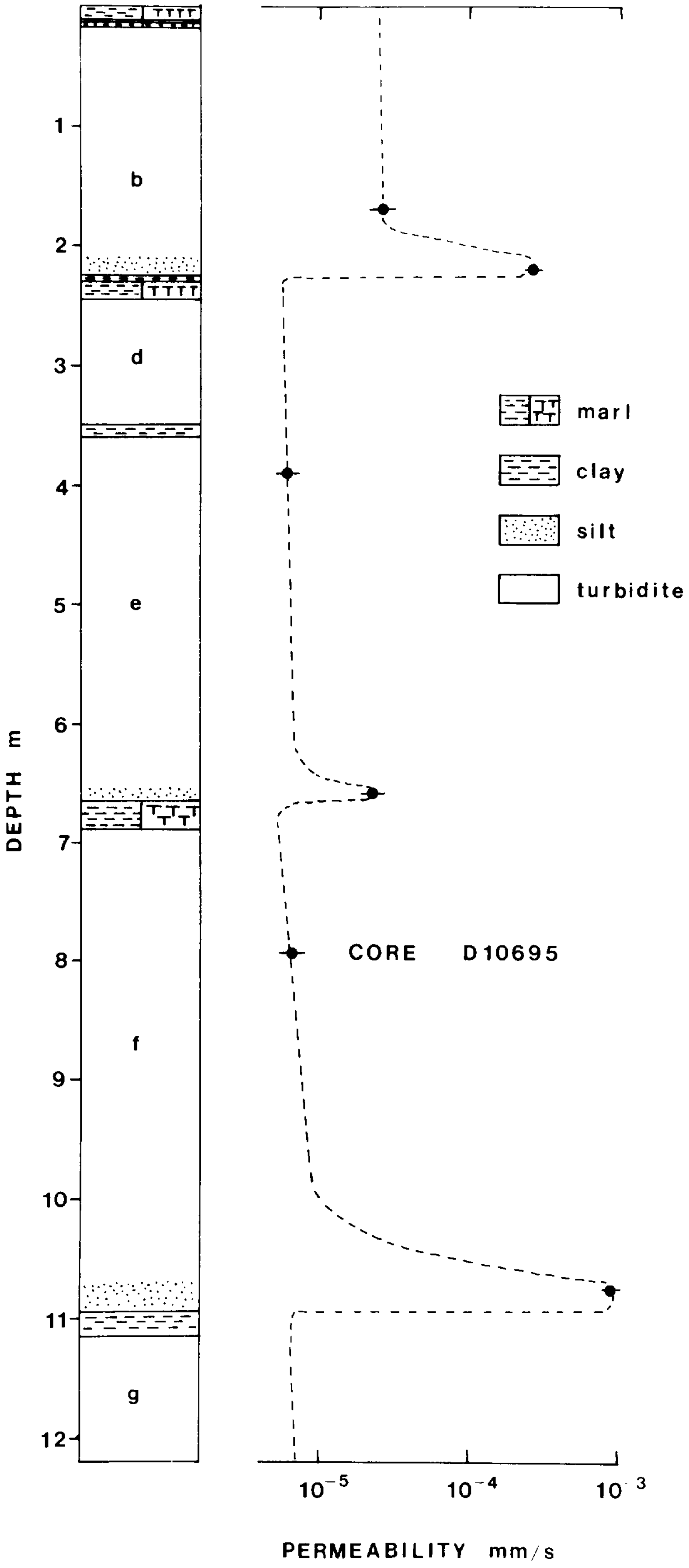

Figure 5.7 Lithology with measured permeability for core D10695.

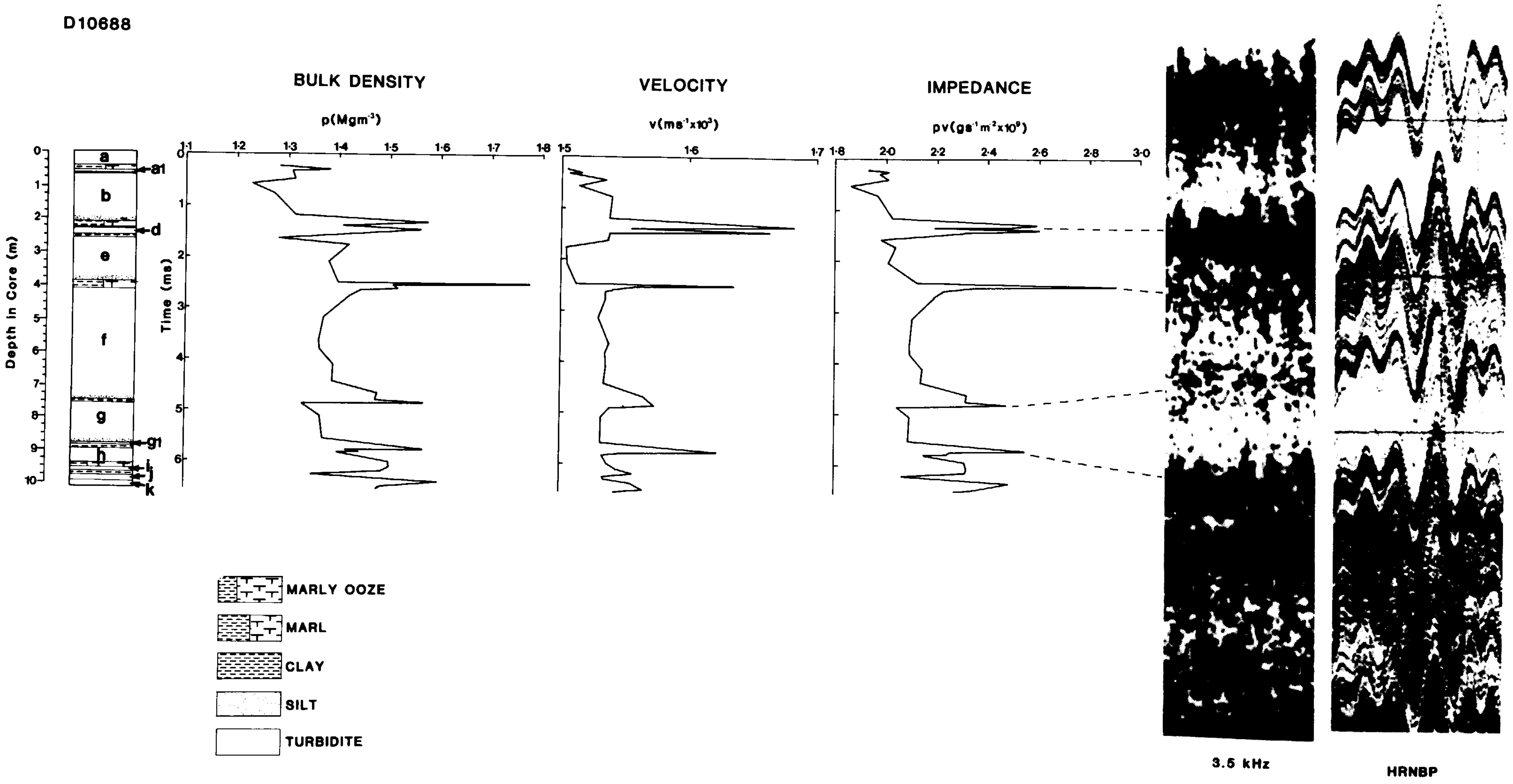

Figure 5.8 Section of 3.5 kHz record and acoustic impedance profile for core D10688. Also shown is the record from the near-bottom profiler which was obtained nearby on Station D10691.

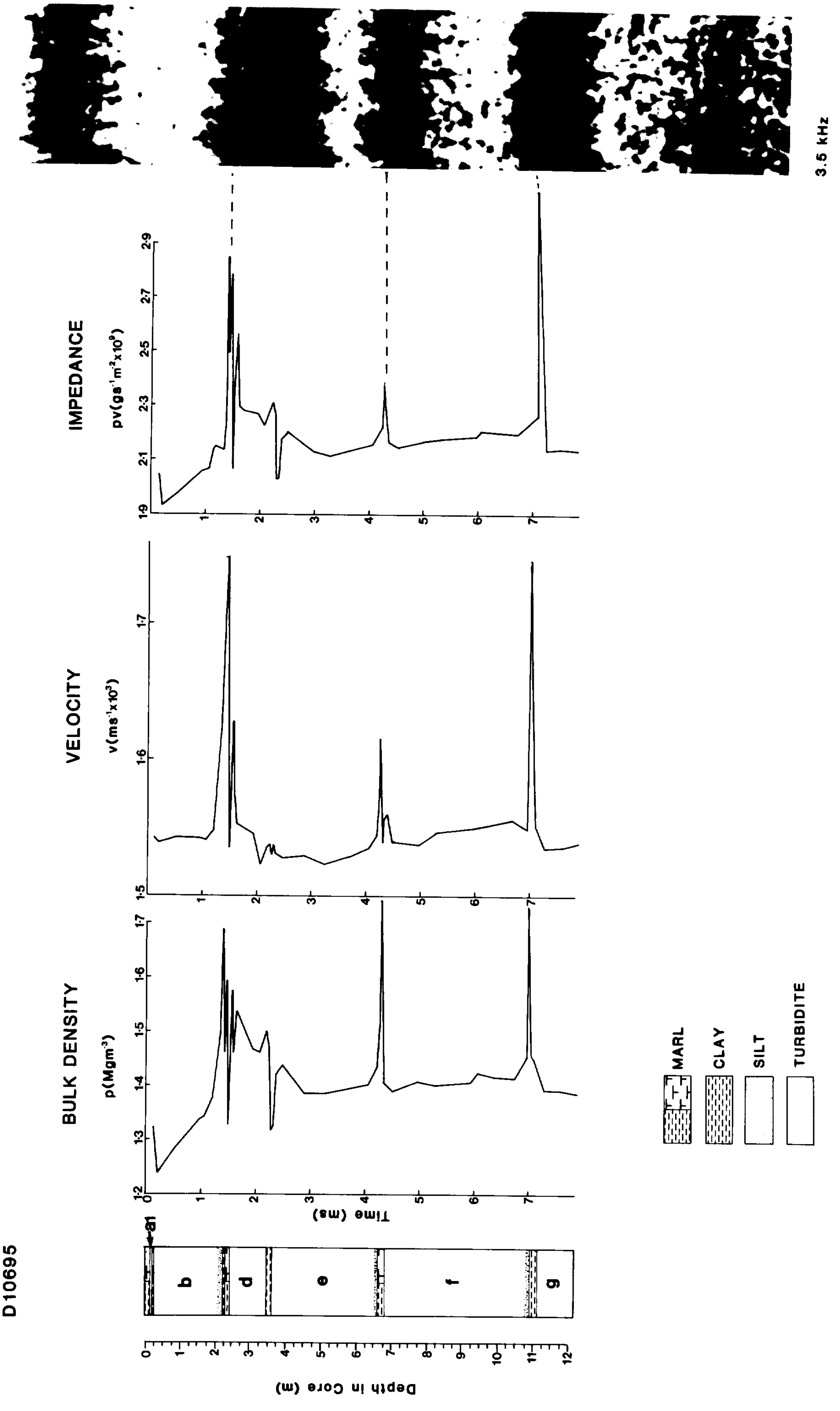

Figure 5.9 3.5 kHz record and acoustic impedance profile for core D10695.

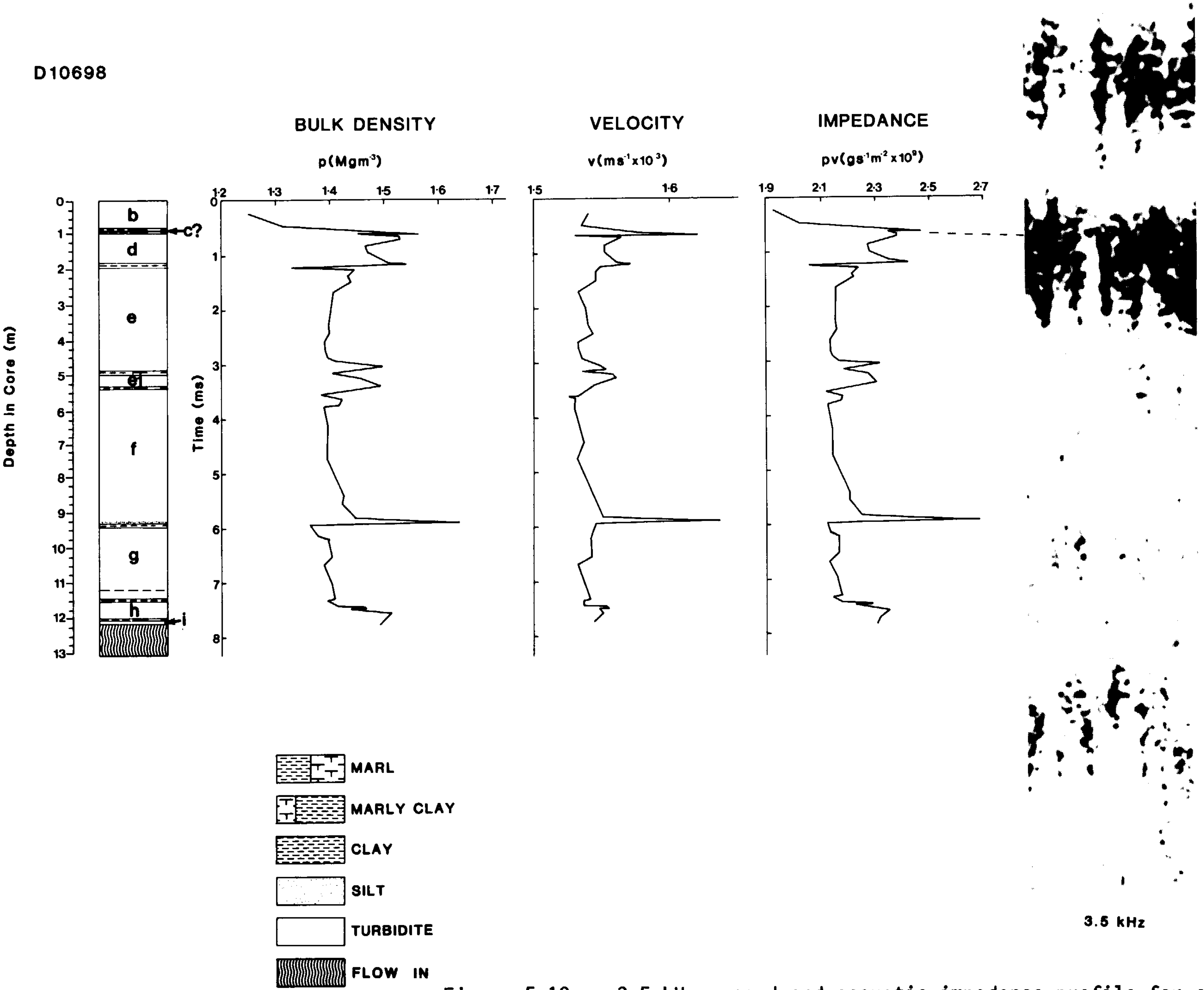

Figure 5.10 3.5 kHz record and acoustic impedance profile for core D10698.

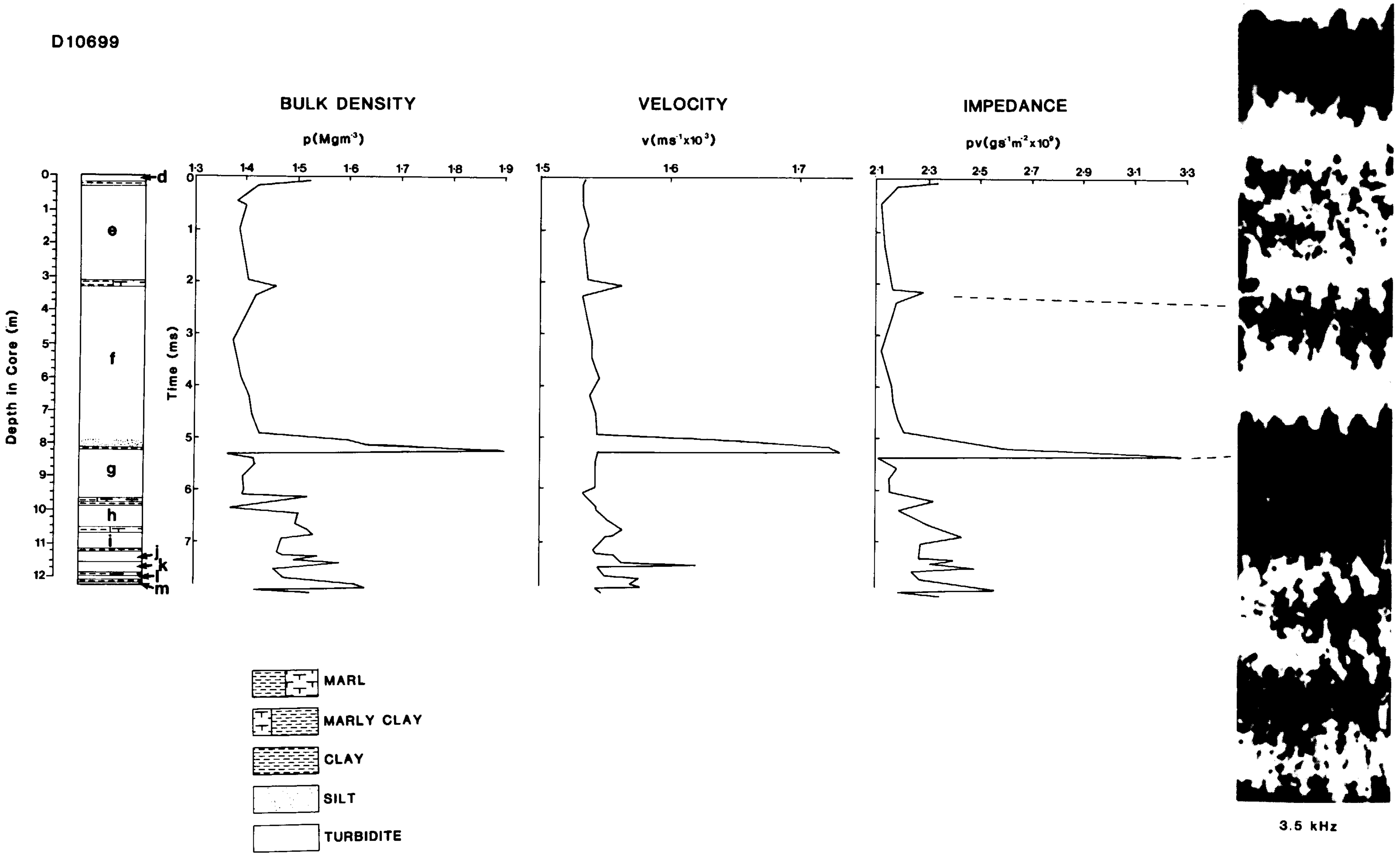

Figure 5.11 3.5 kHz record and acoustic impedance profile for core D10699.

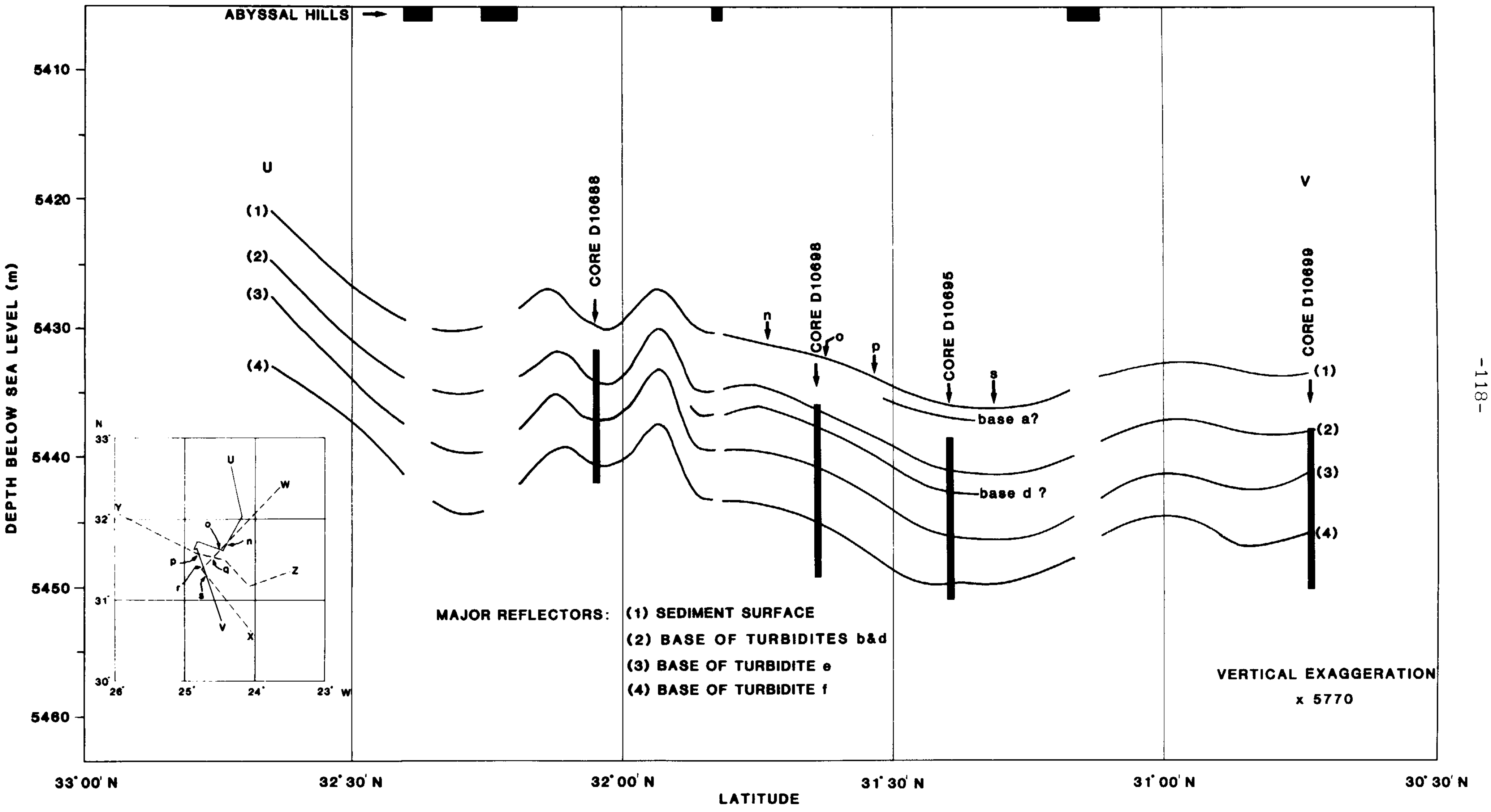

Figure 5.12 N-S transect across GME showing the depth to the base of turbidites B and D, E, and F, based on 3.5 kHz profiles and cores.

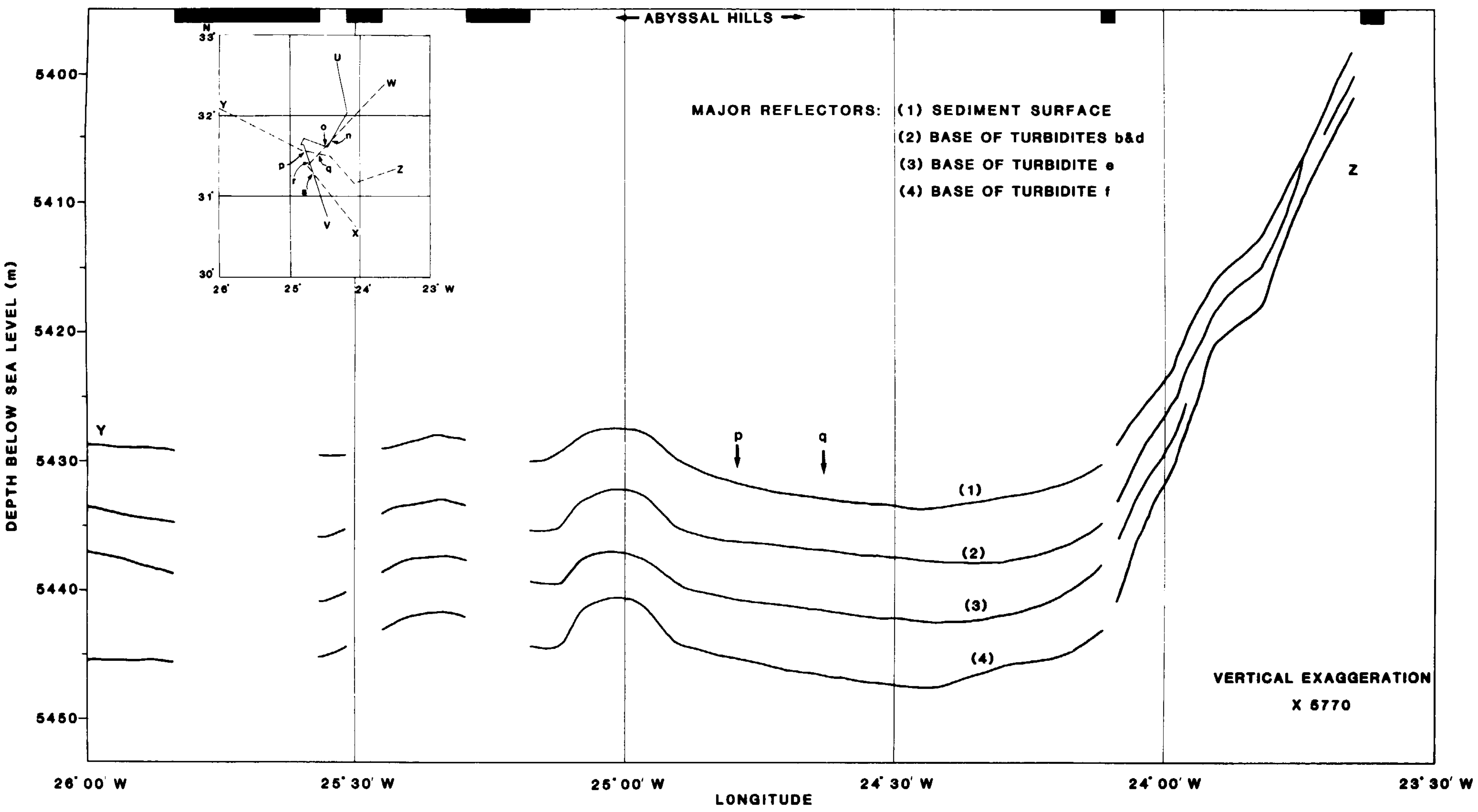

Figure 5.13 W-E transect across GME showing the depth to the base of turbidites B and D, E, and F, based on 3.5 kHz profiles and cores.

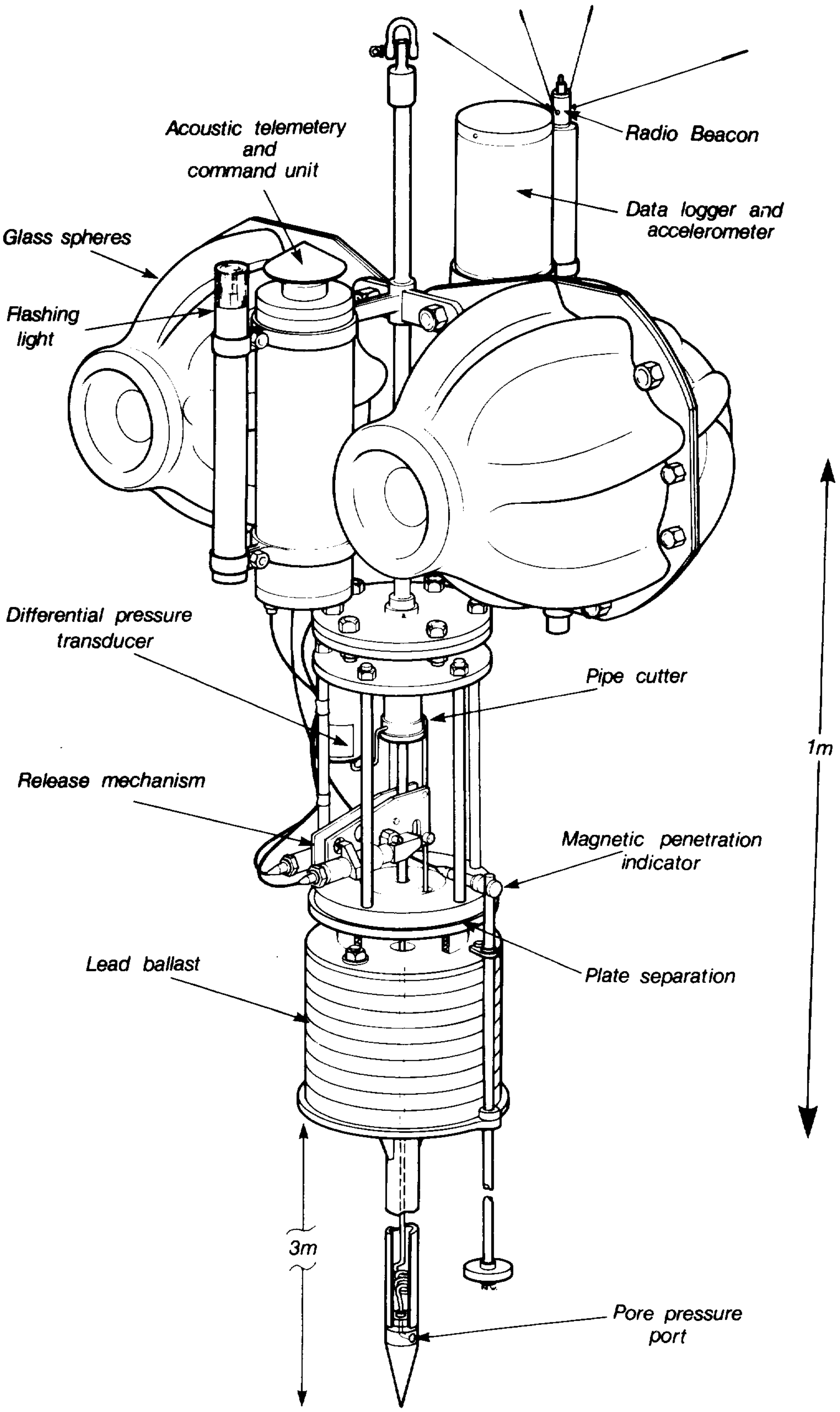

Figure 5.14 Pop-up Pore Pressure Instrument (PUPPI)

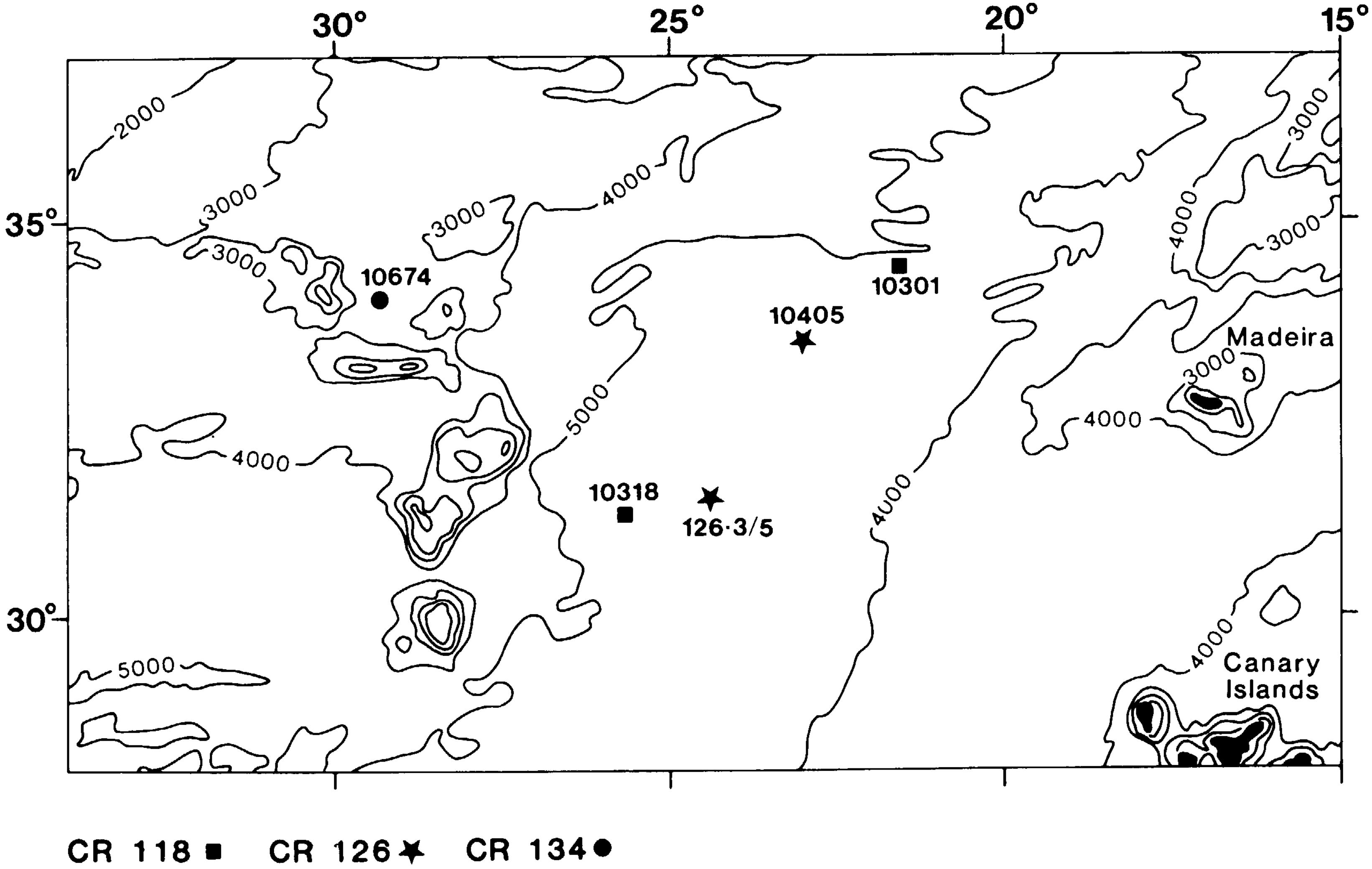

Figure 5.15 Positions of heatflow stations in and near GME.

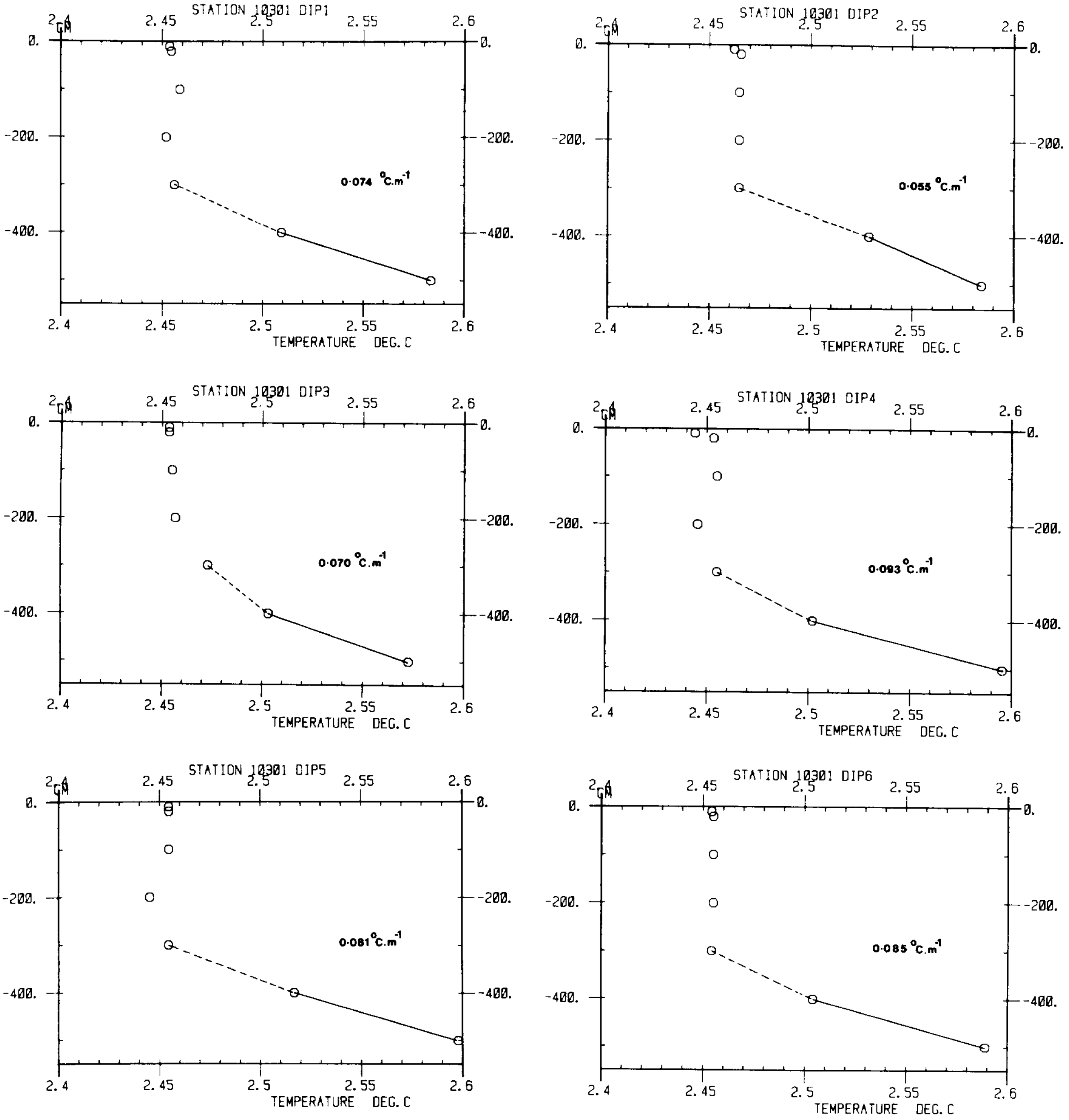

Figure 5.16a Sediment temperature profiles measured at station D10301. It is evident that the probe only penetrated to a depth of 1-2m.

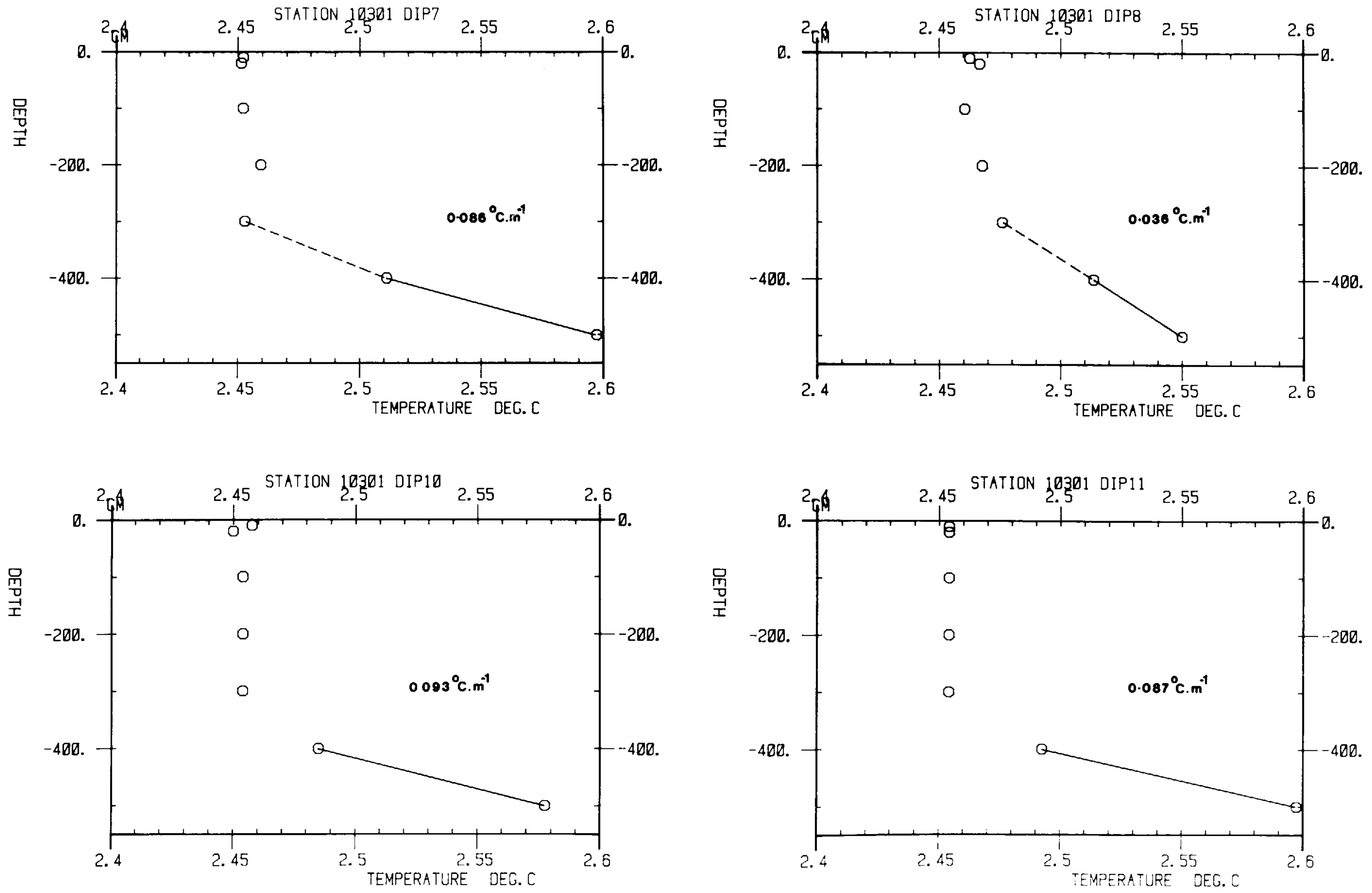

Figure 5.16b Sediment temperature profiles measured at station D10301. It is evident that the probe only penetrated to a depth of 1-2m.

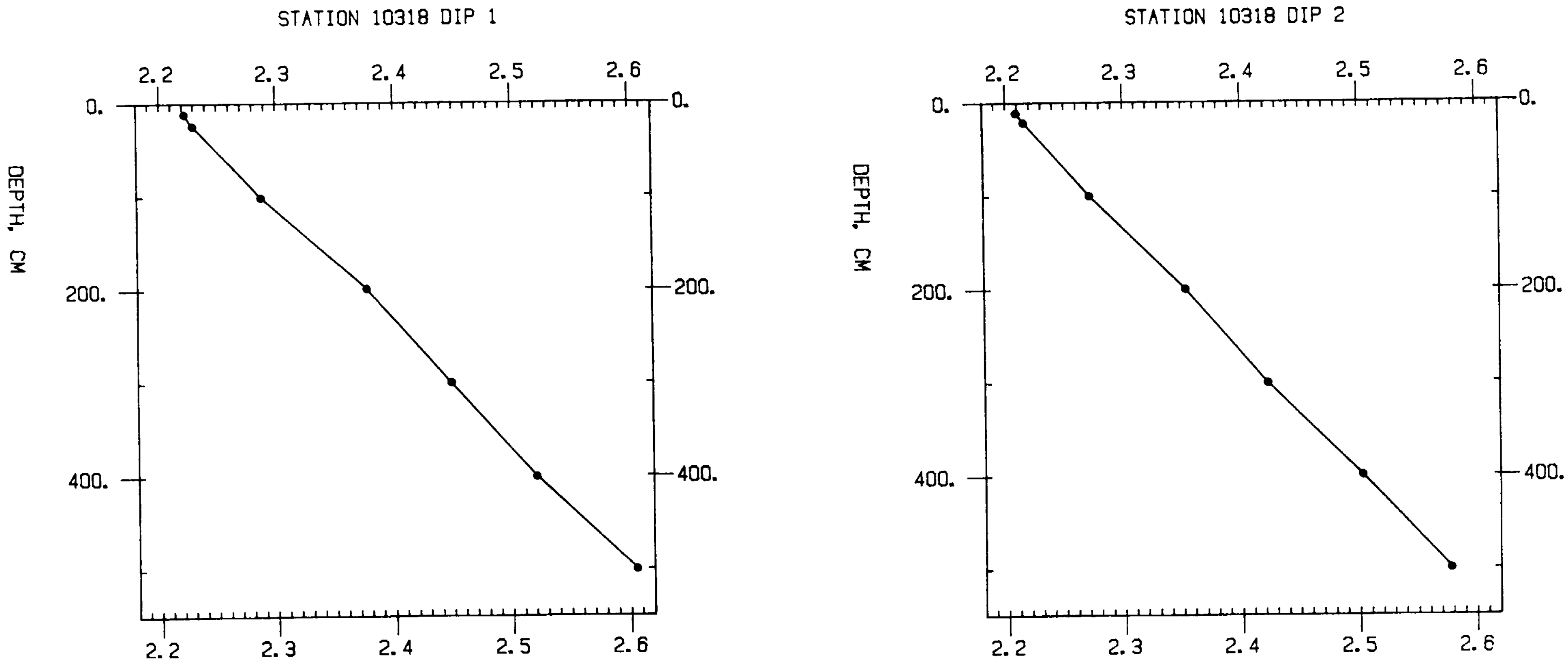

Figure 5.17a Sediment temperature profiles measured at Station D10318.

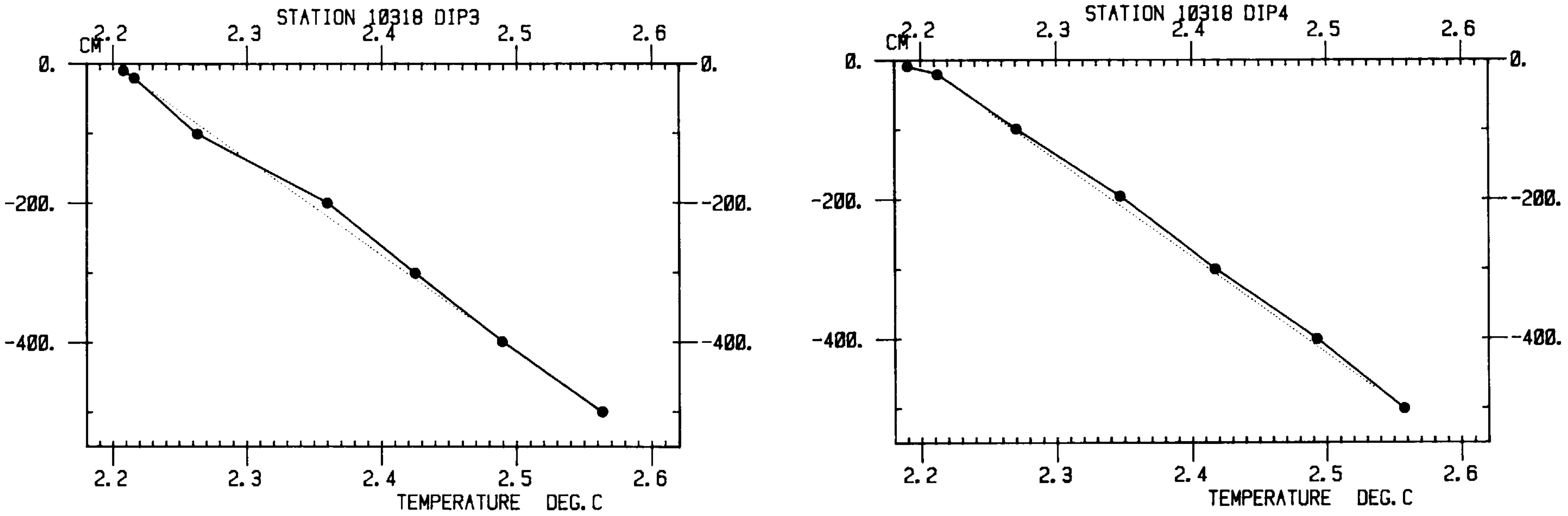

Figure 5.17b Sediment temperature profiles measured at Station D10318.

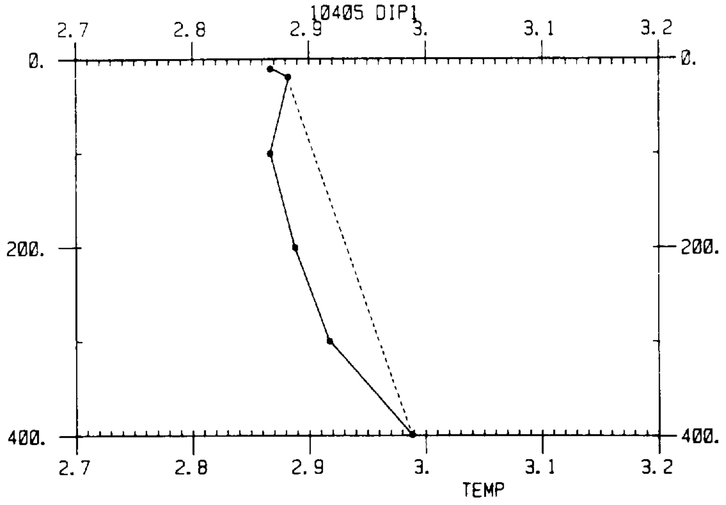

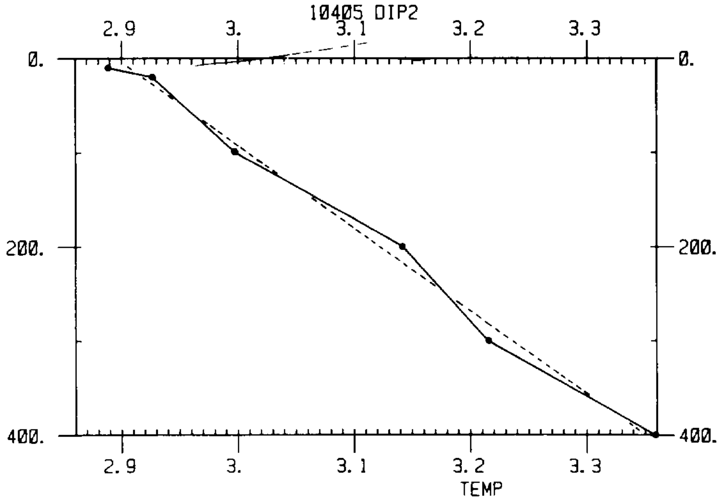

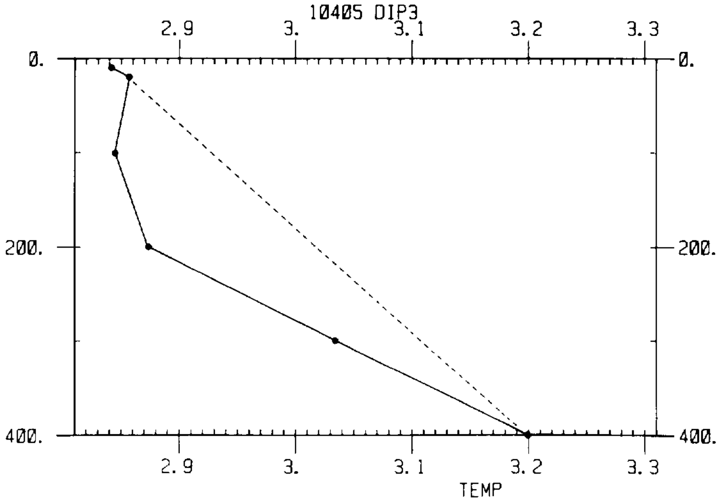

Figure 5.18a Sediment temperature profiles measured at Station D10405.

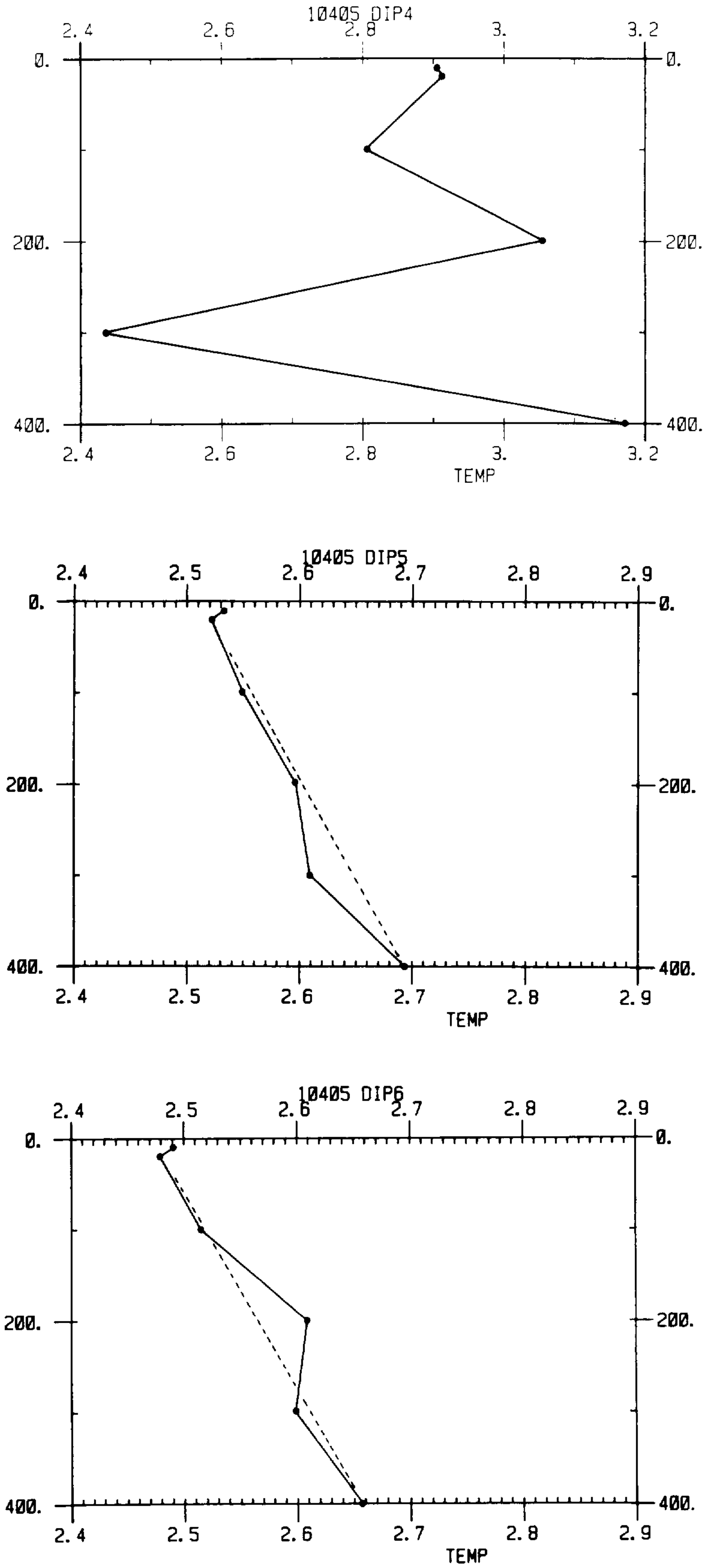

Figure 5.18b Sediment temperature profiles measured at Station D10405.

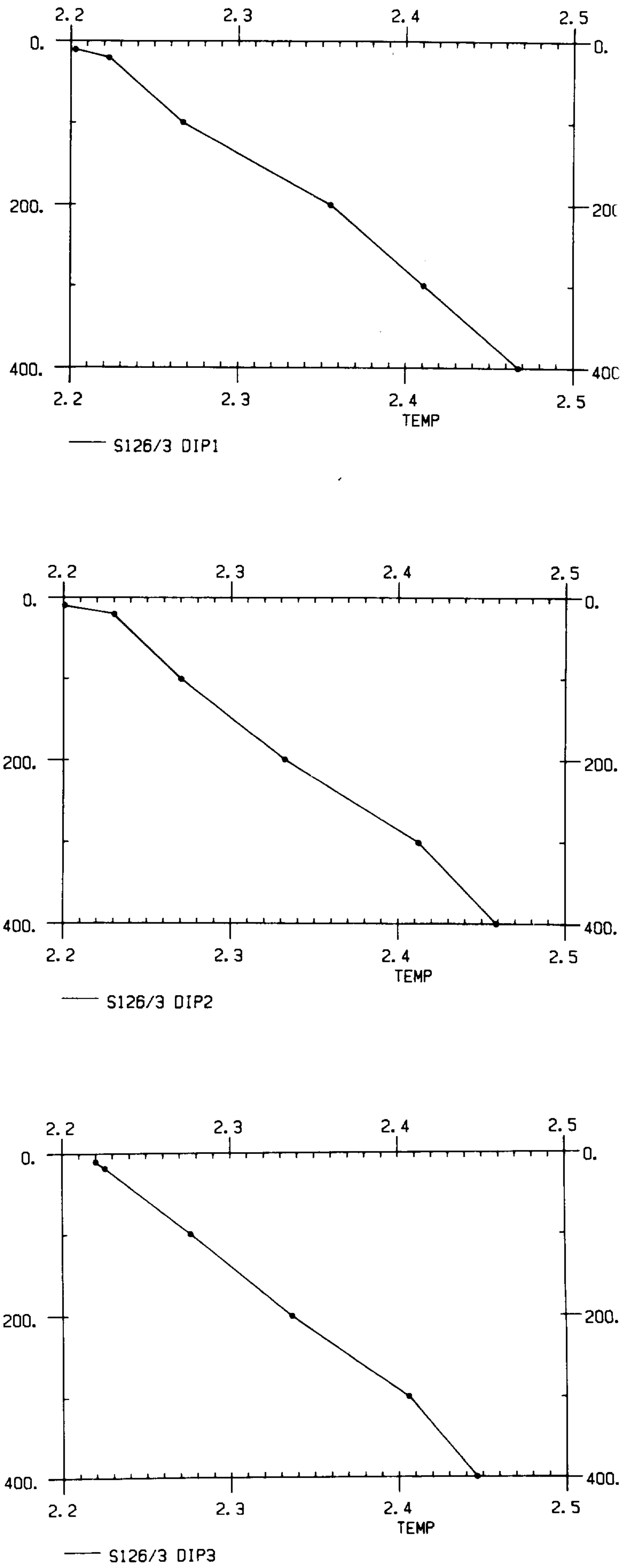

Figure 5.19 Sediment temperature profiles measured at Station S126/3.

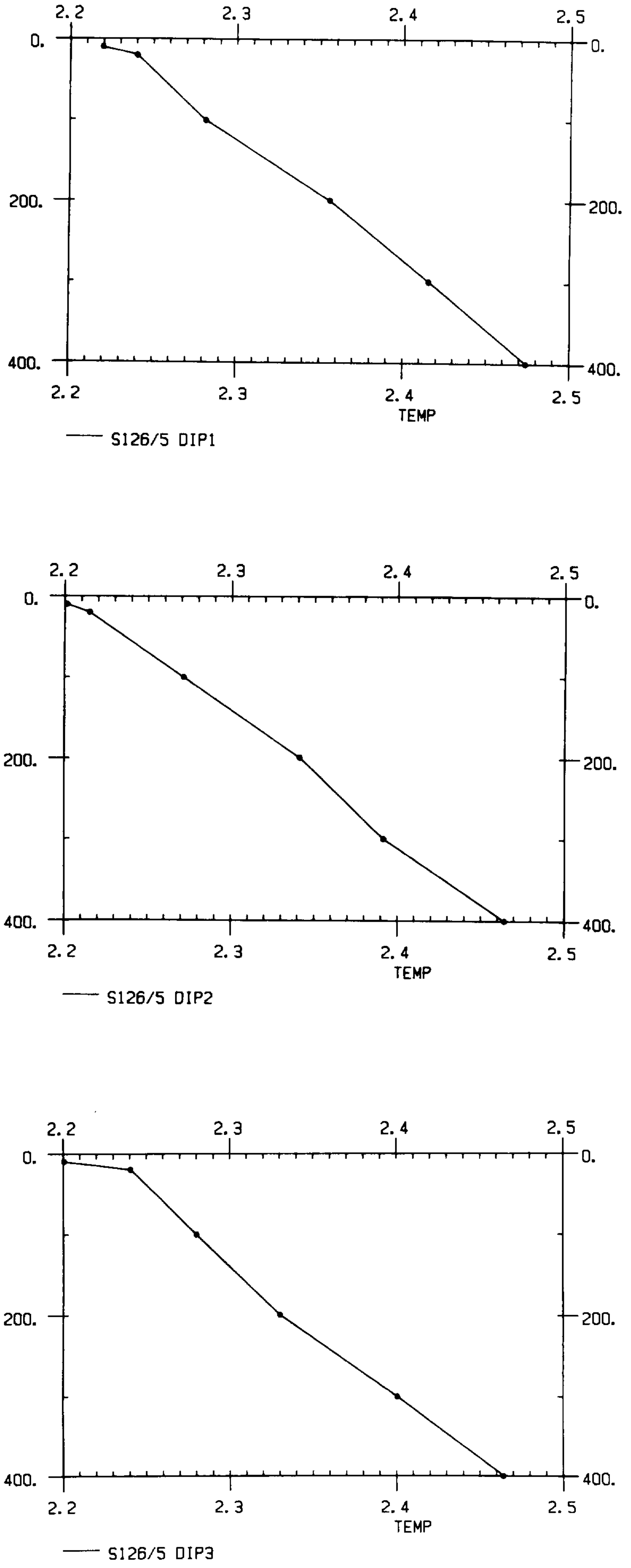

Figure 5.20 Sediment temperature profiles measured at Station S126/5.

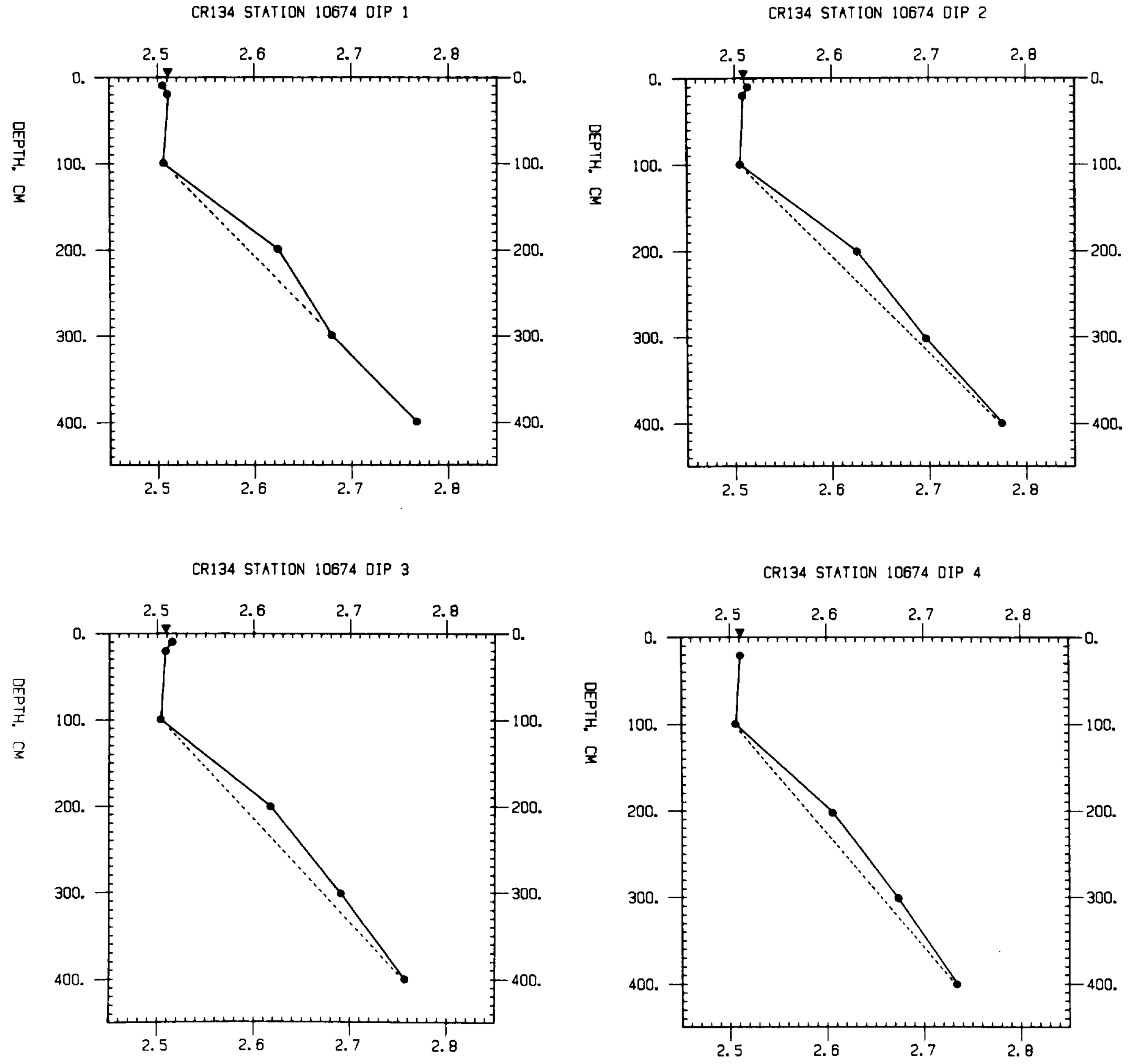

Figure 5.21 Sediment temperature profiles measured at Station D10674.

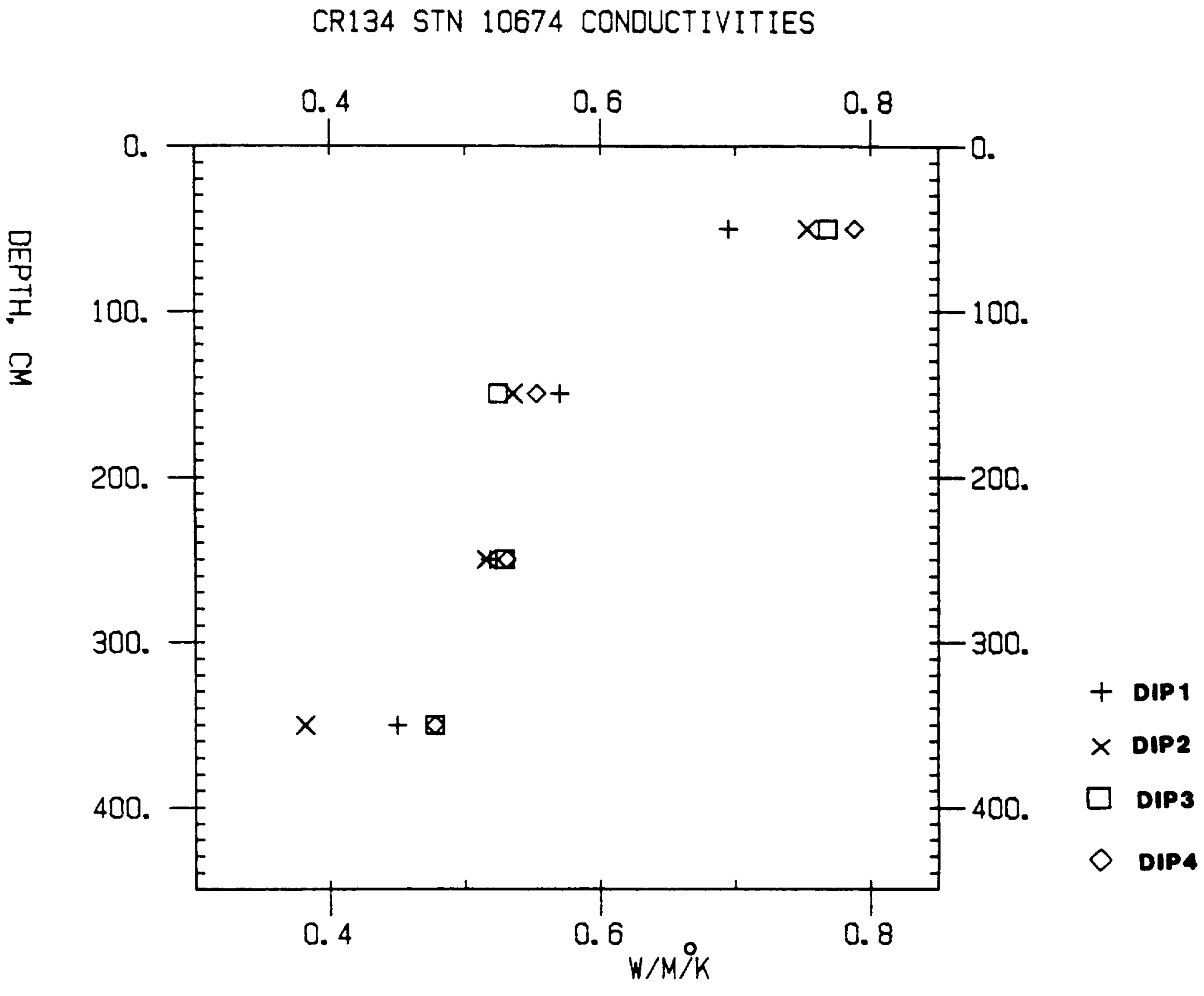

Figure 5.22 Thermal conductivity measurements at Station D10674. (Note: $1 Wm^{-1}K^{-1} \simeq 0.24$ cal $m^{-1}K^{-1}s^{-1}$).

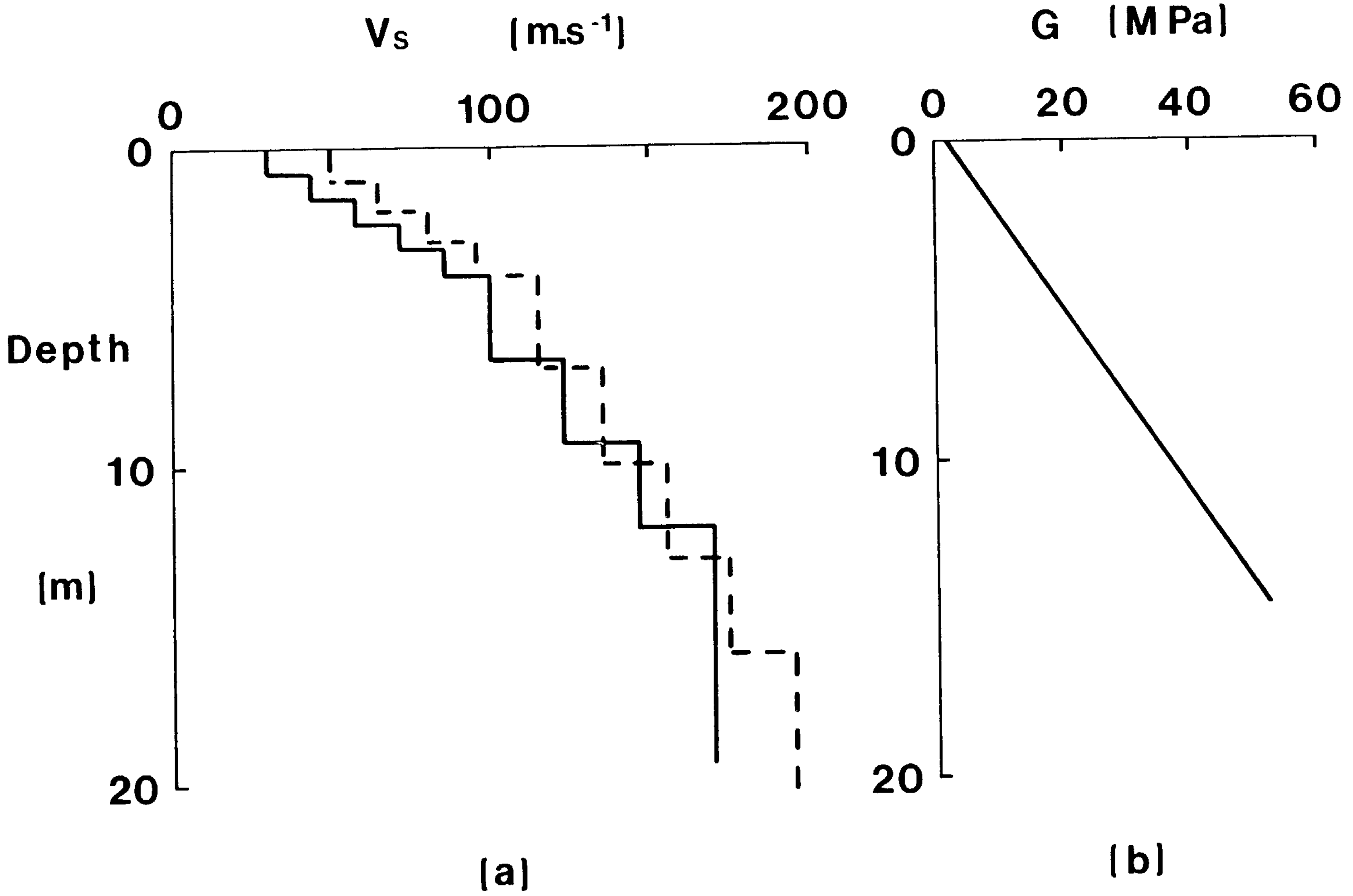

Figure 5.23 Modelled shear-wave velocity (left) and shear modulus to fit the observations of dispersed Scholte waves recorded from a weight-drop experiment at GME (after Whitmarsh & Lilwall, 1982). The two V_S curves shown approximate a bi-linear (dashed line) and a quadratic (solid line) increase with depth.

6. OTHER STUDIES

In this chapter we very briefly review some of the work in the fields of geochemistry, physical oceanography and biology that is relevant to radioactive waste disposal at GME. None of these other studies is entirely independent of the geological ones - for example, ocean currents are influenced by the topography of the seafloor, and in turn influence the erosion or deposition of sediment; the geochemistry of the sediments is intimately bound up with the sediment lithology and depositional processes; and benthic fauna modify the shallow sediments and they or their traces are frequently observed during geological studies.

6.1 Geochemistry

IOS geochemical work to date is summarised by Wilson et al. (1983, 1984). Sediment solid phase and pore water chemistry, Thorium-230 dating and water column particle fluxes have all been studied. Most of the work at GME was carried out in a series of stations near 31°29'N, 24°26'W (all stations designated Discovery 10554). These cores comprise an upper 20 cm of pelagic ooze, a turbidite from 20 to 60 cm containing a marked green layer at its base, pelagic ooze from 60-80 cm, and about 3 m of underlying turbidite (Fig. 6.1). These are the A and B turbidites of section 4.3.

Oxygen measurements show that the oxygen content falls to zero at 30 cm, corresponding to the green band which is relatively high in organic material (1.6% organic carbon - Wilson et al., 1984). Below this there are low but non-zero values for oxygen, suggesting that either the pore-water system is not in equilibrium or that there is horizontal movement of oxygen. Nitrate is reduced almost simultaneously with oxygen, and manganese is mobilised as the soluble Mn II ion at 45 cm (Fig. 6.2). This migrates upwards and is precipitated in the higher oxygen environment at 30-40 cm. The highly sorptive solid manganese hydroxide cannot exist below about 40 cm. It is also inferred that the sharp upper boundary of the green layer, which occurs within an otherwise homogeneous turbidite, marks a downward-moving oxidation front (Wilson et al., 1984). Oxidation of organic carbon appears to take place in a restricted band near the colour change boundary. The abyssal plain sediments at GME are thus much more reduced (with negative Eh) than those at the pelagic CV2 area, where a significant oxygen content persists to 10 m depth. This greater level of reduction is attributed to the higher supply of organic detritus at GME delivered by the terrigenous turbidites. Kuijpers (1982) and Duin & Kuijpers

(1983) have also reported organic carbon peaks of 1.0 to 1.5% associated with the turbidites at GME, with one isolated value of 3.0%. Morris et al. (1984) agree with these observations, but suggest that the changes reflect chemical oxidation of organic carbon and not the effect of molecular oxygen or varying redox potential, because fatty acids have not been strongly affected.

The greater level of reduction at GME, together with the time-varying organic input, render the chemistry there more complicated. Moreover, local variations in chemistry have been found between cores spaced only a few kilometres apart. In addition to the broad green band, thinner blue-black bands occur within the turbidites (Kuijpers, 1982; Duin & Kuijpers, 1983; Morris et al., 1984). Morris et al. show that these bands are enriched in Cu, Ni, V and Zn, and suggest that they too represent migration fronts caused by post-depositional remobilisation. They suggest that the enriched metals come not only from the organic material being deposited within the turbidites, but also from the oxic pelagic ooze.

Experiments on ion exchange capacity of the GME sediments suggest that this is low compared with coastal sediments, on the order of 10 to 30 meq. per 100 g (Wilson et al., 1983). It is even lower where the sediment contains a higher proportion of coarser grained calcite material.

6.2 Physical Oceanography

No physical oceanographic results from within the GME area have yet been reported, although current-meter moorings have been emplaced there during the time of writing this report. The nearest observations to GME are from arrays of current meters, thermometers and dispersed floats near 33°N, 22°W, on the lower continental rise or proximal Madeira Abyssal Plain (Saunders, 1983a, b). The seabed topography is similar to that at GME, with a nearly flat plain at about 5300 m interrupted by occasional, isolated abyssal hills, except that the Mid-Atlantic Ridge flank is further away at 100 to 200 km west of the area. The current meter array was 40 km across and contained seven moorings, all with instruments at 10 m and 100 m above the seafloor and some with additional meters at intermediate depths or at 600 m above the seafloor (Saunders, 1983b). Measurements over periods of about 200 days have been analysed. A tripod containing a current meter and a camera was deployed on the seabed for 60 days (Elliot & Thorpe, 1983). CTD profiles were also made from the surface.

The bottom water is very poorly stratified, making the benthic boundary layer very hard to detect. However, study of very small (a few millidegrees C) temperature differences suggests that it is between 23 and 120 m thick (Saunders, 1983b). High-resolution temperature measurements have also revealed the passage of benthic fronts up to at least 30 km long, with an estimated frequency of several per year (Elliot & Thorpe, 1983). The fronts are inclined and are believed to be capable of transporting material rapidly across the benthic boundary layer. The peak current observed near the bottom was 7.5 cm s^{-1}, but no sediment movement was detected on time-lapse photographs of the seabed.

Observed tidal currents had a maximum (M_2 component) of about 3.5 cm s^{-1}, which is adequately predicted by existing theory. Inertial currents with a period of 22 hours and wavelength of 100 km had an amplitude of 1-2 cm s^{-1}, and the residual low frequency currents, represented by eddies less than 35 km across with dominant periods of 50-100 days, had no net velocity, but a kinetic energy of 3.6 km^2 s^{-2} at 10 m and 1.6 cm^2 s^{-2} at 600 m above bottom. Knowing the eddy size it was possible to map the flow near the top of the benthic boundary layer (Fig. 6.3); a mean westward drift of the eddies of 1 cm s^{-1} was found (Saunders, 1983a).

The current meter measurements and float observations were also used to estimate dispersion (Fig. 6.4) (Saunders, 1983a). Tidal and inertial currents would transport tracer from a maintained point source via bands 500-1000 m wide, but dispersion within these bands cannot be estimated from the current measurements available. From the study of the 10 m flow maps and of clusters of floats, it was estimated that the squared separation of two points doubles, and the concentration of a tracer would approximately halve, in about 15 days, for initial separations in the range 1 to 20 km. Dispersion at larger than eddy scales (100 km) depends on the ocean diffusivity, which was found to be 1-2 x 10^6 cm^2 s^{-1} within the bottom 100 m and half that at 600 m. diffusivity of 10^6 cm^2 s^{-1} would disperse a cloud 100 km in diameter to half its initial concentration after about 60 days.

6.3 Marine Biology

No primary site specific studies have yet been made in or near GME, but a few biological observations have occurred as by-products of our geological studies. We have already discussed bioturbation (section 4.7), and here we report on some preliminary estimates of the density of benthos based on photographs taken with the WASP survey camera. A total area of approximately 10 hectares (25 acres) was covered.

Figure 6.5 shows meandering trails of holothuroidea, small spoke burrows the star-like features) made by echiurid worms, and a (rat-tail?) fish. Figure 6.6 is also from GME, and shows a giant spoke burrow over 4 m across, as well as several smaller ones. This high level of biological activity is fairly typical of GME, and we attribute this to the relatively high levels of organic carbon available in the turbidites. By contrast, the King's Trough Flank area, although shallower, contains much less activity and, in particular, is almost devoid of spoke-burrows (Table 6.1).

TABLE 6.1 - WASP camera observations of benthic biology (preliminary results).

AREA 1. PELAGIC CLAYS (26°N)		Count:	No/km^2
16,568 m^2 covered			
Pelagic holuthurians		8	483
Benthic holothurians		0	0
Spoke burrows:	L	0	0
	M	0	0
	S	0	0
AREA 2 PELAGIC OOZES (KTF area)			
79,657 m^2 covered			
Pelagic holothurians		18	226
Benthic holothurians		67	841
Spoke burrows:	L	0	0
	M	5	63
	S	0	0
AREA 3. TURBIDITES (GME area)			
90,749 m^2 covered			
Pelagic holothurians		59	650
Benthic holothurians		35	386
Spoke burrows:	L	3	33
	M	41	452
	S	2,221	24,474

Spoke burrows:
L = Burrows larger than 1.8 m.
M = Burrows 0.7-1.8 m.
S = Burrows smaller than 0.7 m.

FIGURE CAPTIONS

Figure 6.1 Summary lithology and solid phase manganese content at Station D10554. (After Wilson *et al.*, 1983.)

Figure 6.2 Pore-water composition of sediments at Station D10554. Arrows indicate composition of bottom water. (After Wilson *et al.*, 1983.)

Figure 6.3 Stream function maps of the flow calculated 10 m above the Madeira Abyssal Plain at 10-day intervals. Solid arrows show observed currents at 10 m, dashed lines at 600 m. Contours in m s^{-1}. Dot-dashed line is where prediction error equals half the variance. (After Saunders, 1983a.)

Figure 6.4 Comparison between observed tracks of two groups of four floats (solid) and trajectories calculated from Eulerian current measurements. Circles are a measure of the dispersion of the floats. Tracks are marked in days and hours. (After Saunders, 1983a.)

Figure 6.5 Survey camera photograph from station D10678; 31°24'N, 24°35'W, at GME. Area of frame is 9.0 x 6.4 m; height above bottom 9.9 m; water depth 5422 m.

Figure 6.6 Survey camera photograph of giant spoke-burrow (echiurid worm lebenspuren) at GME. Station S126/6; 31°10'N, 23°48'W; water depth 5433 m; height above bottom, 13 m; frame size, 12.0 x 8.6 m (sketch of car is to scale).

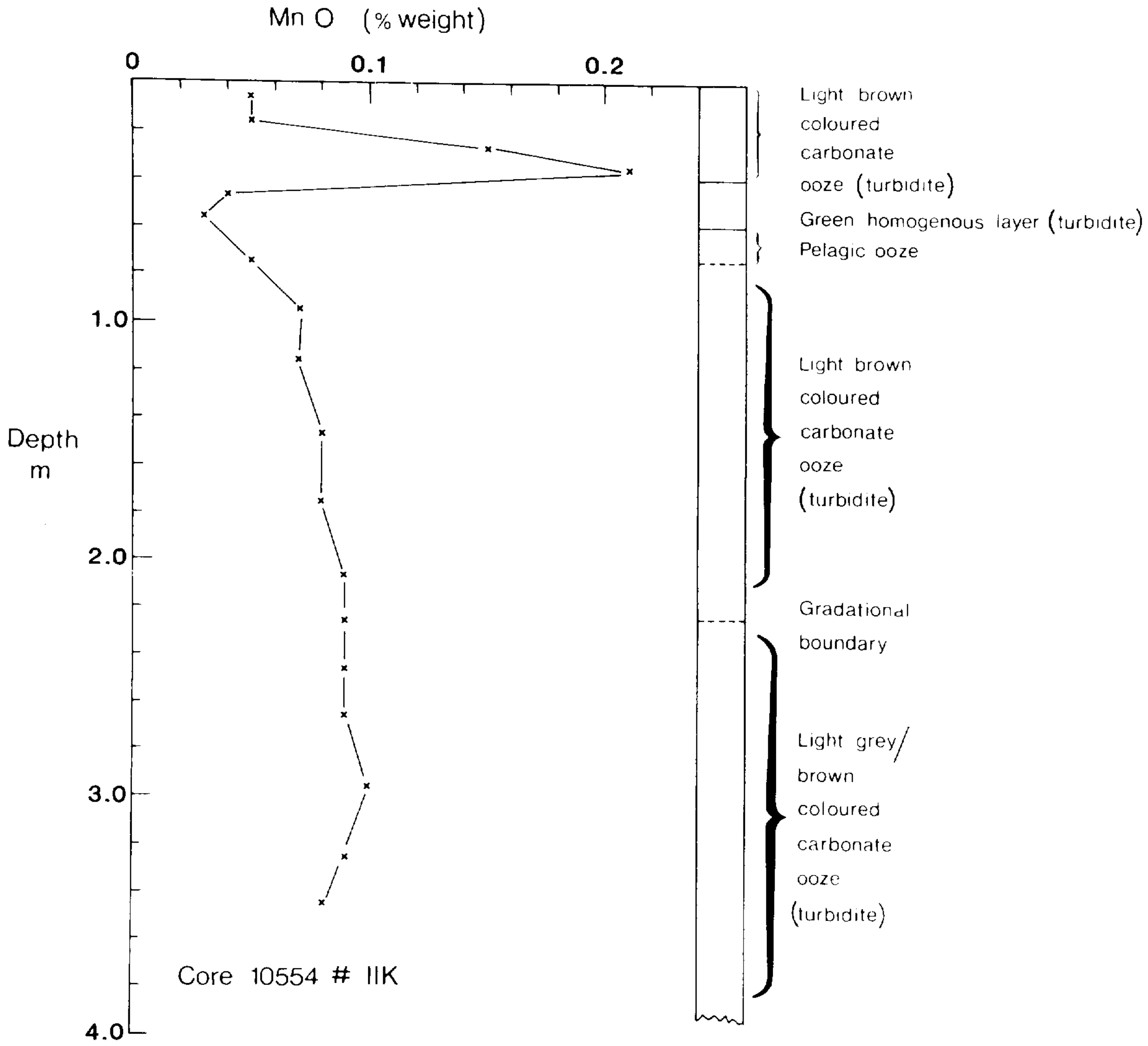

Figure 6.1 Summary lithology and solid phase manganese content at Station D10554. (After Wilson *et al.*, 1983.)

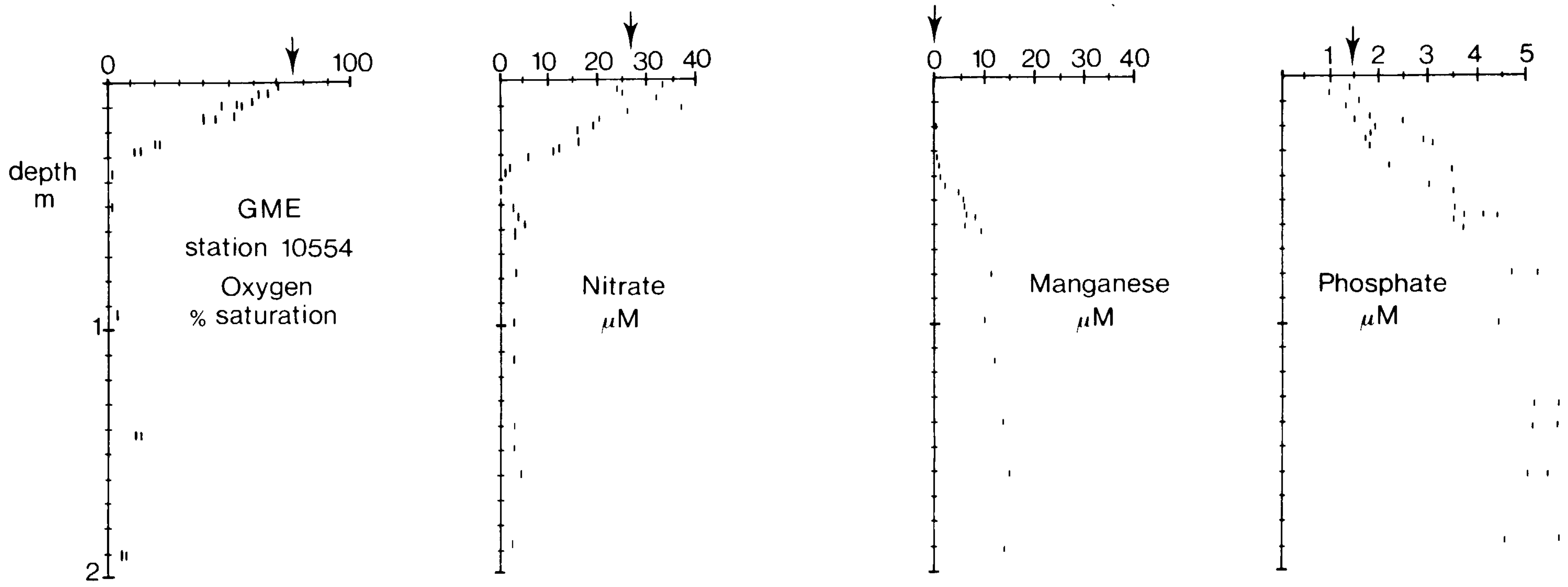

<u>Figure 6.2</u> Pore-water composition of sediments at Station D10554. Arrows indicate composition of bottom water. (After Wilson <u>et al</u>., 1983.)

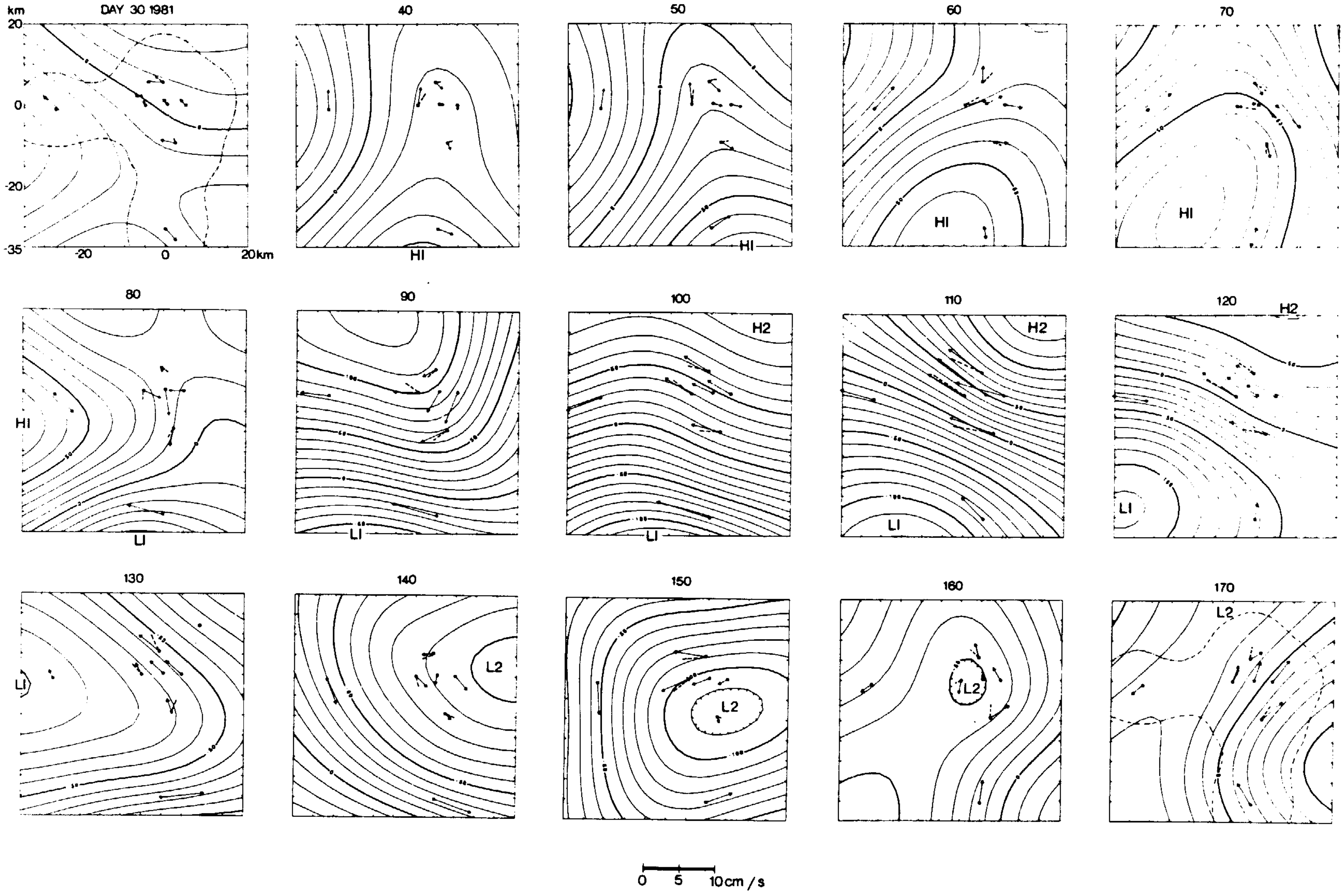

Figure 6.3 Stream function maps of the flow calculated 10 m above the Madeira Abyssal Plain at 10-day intervals. Solid arrows show observed currents at 10 m, dashed lines at 600 m. Contours in m s^{-1}. Dot-dashed line is where prediction error equals half the variance. (After Saunders, 1983a.)

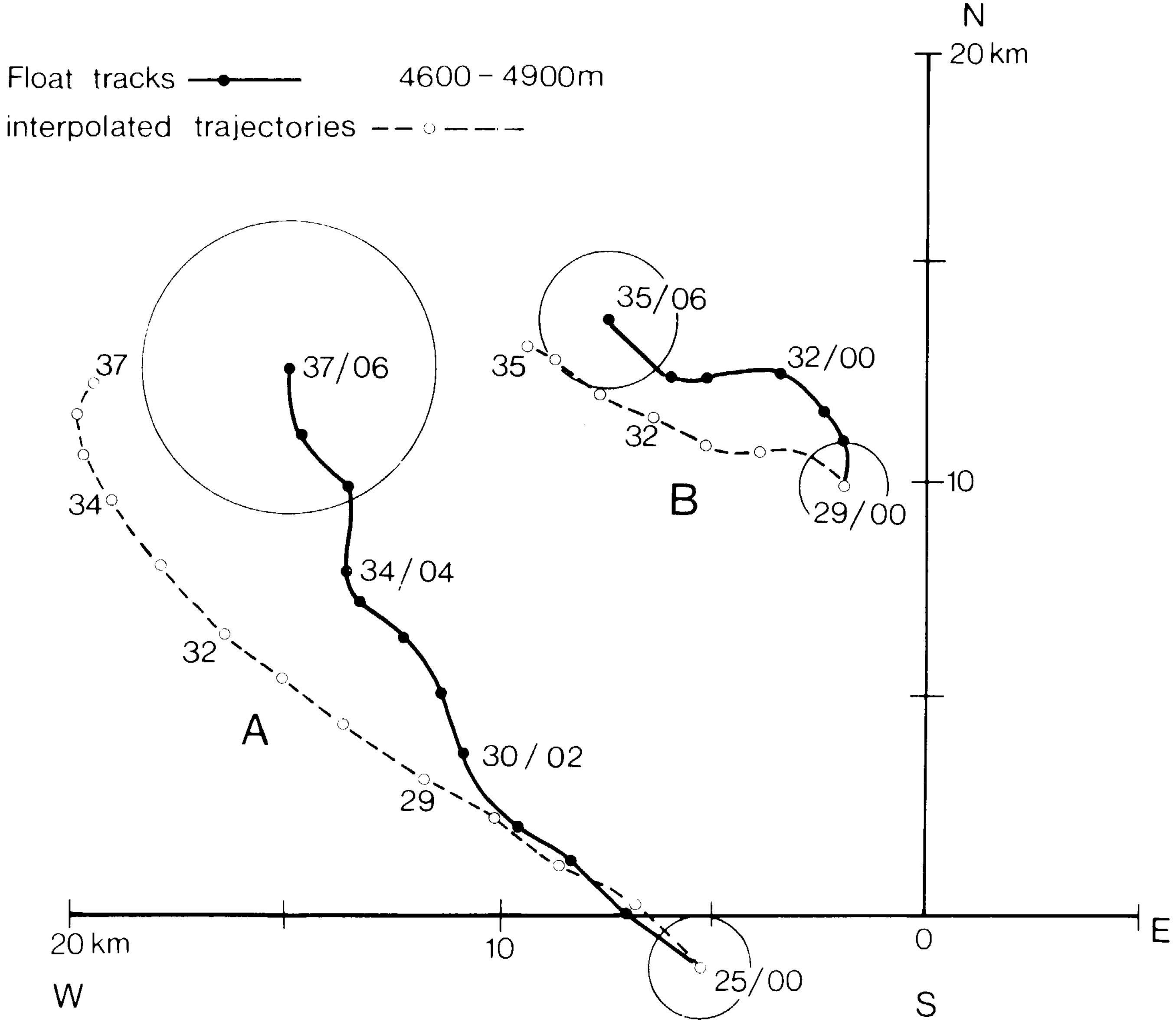

Figure 6.4 Comparison between observed tracks of two groups of four floats (solid) and trajectories calculated from Eulerian current measurements. Circles are a measure of the dispersion of the floats. Tracks are marked in days and hours. (After Saunders, 1983a.)

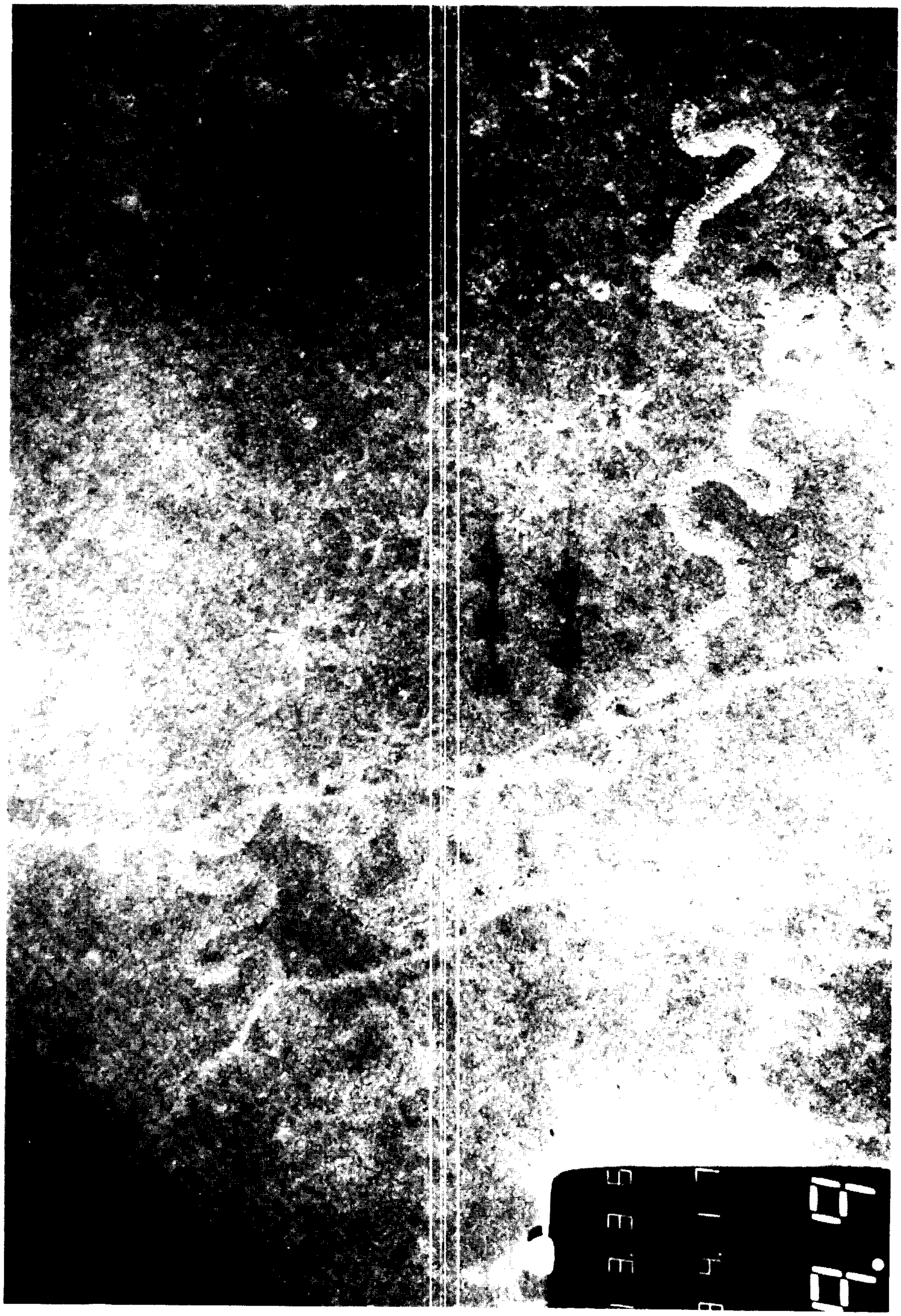

Figure 6.5 Survey camera photograph from station D10678; 31°24'N, 24°35'W, at GME. Area of frame is 9.0 x 6.4 m; height above bottom 9.9 m; water depth 5422 m.

Figure 6.6 Survey camera photograph of giant spoke-burrow (echiurid worm lebenspuren) at GME. Station S126/6; 31°10'N, 23°48'W; water depth 5433 m; height above bottom, 13 m; frame size, 12.0 x 8.6 m (sketch of car is to scale).

7. SUMMARY, DISCUSSION, CONCLUSIONS AND RECOMMENDATIONS

In this final chapter, we first summarise and discuss the results from GME in relation to the site selection guidelines developed by Searle (1979, 1984), and then conclude with recommendations for further work.

7.1 Summary and discussion

We deal with our results item by item under the headings of the individual guidelines, restricting ourselves to those guidelines that deal with the "Desirable characteristics of the geological barrier".

A1. "The site should avoid areas near steep slopes where sediments may be unstable."

A2. "It should avoid areas of recent erosion, dissolution or mass movement of sediment."

The abyssal plain at GME is completely flat and therefore stable. Sediments on the adjacent continental rise and slope have been shown to be unstable, and to move downslope into the GME area. These movements appear to occur preferentially at the boundaries between glacial and interglacial climatic regimes, and it is likely that such changes will recur within the next 10^4 to 10^5 years. The last episode of mass movement resulted in some erosion, accompanied by deposition of sand-sized material, east of 24°W; west of 24°W it produced fine-grained turbidites. We have no evidence of serious erosion west of 24°W in the cored interval (up to 22 m depth; approximately 190,000 years), although there may have been slight erosion (~ 10 cm?) of the Stage 2 pelagic unit at one or two places. There is no evidence on the seismic sections of erosion at greater depths, but such erosion would not necessarily show on these records. We have no direct evidence of sediment slumping off abyssal hills onto the plain, but it probably does occur locally especially where seafloor slopes are steep. Today the abyssal plain lies above the CCD but within the lysocline, and as a result there is moderate, but not complete, dissolution of sediment in the water column. During glacial intervals the area lies below the CCD and calcareous sediments suffer complete dissolution in the water column. However, there is no evidence of significant removal of material once it has been incorporated into the sediment column.

A3. "The site should avoid areas of recent tectonic activity."

The area is situated within the African lithospheric plate and is 500 km from the nearest tectonically active plate boundary. We have no evidence of tectonic activity nearer than this, with the possible exception of the apparent faults seen on the seismic records at GME. Present evidence suggests that they do not reach closer than about 17 m to the surface but this needs further investigation. We think at present that the features are growth faults related to differential compaction of the sediment, in which case the uppermost, soft layers are probably not disrupted, but this has not yet been established. However, other possible origins must be investigated. Even if the faults are not associated with tectonic activity, it is possible that they provide paths for the escape of water released from the sediments (see under A8).

A4. "The site should avoid areas of recent volcanic activity."

The nearest active volcanism is in the island of Sao Miguel in the Azores and in the adjacent Azores spreading centre, over 500 km away. However, the island of Madeira, 500 km east of GME, has been volcanically active during the last million years. The Madeira and Canary archipelagos, together with the Great Meteor Seamount group, all represent examples of predominantly Neogene to Quaternary intra-plate volcanism. Although it is difficult to quantify exactly, we estimate very roughly that the probability of a new volcano erupting in a 30 km square area during the next 100,000 years is approximately 1 in 10^5.

A5. "The site should be in a region of low seismic activity."

The probability of occurrence of an earthquake of body wave magnitude $m_b > 4.5$ per square kilometre per year has been estimated at about 1 in 10^7 at GME, and the return period for peak accelerations in excess of 0.1 g is between 2000 and 10,000 years. This level of seismicity is slightly lower than that in the land area of Great Britain.

A6. "The site should have adequate sediment thickness."

Approximately 80% of the GME area has sediments in excess of 250 m thick. Unsedimented areas account for no more than about 2% of the area.

A7. "The disposal medium should be laterally homogeneous."

Under the abyssal plain west of 24°W (about 80% of the GME area) the sediments show a high degree of lateral uniformity. Individual turbidites in the uppermost 20-50 m can be traced for 100 km or more across the plain, though thin ones (less than 10-20 cm thick) may be drastically thinned or absent in places. Lithology and physical properties vary slowly and evenly across the area. However, there is one, possibly serious, exception to this, and that is that the sedimentary layers may be disrupted by faults in some places. The apparent faulting appears to be concentrated in areas where the sediments, especially the turbidites, are thickest. An area 30-50 km across centred near 31.25°N, 25.35°W appears to be free of them, but this needs further investigation.

A8. "The disposal medium should have low pore-water convection and low permeability."

Geothermal gradients in the GME abyssal plain are linear within the resolution of the instrument, implying that porewater advection is less than about 0.5 m y^{-1}. Heatflow values are also normal. No results are yet available from the abyssal hills, where advection might be concentrated, nor have direct measurements of pore-water advection been made. Apart from pore-water advection driven by thermal convection, water released during the compaction of sediments must also migrate to the surface. If the sediments are faulted (see A3) then the faults may provide pathways for enhanced pore-water flow. This possibility needs investigation.

Measured permeabilities are in the range 10 to 150 x 10^{-6} mm s^{-1} (mean about 30 x 10^{-6} mm s^{-1}) for the turbiditic nannofossil marls that make up about 90% of the sediment, around 10^{-3} mm s^{-1} for the silty bases of the turbidites (5% of the total) and in the range 3 to 40 x 10^{-6} mm s^{-1} for the calcareous pelagic clay that makes up the remaining 5%. It is possible that these values may be increased significantly (perhaps by orders of magnitude for the fine-grained material) in places by the presence of open burrows, and both the density of such burrows and in-situ measurements of permeability therefore need careful study.

A9. "The disposal medium should provide low diffusivity for the waste ions."

We have no information on diffusion coefficients.

A10. "The disposal medium should have high specific adsorptivity."

We have no information on sorption coefficients.

A11. "The disposal medium should have a large active grain surface area (and therefore small grain size)."

Median grain size ranges from about 2 μm for the pelagic clays through 3μ for the marls to 200 μ for the sands of some turbidite bases, though west of about 24.5°W less than 10% of the material in the turbidite bases is sand (> 62.5 μm).

A12. "The disposal medium should have a low organic carbon content to minimise ion mobility."

Organic carbon content ranges from less than 0.2% in the pelagic clays to about 1.5% (and locally occasionally 3%) in the turbidites. These are relatively high values, and there is evidence for some ion mobility. These effects need to be carefully assessed.

A13. "The disposal medium should be strong enough to resist massive thermal convection."

Shear strengths are around 2 kPa at the surface, increasing to perhaps 35-50 kPa at 30 m. Detailed modelling will be required to show whether this is acceptable.

A14. "A sufficient thickness of the medium should have high plasticity to promote self-healing."

We have no information on this parameter.

A15. "The medium should contain no natural gases or gas hydrates."

There is no evidence of such products at GME.

A16. "The site should be relatively free of obstructions on the seafloor."

The incidence of glacial erratics and other boulders at GME is low compared with areas farther north in the Atlantic. It is estimated that the cumulative risk of impact of a point penetrator with erratics greater than 1.5 cm diameter in the uppermost 12.5 m of the turbidites is about 0.015%.

A17. "The thermal conductivity of the disposal medium should be high enough to ensure acceptable in-situ temperatures."

No in-situ conductivity measurements have been made in GME or neighbouring abyssal plain sediments, but we estimate values of about

0.85 ± 0.1 Wm^{-1} K^{-1}. Detailed modelling is required to show whether this is acceptable.

A18. "The properties of the medium should not be adversely affected by the presence of the waste."

A19. "The pore-water chemistry should be such as to minimise corrosion ..... and maximise predictability of the system."

These matters are outside the scope of this report.

7.2 Conclusions

At the end of this first phase of work on GME, the area appears to have many of the characteristics required for a disposal site, although few of these characteristics are the best that can be found in the world's oceans. The area is in a region of low volcanic and seismic activity, though quieter areas (especially with regard to volcanism) could be found. It is well away from major tectonic activity, but the sediments may be undergoing faulting at depth, possibly as a result of differential compaction. West of 24°W, and in the uppermost 20 m, there is a history of continuous deposition of medium-to-fine-grained sediments. However, east of 24°W the turbidite bases are coarser grained and may be erosive. The history of sedimentation below 20 m is not known. No evidence of high pore-water advection has yet been found, but the possibility of it occurring along faults or through open burrows in the sediments needs to be explored. Finally, although the reduced nature of the sediments may be advantageous in causing sorption of some anions, there is certainly evidence of enhanced mobility of other ions. Further work is therefore needed in several of these areas to ensure that the actual conditions are well understood and are in fact within acceptable limits.

7.3 Recommendations for further work

The most important outstanding geological objective at GME is to obtain a better understanding of the faults. We need to determine to what extent, and at what depth, the sediments are physically disrupted; whether this will lead to enhanced pore-water movement (either natural or waste-induced); how far from an individual fault or field of faults one needs to go before these effects become insignificant; the precise geographical distribution of the faults; and whether any of these factors are likely to change over the expected duration of a waste repository. This last requirement in particular means that the precise origin and nature of the faults must be understood. To answer these questions, we will need to carry out more detailed surveys of the distribution of the faults (including detailed surveys of areas at present thought to be fault-free), together with precise geophysical and geochemical investigations of individual faults to determine their nature and effects.

It is also necessary to extend our studies of the geological barrier off the abyssal plain and onto the abyssal hills. It is possible that hydrothermal circulation could be concentrated there (Embley et al., 1983), and this needs to be checked by heatflow and geochemical studies. There is some suggestion of erosion or at least non-deposition around the feet of abyssal hills (Weaver & Kuijpers, 1983; R. Schuttenhelm, personal communication, 1983), and this needs to be examined, as do the extent and effects of any sediment slumping off the hills.

We are still in need of good measurements of pore-water advection velocities through the undisturbed sediments of the abyssal plain; this will require in-situ measurements using PUPPI.

Another important uncertainty is the effect of the relatively high organic carbon content of the sediments on redox conditions and ion mobility; further geochemical work will be needed to resolve this.

Finally, we stress that none of our studies to date, except for seismic reflection profiling, have addressed the properties of sediments deeper than about 20 m. Deeper sampling is needed to check the stability of sediment deposition through the Pleistocene, to investigate earlier positions of the lower continental rise/abyssal plain boundary (and hence the likely extent of deep sand layers), to determine the physical properties of the deeper sediments, and to study important geochemical reactions that appear to be occurring below the current limit of sampling.

REFERENCES

ABBOT, D.H., MENKE, W. & MORIN, R., 1983. Constraints upon water advection in sediments of the Mariana Trough. Journal of Geophysical Research, 88, 1075-1093.

ABDEL-MONEM, A., FERNANDEZ, L.A. & BOONE, G.A., 1968. Pliocene-Pleistocene minimum K-Ar ages of the older eruptive centers, eastern Azores. EOS, Transactions of the American Geophysical Union, 49, p. 363 (Abstract).

ABDEL-MONEM, A.A., FERNANDEZ, L.A. & BOONE, G.A., 1975. K-Ar ages from the eastern Azores group (Santa Maria, Sao Miguel and the Formigas Islands). Lithos, No. 4, 247-254.

ANDERSON, D.R. (Ed.), 1980. Proceedings of the Fifth Annual NEA - Seabed Working Group Meeting, Bristol, England, March 3-5, 1980. Sandia National Laboratories, Albuquerque, Report No. SAND 80-0754, 252 pp.

ANDERSON, R.N., HOBART, M.A. & LANGSETH, M.G., 1979. Geothermal convection through oceanic crust and sediments in the Indian Ocean. Science, 204, 828-832.

BACKMAN, J. & SHACKLETON, N.J., 1983. Quantitative biochronology of Pliocene and early Pleistocene calcareous nannofossils from the Atlantic, Indian and Pacific Oceans. Marine Micropaleontology, 8, 141-170.

BANDA, E., DANOBEITIA, J.J., SURINACH, E. & ANSORGE, J., 1981. Features of crustal structure under Canary Islands. Earth and Planetary Science Letters, 55, 11-24.

BECKER, K. & VON HERZEN, R.P., 1983. Heat flow on the western flank of the East Pacific Rise at 21°N. Journal of Geophysical Research, 88, 1057-1066.

BECKER, K., VON HERZEN, R.P., FRANCIS, T.J.G., ANDERSON, R.N., HONNOREZ, J., ADAMSON, A.C., ALT, J.C., EMMERMANN, R., KEMPTON, P.D., KINOSHITA, H., LAVERNE, C., MOTTL, M.J. & NEWMARK R.L., 1982. In-situ electrical resistivity and bulk porosity of the oceanic crust, Costa Rica Rift. Nature, 300, 594-598.

BERGER, W.H. & VON RAD, U., 1972. Cretaceous and Cenozoic sediments from the Atlantic Ocean. Initial Reports of Deep Sea Drilling Project, 14, 787-954.

BOSSHARD, E. & MacFARLANE, D.J., 1970. Crustal structure of the western Canary Islands from seismic refraction and gravity data. Journal of Geophysical Research, 75, 4901-4918.

BOWEN, A.J., NORMARK, W.R. & PIPER, W.J., 1984. Modelling of turbidity currents on Navy submarine fan, California continental borderland. Sedimentology, 31, 169-185.

BREDEHOEFT, J.D. & PAPADOPULOS, I.S., 1965. Rates of vertical groundwater movement estimated from the Earth's thermal profile. Water Resources Research, 1, 325-328.

BURGESS, M. & JUDGE, A., 1981. Heatflow studies in the Sohm Abyssal Plain and their relevance to nuclear waste disposal investigations. Canada, Energy, Mines & Resources, Earth Physics Branch, Open File No. 81-15, 21 pp. & figs.

CASAGRANDE, A., 1936. The determination of the preconsolidation load and its practical significance. In: Proceedings 1st International Conference of Soil Mechanics and Foundation Engineers, Cambridge, Massachusetts, 1936, p. 60.

COLLETTE, B.J., SLOOTWEG, A.P., VERHOEF, J. & ROEST, W.R., 1984. Geophysical investigations of the floor of the Atlantic Ocean between 10°and 38°N (Kroonflag-Project). Proceedings, K. Nederlandse akademie van wetenschappen, C, 87, (1), 1-76.

CROWLEY, T.J., 1983. Calcium carbonate preservation patterns in the central North Atlantic during the last 150,000 years. Marine Geology, 51, 1-14.

CRONIN, T.M., 1983. Rapid sea level and climate change: evidence from continental and island margins. Quaternary Science Reviews, 1, 177-214.

CROWE, J. & McDUFF, R.E., 1979. Temperature and porewater chemistry profiles of sediments in the equatorial Pacific: incompatible results? EOS, Transactions of the American Geophysical Union, 60, p. 863 (Abstract).

DAMUTH, J.E., 1980. Use of high-frequency (3.5-12 kHz) echograms in the study of near-bottom sedimentation processes in the deep-sea: a review. Marine Geology, 38, 51-75.

DE VRIES, D.A., 1958. Simultaneous transfer of heat and moisture in porous media. EOS, Transactions of the American Geophysical Union, 39, 909-916.

DUIN, E.J.T. & KUIJPERS, A., 1983. Contribution to the Seabed Working Group Programmes. Progress report 1982. Geological studies on abyssal plains in the North Atlantic. Haarlem: Rijks Geologische Dienst. 107 pp. and 7 charts (unpublished manuscript).

DUIN, E.J.T., MESDAG, C.S. & KOK, P.T.J., 1984. Faulting in Madeira Abyssal Plain sediments. Marine Geology, 56, 299-308.

ELLIOT, A.J. & THORPE, S.A., 1983. Benthic observations on the Madeira Abyssal Plain. Oceanologica Acta, 6, 463-466.

EMBLEY, R.W., 1975. Studies of deep-sea sedimentation processes using high-frequency seismic data. Columbia University, Ph.D. thesis, 332 pp.

EMBLEY, R.W., 1976. New evidence for occurrence of debris flow deposits in the deep sea. Geology, 4, 371-374.

EMBLEY, R.W., 1980. The role of mass transport in the distribution and character of deep-ocean sediments with special reference to the North Atlantic. Marine Geology, 38, 23-50.

EMBLEY, R.W., 1982. Anatomy of some Atlantic Margin sediment slides and some comments on ages and mechanisms. In: Marine slides and other mass movements (ed. S. Saxov & J.K. Nieuwenhuis), pp. 189-213. New York: Plenum.

EMBLEY, R.W. & JACOBI, R.D., 1977. Exotic Middle Miocene sediment from Cape Verde Rise and its relation to piercement structures. American Association of Petroleum Geologists Bulletin, 61, 2004-2009.

EMBLEY, R.W., HOBART, M.A., ANDERSON, R.N. & ABOTT, D.A., 1983. Anomalous Heat Flow in the Northwest Atlantic: A Case for Continued Hydrothermal Circulation in 80 M.y. Crust. Journal of Geophysical Research, 88, 1067-1074.

EMILIANI, C, 1955. Pleistocene temperatures. Journal of Geology, 63, 538-578.

EWING, J. & EWING, M., 1959. Seismic-refraction measurements in the Atlantic Ocean basins, in the Mediterranean Sea, on the Mid-Atlantic Ridge, and in the Norwegian Sea. Bulletin of the Geological Society of America, 70, 291-318.

FLOOD, R.D., 1980. Deep-sea sedimentary morphology: modelling and interpretation of echo-sounding profiles. Marine Geology, 38, 77-92.

FREEMAN, T.J., MURRAY, C.N., FRANCIS, T.J.G., McPHAIL, S.D. & SCHULTHEISS, P.J., 1984. Modelling radioactive waste disposal by penetrator experiments in the abyssal Atlantic Ocean. Nature, 310, 130-133.

GARDNER, J.V., 1975. Late Pleistocene carbonate dissolution cycles in the eastern equatorial Atlantic. In: Dissolution of deep-sea carbonates (ed. W.V. Sliter, A.W.H. Be & W.H. Berger) pp. 129-141, Cushman Foundation for Foraminiferal Research, Special Publication 13.

GOULD, W.J., HENDRY, R.M. & HUPPERT, H.E., 1981. An abyssal topographic experiment. Deep-Sea Research, 28A, 409-440.

HAMBLIN, W.K., 1965. Origin of 'reverse drag' on the downthrown side of normal faults. Geological Society of America Bulletin, 76, 1145-1164.

HAMILTON, E.L., 1979. Sound velocity gradients in marine sediments. Journal of the Acoustical Society of America, 65, 909-922.

HAMILTON, E.L., 1980. Geoacoustic modeling of the sea floor. Journal of the

Acoustical Society of America, 68, 1313-1340.

HARLAND, W.B., COX, A.V., LLEWELLYN, P.G., PICKTON, C.A.G., SMITH, A.G. & WALTERS, R., 1982. A geologic timescale. Cambridge University Press, 131 pp.

HAYES, D.E., PIMM, A.C., et al., 1972. Initial Reports of Deep Sea Drilling Project, Vol. 14. Washington: Government Printing Office, 975 pp.

HOFFMAN, J., 1957. Hyperbolic curves applied to echo-sounding. International Hydrographic Review, 34(2), 45-55.

HONEA, J.W., 1956. Sam Fordyce - Vanderbilt fault system of southwest Texas. Transactions of the Gulf-Coast Association of Geological Societies, 6, p. 51.

HOUTZ, R.E. & EWING, J.T., 1963. Detailed sedimentary velocities from seismic refraction profiles in the western North Atlantic. Journal of Geophysical Research, 68, 5233-5258.

HUGGETT, Q.J., 1985. The distribution of ice-rafted material in the northeast Atlantic ocean - final results. IOS Report (in preparation).

IAGA Division I, Working Group 1, 1981. International Geomagnetic Reference Fields: DGRF 1965, DGRF 1970, DGRF 1975 and IGRF 1980. EOS, Transactions of the American Geophysical Union, 62, p. 1169.

JACOBI, R.D. & HAYES, D.E., 1982. Bathymetry, microphysiography and reflectivity characteristics of the West African Margin between Sierra Leone and Mauritania. In: Geology of the northwest African continental margin (ed. U. Von Rad, K. Hinz, M. Sarnthein & E. Seibold), pp. 182-212. Berlin: Springer-Verlag, 703 pp.

JESSOP, A.M., HOBART, M.A. & SCLATER, J.G., 1976. The world heat flow data collection, 1975. Canada, Energy, Mines & Resources, Earth Physics Branch, Geothermal Series No. 5, 125 pp.

KASTENS, K.A., 1984. Earthquakes as a triggering mechanism for debris flows and turbidites on the Calabrian Ridge. Marine Geology, 55, 13-33.

KENNEDY, W.J. & ODIN, G.S., 1982. The Jurassic and Cretaceous timescale in 1981. In: Numerical dating in stratigraphy, Part 1 (ed. G.S. Odin), pp. 557-592. Chichester: John Wiley, 630 pp.

KIDD, R.B. & SEARLE, R.C., 1984. Sedimentation in the southern Cape Verde Basin: regional observations by long-range sidescan sonar. In: Fine-grained sediments (ed. D.A.V. Stow & D.J.W. Piper), Geological Society of London, Special Publication, 145-151.

KIDD, R.B., SEARLE, R.C., WEAVER, P.P.E., JACOBS, C.L., HUGGETT, Q.J., NOEL, M.J. & SCHULTHEISS, P.J., 1983a. King's Trough Flank: geological and geophysical investigations of its suitability for high-level radioactive waste disposal. Institute of Oceanographic Sciences, Report No. 166, 103 pp.

KIDD, R.B., RUDDIMAN, W.F. et al., 1983b. Sediment Drifts and Intraplate Tectonics in the North Atlantic. Nature, 306, 532-533.

KIDD, R.B., SIMM, R.W. & SEARLE, R.C., 1985. Acoustic and sediment facies on the Saharan Continental Rise - a calibration of long-range sidescan sonar data. Marine and Petroleum Geology (in press).

KRAUSE, D.C., 1962. Interpretation of echo-sounding profiles. International Hydrographic Review, 39(1), 65-123.

KRAUSE, D.C. & WATKINS, N.D., 1970. North Atlantic crustal genesis in the vicinity of the Azores. Geophysical Journal of the Royal Astronomical Society, 19, 261-283.

KUIJPERS, A., 1982. Contribution to the Seabed Working Group Programme. Progress report 1981. The sedimentology of two northeast Atlantic study areas: the Western Madeira Abyssal Plain and the area west of Great Meteor Seamount. Haarlem: Rijks Geologische Dienst, 61pp. (Unpublished manuscript).

LANGSETH, M.G. & HERMAN, B.M., 1981. Heat transfer in the oceanic crust of the Brazil Basin. Journal of Geophysical Research, 86, 10805-10819.

LANGSETH, M.G., CANN, J.R., NATLAND, J.H. & HOBART, M., 1983. Geothermal phenomena at the Costa Rica Rift: background and objectives for drilling sites 501, 504 and 505. Initial Reports of Deep Sea Drilling Project, 69, 5-29.

LAUGHTON, A.S. & WHITMARSH, R.B., 1974. The Azores - Gibraltar plate boundary. In: Geodynamics of Iceland and the North Atlantic area (ed. L. Kristjansson), pp. 63-81. Dordrecht, Holland: Reidel.

LE PICHON, X., HOUTZ, R.E., DRAKE, C.L. & NAFE, J., 1965. Crustal structure of the mid-ocean ridges: 1. Seismic reflection measurements. Journal of Geophysical Research, 70, 319-339.

LILWALL, R.C., 1982. Intraplate seismicity and seismic risk in the Atlantic Ocean based on teleseismically observed earthquakes. Institute of Oceanographic Sciences, Report No. 136, 40 pp.

MANSURE, A.J. & REITER, M., 1979. A vertical groundwater movement correction for heat flow. Journal of Geophysical Research, 84, 3490-3496.

McKENZIE, D.P., 1972. Active tectonics of the Mediterranean region.

Geophysical Journal of the Royal Astronomical Society, 30, 109-185.

MORRIS, R.J., McCARTNEY, M.J., GROGAN, W.C. & SMITH, D.J., 1984. Post-depositional changes in the geochemistry of an organic-rich turbidite from sediments on the Madeira Abyssal Plain. (In preparation).

MULLER, T.J., 1981. Current and temperature measurements in the northeast Atlantic durings NEADS. Berichte aus dem Institut für Meereskunde, Christian-Albrechts-Universität, Kiel, No. 90, 98 pp.

NOEL, M.J., 1984a. Origins and significance of non-linear temperature profiles in deep-sea sediments. Geophysical Journal of the Royal Astronomical Society, 76, 673-690.

NOEL, M.J., 1984b. Measurements of sediment temperatures, conductivity and heat flow in the North Atlantic and their relevance to radioactive waste disposal. Institute of Oceanographic Sciences, Report No. 172, 27 pp. and figs.

PARSONS, B. & SCLATER, J.G., 1977. An analysis of the variation of ocean floor bathymetry and heatflow with age. Journal of Geophysical Research, 82, 803-827.

PEDDIE, N.W., 1982. International geomagnetic reference field 1980: a report by IAGA Division I, Working Group 1. Geophysical Journal of the Royal Astronomical Society, 68, 265-268.

PERRY, R.K., FLEMMING, H.S., VOGT, P.R., CHERKIS, N.Z., FEDEN, R.H., THIEDE, J., STRAND, J.E. & COLLETTE, B.J., 1981. North Atlantic Ocean: bathymetry and plate tectonic evolution. Geological Society of America, Map and Chart Series, MC-35.

PIPER, D.J.W., 1978. Turbidite muds and silts on deepsea fans and abyssal plains. In: Sedimentation in submarine canyons, fans and trenches (ed. D.J. Stanley & G. Kelling), pp. 163-176. Stroudsberg, Pa.: Hutchinson & Ross.

PRATT, R.M., 1961. Erratic boulders from the Great Meteor Seamount. Deep-Sea Research, 8, 152-153.

PRATT, R.M., 1963. Great Meteor Seamount. Deep-Sea Research, 10, 17-25.

PRELL, W.L., GARDNER, J.V. et al., 1982. Initial Reports of Deep Sea Drilling Project, Vol. 68. Washington: U.S. Government Printing Office.

RATCLIFFE, E.H., 1960. The thermal conductivities of ocean sediments. Journal of Geophysical Research, 65, 1535-1541.

RIDLEY, W.I., WATKINS, N.D. & MacFARLANE, D.J., 1974. The Oceanic Islands: Azores. In: Ocean basins and margins, Vol. 2, The North Atlantic (ed. A.E.M. Nairn & F.G. Stehli), pp. 445-483. New York: Plenum.

RUDDIMAN, W.F. McINTYRE, A., 1981. The North Atlantic Ocean during the last deglaciation. Palaeography, Palaeoclimatology, Palaeoecology, 35, 145-214.

SARNTHEIN, M., 1978. Neogene sand layers off N.W. Africa: composition and source environment. Initial Reports of Deep Sea Drilling Project, 41, Supplementary Volume, 939-959.

SAUNDERS, P.M., 1983a. Benthic boundary layer, IOS Observational Programme. Interim report January 1983. Institute of Oceanographic Sciences, Report No. 163, 33 pp.

SAUNDERS, P.M., 1983b. Benthic observations on the Madeira Abyssal Plain: currents and dispersion. Journal of Physical Oceanography, 13, 1416-1429.

SCHMINKE, H.U., 1979. Age and crustal structure of the Canary Islands. Journal of Geophysics, 46, 217-224.

SCHMINKE, H.U., 1982. Volcanic and chemical evolution of the Canary Islands. In: Geology of the northwest African continental margin (ed. U. Von Rad, K. Hinz, M. Sarnthein & E. Seibold), pp. 273-306. Berlin: Springer-Verlag, 703 pp.

SCHREIBER, E. & FOX, P.J., 1973. Compressional wave velocities of oceanic rocks and the geology of the oceanic crust: a brief summary. EOS, Transactions of the American Geophysical Union, 54, 1033-1035.

SCHULTHEISS, P.J. & GUNN, D.E., 1982. Geotechnical properties of deep sea sediments: a critical review of measurement techiques. Institute of Oceanographic Sciences, Report No. 134, 62 pp.

SCHULTHEISS, P.J., 1984. Consolidation and permeability of North Atlantic sediments. Institute of Oceanographic Sciences Report (in preparation).

SCHULTHEISS, P.J., McPHAIL, S.D., PACKWOOD, A.R. & HART, B., 1984. An instrument to measure differential pore pressures in deep-ocean sediments: Pop-Up-Pore-Pressure-Instrument (PUPPI). (In preparation).

SCLATER, J.G. & FRANCHETEAU, J., 1970. The implications of terrestrial heat-flow observations on current tectonic and geochemical models of the crust and upper mantle of the Earth. Geophysical Journal of the Royal Astronomical Society, 20, 509-542.

SEARLE, R.C., 1976. Lithospheric structure of the Azores Plateau from Rayleigh wave dispersion. Geophysical Journal of the Royal Astronomical Society, 44, 537-546.

SEARLE, R.C., 1979. Guidelines for the selection of sites for disposal of radioactive waste on or under the ocean floor. Institute of Oceanographic

Sciences, Report No. 91, 46 pp.

SEARLE, R.C., 1980. Tectonic pattern of the Azores spreading centre and triple junction. Earth and Planetary Science Letters, 51, 415-434.

SEARLE, R.C., 1984. Guidelines for the selection of sites that might prove suitable for disposal of high-level radioactive waste on or beneath the ocean floor. Nuclear Technology, 64, 166-174.

SEARLE, R.C., MONAHAN, D. & JOHNSON, G.L., 1982. General Bathymetric Chart of the Oceans, 5th ed., Sheet 5.08. Ottawa: Canadian Hydrographic Service. (Scale 1:10,000,000 at the Equator).

SEED, H.B. & IDRISS, I.M., 1971. A simplified procedure for evaluating soil liquefaction potential. Journal of the Soil Mechanics and Foundations Division, American Society of Civil Engineers, 97, 1249-1273.

SHACKLETON, N.J., 1969. The last interglacial in the marine anbd terrestrial records. Proceedings of the Royal Society of London, B, 174, 135-154.

SHACKLETON, N.J. & OPDYKE, N.D., 1973. Oxygen isotope and palaeomagnetic stratigraphy of equatorial Pacific core V28-238: oxygen isotope temperatures and ice volume on a 10^4 and 10^5 year scale. Quaternary Research, 3, 39-55.

SIMM, R.W. & KIDD, R.B., 1984. Submarine debris flow deposits detected by long-range sidescan sonar 1000 km from source. Geo-Marine Letters, 3, 13-16.

SMITH, S.G., 1977. A reflection profile modelling system. Geophysical Journal of the Royal Astronomical Society, 49, 723-737.

SOMERS, M.L., CARSON, R.M., REVIE, J.A., EDGE, R.H., BARROW, B.J. & ANDREWS, A.G., 1978. 'GLORIA II' - an improved long-range sidescan sonar. In: Oceanology International '78, Technical Session J., pp. 16-24. London: BPS Exhibitions Ltd., 610 pp.

STALLMAN, R.W., 1963. Computation of groundwater velocity from temperature data. U.S. Geological Survey, Water Supply Paper, 1544-H, 36-46.

THIERSTEIN, H.R., GEITZENAUER, K.R., MOLFINO, B. & SHACKLETON, N.J., 1977. Global synchroneity of late Quaternary coccolith datum levels: validation by oxygen isotopes. Geology, 5, 400-404.

THUNELL, R.C., 1982. Carbonate dissolution and abyssal hydrography in the Atlantic Ocean. Marine Geology, 47, 165-180.

TUCHOLKE, B.E. & MOUNTAIN, G.S., 1979. Seismic stratigraphy, lithostratigraphy and paleosedimentation patterns in the North American Basin. In: Deep Drilling Results in the Atlantic Ocean: Continental Margins and

Paleoenvironment (ed. M. Talwani & W.B.F. Ryan), pp. 56-86. Maurice Ewing Series, Vol. 2, Washington, D.C., American Geophysical Union.

TUCHOLKE, B.E. & VOGT, P.R., 1979. Western North Atlantic: sedimentary evolution and aspects of tectonic history. Initial Reports of Deep Sea Drilling Project, 43, 791-825.

TUCHOLKE, B.E. & LUDWIG, W.J., 1982. Structure and origin of the J Anomaly Ridge, western North Atlantic. Journal of Geophysical Research, 87, 9389-9407.

TUCHOLKE, B.E., FRY, V.A. & SHEPARD, L.E., 1983. Interim report on Nares Abyssal Plain studies for sub-seabed disposal of high-level nuclear waste. (Unpublished manuscript).

UDINTSEV, G.B., YELNIKOV, I.N., LUNARSKIY, G.N., KRASILSHCHIKOVA, G.N., GRINKO, B.N., PEREVOZCHIKOV, A.V. & BEREZYUK, V.M., 1976. Results of deep seismic soundings southwest of the Azores. Oceanology, 16, 360-362.

UDINTSEV, G.B., YELNIKOV, I.N. & LUNARSKIY, G.N., 1977. New data on the deep structure of the Earth's crust to the northwest of the Cape Verde Islands. Oceanology, 17, 163-166.

ULRICH, J., 1969. Topographie und Morphologie. In: Atlantische Kuppenfahrten 1967 mit dem Forschungschiff 'Meteor' - Reisebericht. 'Meteor' Forschungsergebnisse, A, No. 5, 1-71.

VAN ANDEL, T.H., 1975. Mesozoic-Cenozoic calcite compensation depth and the global distribution of calcareous sediments. Earth and Planetary Science Letters, 26, 187-194.

VERHOEF, J., 1983. The sedimentation pattern around the Atlantis-Meteor Seamount complex: a model study. 26 pp. & figs. (Unpublished manuscript).

VERHOEF, J. & COLLETTE, B.J., 1983. A tear fault system beneath the Atlantic-Meteor Seamount Group. Annales Geophysicae, 1, 199-206.

VERHOEF, J., 1984. Geophysical study of the Atlantis-Meteor Seamount complex. University of Utrecht, Ph.D. thesis.

VON RAD, U., 1974. Great Meteor and Josephine Seamounts (eastern North Atlantic): composition and origin of bioclastic sands, carbonate and pyroclastic rocks. 'Meteor' Forschungsergebnisse, Reihe C (19), pp. 1-61.

VON RAD, U. & WISSMANN, G., 1982. Cretaceous-Cenozoic history of the West Saharan continental margin (NW Africa): development, destruction and gravitational sedimentation. In: Geology of the northwest African continental margin (ed. U. Von Rad, K. Hinz, M. Sarnthein & E. Seibold), pp. 106-131. Berlin: Springer-Verlag, 703 pp.

WATKINS, N.D., 1973. Palaeomagnetism of the Canary Islands and Madeira. Geophysical Journal of the Royal Astronomical Society, 32, 249-267.

WATTS, A.B., COCHRAN, J.R. & SELZER, G., 1975. Gravity anomalies and flexure of the lithosphere: a three-dimensional study of the Great Meteor Seamount, northeast Atlantic. Journal of Geophysical Research, 80, 1391-1398.

WEAVER, P.P.E., 1983. An integrated stratigraphy of the Upper Quaternary of the King's Trough Flank area, NE Atlantic. Oceanologica Acta, 6, 451-456.

WEAVER, P.P.E. & KUIJPERS, A., 1983. Climatic control of turbidite deposition during the last 200,000 years on the Madeira Abyssal Plain. Nature, 306, 360-363.

WEAVER, P.P.E. & SCHULTHEISS, P.J., 1983. Vertical open burrows in deep-sea sediments 2 m in length. Nature, 301, 329-331.

WENDT, I., KREUZER, H., MÜLLER, P., VON RAD, U. & RASCHKA, H., 1976. K-Ar age of basalts from Great Meteor and Josephine seamounts (eastern north Atlantic). Deep-Sea Research, 23, 849-862.

WHITMARSH, R.B. & LILWALL, R.C., 1982. A new method for the determination of in-situ shear-wave velocity in deep-sea sediments. In: Oceanology International exhibition and conference, 2-5 March 1982, Brighton, Paper No. 4.2. Kingston-upon-Thames: Spearhead Exhibitions Ltd., 21 pp.

WILLIAMS, D.L., VON HERZEN, R.P., SCLATER, J.G. & ANDERSON, R.N., 1974. The Galapagos spreading centre: lithospheric cooling and hydrothermal circulation. Geophysical Journal of the Royal Astronomical Society, 38, 587-608.

WILLIAMS, D.L., GREEN, K., VAN ANDEL, T.H., VON HERZEN, R.P., DYMOND, J.R. & CRANE, K., 1979. The hydrothermal mounds of the Galapagos Rift: observations with DSRV Alvin and detailed heat flow studies. Journal of Geophysical Research, 84, 7467-7484.

WILSON, T.R.S., THOMSON, J., HYDES, D.J. & COLLEY, S., 1983. Status report on geochemical field results from Atlantic study sites. Institute of Oceanographic Sciences, Report No. 175, 57 pp.

WILSON, T.R.S., THOMSON, J., COLLEY, S., HYDES, D.J., HIGGS, N.C. & SORENSEN, J., 1984. Early organic diagenesis: the significance of progressive subsurface oxidation fronts in pelagic sediments. Geochimica et Cosmochimica Acta. (In press).

PLATE 1 Photograph of piston core D10688. For ease of handling, the core has been cut into seven sections. Note homogenous turbidite units and bioturbated pelagic units. In the interpretation, letters denote individual turbidites and numbers relate to oxygen isotope stages (odd numbers = glacial intervals).

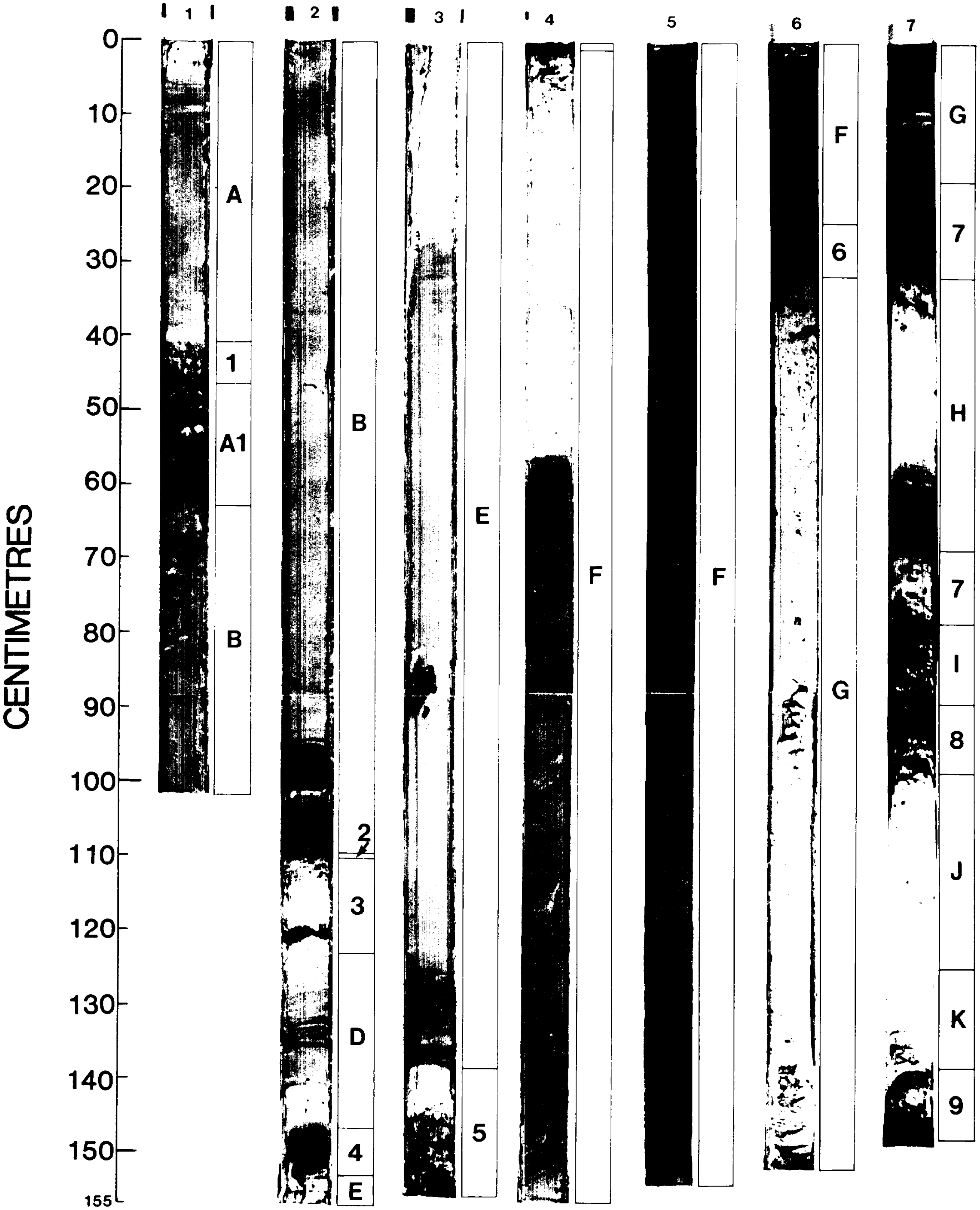
CENTIMETRES
0
10
20
30
40
50
60
70
80
90
100
110
120
130
140
150
155
1
A
1
A1
B
2
B
2
3
D
4
E
3
E
5
4
F
5
F
6
F
6
G
7
G
7
H
7
I
8
J
K
9